ABSTRACT

Title of Document: AN INTEGRATED ELECTROMAGNETIC
                                      MICRO-TURBO-GENERATOR SUPPORTED
                                      ON ENCAPSULATED MICROBALL
                                      BEARINGS

                                      Mustafa Ilker Beyaz, Doctor of Philosophy, 2011

Directed By: Professor Reza Ghodssi, Department of
                                      Electrical and Computer Engineering

This dissertation presents the development of an integrated electromagnetic micro-turbo-generator supported on encapsulated microball bearings for electromechanical power conversion in MEMS (Microelectromechanical Systems) scale. The device is composed of a silicon turbine rotor with magnetic materials that is supported by microballs over a stator with planar, multi-turn, three-phase copper coils. The micro-turbo-generator design exhibits a novel integration of three key technologies and components, namely encapsulated microball bearings, incorporated thick magnetic materials, and wafer-thick stator coils. Encapsulated microball bearings provide a robust supporting mechanism that enables a simple operation and actuation scheme with high mechanical stability. The integration of thick magnetic materials allows for a high magnetic flux density within the stator. The wafer-thick coil design optimizes the flux linkage and decreases the internal impedance of the stator for a higher output power. Geometrical design and device parameters are optimized based on theoretical

analysis and finite element simulations. A microfabrication process flow was designed using 15 optical masks and 110 process steps to fabricate the micro-turbo-generators, which demonstrates the complexity in device manufacturing. Two 10 pole devices with 2 and 3 turns per pole were fabricated. Single phase resistances of 46Ω and 220Ω were measured for the two stators, respectively. The device was actuated using pressurized nitrogen flowing through a silicon plumbing layer. A test setup was built to simultaneously measure the gas flow rate, pressure, rotor speed, and output voltage and power. Friction torques in the range of 5.5-33μNm were measured over a speed range of 0-16krpm (kilo rotations per minute) within the microball bearings using spin-down testing methodology. A maximum per-phase sinusoidal open circuit voltage of 0.1V was measured at 23krpm, and a maximum per-phase AC power of 10μW was delivered on a matched load at 10krpm, which are in full-agreement with the estimations based on theoretical analysis and simulations. The micro-turbo-generator presented in this work is capable of converting gas flow into electricity, and can potentially be coupled to a same-scale combustion engine to convert high-density hydrocarbon energy into electrical power to realize a high-density power source for portable electronic systems.

AN INTEGRATED ELECTROMAGNETIC MICRO-TURBO-GENERATOR
SUPPORTED ON ENCAPSULATED MICROBALL BEARINGS

By

Mustafa Ilker Beyaz

Dissertation submitted to the Faculty of the Graduate School of the
University of Maryland, College Park, in partial fulfillment
of the requirements for the degree of
Doctor of Philosophy
2011

Advisory Committee:
Professor Reza Ghodssi, Chair
Professor Isaak Mayergoyz
Professor Christopher Cadou
Professor Martin Peckerar
Professor Alireza Khaligh

Dedication

To my mother Muazzez Beyaz,

who has given me unconditional love and unending support throughout my life…

Acknowledgements

Table of Contents

List of Tables

List of Figures

ix

1. Introduction

1.1. Motivation

The continuous advancements in science and technology have revolutionized the development of electronic devices and resulted in miniaturized portable systems with applications ranging from implantable medical devices, home appliances, and military devices to microplatforms with multiple sensing capabilities. The portable power sources that they rely on, however, have not kept up with the pace of size reduction while providing enough power to most of these devices. Compact and high-density power units are still the missing piece to realize fully integrated, portable, and stand-alone microsystems.

Currently, most of the portable electronic systems are powered by batteries made from lithium ion or metal hydride material systems with energy densities on the order of 0.5MJ/kg [1]. Although this value is low compared to other materials in Figure 1, batteries are still viable power solutions for most of the electronic systems such as laptops, cell phones, and digital cameras as they can be recharged or replaced in the environments where these systems are used. In addition, their high efficiency on the order of 90% and lack of moving parts make them suitable for most portable devices [1]. However, batteries cannot be used in applications including micro air vehicles and portable military electronics, where low weight and volume along with high energy and power densities are required to maintain high-performance device operation for long times. Figure 1 shows the energy density of material types [2] excluding the radioactive materials and liquid hydrogen which are difficult to handle. This figure reveals that it is quite advantageous to utilize hydrocarbon fuels in

microscale power generation due to their high energy density, with values up to two orders of magnitude higher than current battery technology [3]. Accordingly, successful development of a microscale hydrocarbon-based energy source with efficiency as low as 2% would outperform current battery technology and extend the performance range of portable electronic systems. In addition, the power density in such an energy source is determined by the rate at which the hydrocarbons are burned, and can be increased depending on the requirements of specific applications. To realize a small scale power generation platform using hydrocarbon fuels, a serial connection of a fuel-powered combustion engine and an electromechanical generator is required.
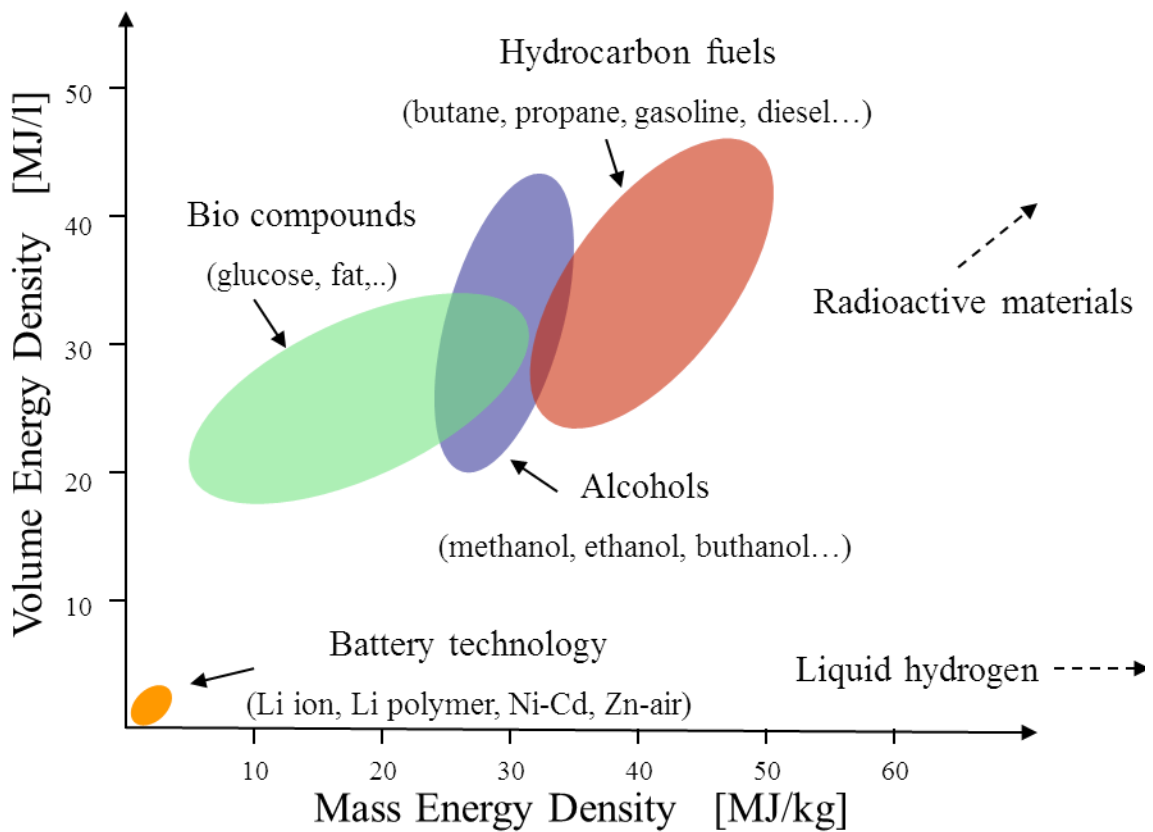
Figure 1.1. Energy density of materials showing high energy density of hydrocarbons [2].

Various combustion engines with centimeter–scale dimensions, such as COX Tee Dee ($0.16cm^3$), and COX Pee Wee ($0.33cm^3$) are commercially available [4]. In parallel, researchers at MIT have developed the building blocks of a microfabricated combustion engine with the smallest features on the order of micrometers [5-6]. To utilize the available energy from these miniature engines, equally compact electromechanical energy converters must be developed and coupled to these devices. Electromechanical generators based on electromagnetic energy conversion principles are widespread in macro-scale high-power generation systems. However, same kind of devices is not common for small-scale power supplies under 100W [7] mainly due to the restrictions of manufacturing technologies limiting the device designs to mostly planar rather than three-dimensional architectures observed in kW-scale systems. The manufacturing and integration of magnetic materials such as permanent magnets and high-permeability materials also pose challenges for small-scale generators. In addition, the development of bearing mechanisms that would enable high speed operation is required to compensate for small device size and to attain the targeted power levels. Finally, the high surface-to-volume ratio of small-scale devices leads to increasing mechanical losses resulting from friction and wear, specifically at the required high speeds.

The objective of this work is to develop a reliable, robust, and small-scale MEMS (Microelectromechanical Systems) micro-turbo-generator that can perform electromechanical energy conversion in small-scale. Given the ability to realize structures ranging from centimeters down to nanometers, MEMS technology is ideal for small scale power conversion. High rotational speeds achieved by MEMS

microturbines [5-8] also offer a great advantage over conventionally machined generators to attain high power densities. Finally, the batch fabrication techniques and low device cost make MEMS highly desirable for the development of small generators.

1.2. Summary of Contributions

The first electromagnetic micro-turbo-generator supported on encapsulated microball bearings has been developed for power conversion in small scale. Throughout the course of device development, new MEMS process techniques have been demonstrated. The following are the key contributions of this dissertation:

1. Development of an electromagnetic micro-turbo-generator supported on encapsulated microball bearings: The design, fabrication, and characterization of the first silicon micro-turbo-generator with integrated permanent magnets and encapsulated microballs are demonstrated. The device combines three key technologies and components for power generation, namely robust encapsulated microball bearings, integrated thick magnetic materials, and wafer-thick three-phase stator coils, enabling the realization of a stable, reliable, and high-power microgenerator. A maximum peak sinusoidal open circuit voltage of 0.1V was achieved at a rotor speed of 23krpm (kilo rotations per minute). Maximum per-phase AC power of 10µW was delivered on a matched load of 46Ω at 10krpm. Further integration of this micro-turbo-generator with a micro-scale combustion engine will enable the realization of high-density power sources capable of converting hydrocarbon energy into electricity for portable electrical systems. In addition, the

unique design and the dimensions of this device lend itself for the development of a power converter that can harvest human breathing, convert the mechanical energy in carbon dioxide flow into electricity, and recharge the batteries of portable electronic systems.

2. Wafer-thick three-dimensional stator coils: The micro-turbo-generator involves a unique stator design with coils as thick as one silicon wafer for optimum utilization of magnetic flux density from the magnets, as well as to decrease coil resistance. Due to geometric constraints, coils have a three-dimensional connection scheme to realize a three-phase structure.

3. A novel fabrication technique for through-hole electroplating of metals with planar surfaces: A new process technique for the fabrication of wafer-thick high-aspect-ratio copper structures has been developed. Through-hole electroplating process together with a seed layer detachment method are utilized to fabricate 500µm thick, 4mm long radial structures varying in width from 50µm to 250µm. The fabrication process flow is designed such that it enables the integration of sensitive device structures on one side of the through-plated wafer by excluding abrasive polishing techniques. Planar surfaces with protrusions less than 3µm were achieved on the polish-free side. This process leads to low-resistance electrical connections leading to decreased internal power dissipation and increased efficiency in Power MEMS devices such as ambient energy harvesters and generators.

1.3. Literature Review: MEMS-Scale Power Sources

As technology has improved over the past few decades and resulted in very small microchips with optical, mechanical, and electrical components, it became increasingly necessary to develop power sources with similar overall dimensions. The field of Power MEMS has emerged to address this need and to manufacture micro-scale power conversion platforms. Efforts in this field have been concentrated on regenerative and non-regenerative power supplies [9]. While "regenerative" refers to on-chip conversion of ambient energy in the form of light, vibration, temperature, and other types of radiation to electrical energy (power harvesting), "non-regenerative" simply refers to sources that need to be recharged after a certain period of time such as batteries, fuel cells, and combustors with coupled generators. This section briefly reviews these power generation architectures and focuses more on the work performed for the development of electromechanical microgenerators.

1.3.1. MEMS Power Harvesting

Generating electrical power from the energy available in the ambient poses an opportunity for replacing rechargeable power sources and developing self-sufficient microsystems. The most common ambient harvesters are solar cells utilizing the photovoltaic effect, which is the conversion of incident light to electrical energy. The use of high-energy sunlight and lack of any moving parts are among the advantages of these devices. However, the variability in sunlight puts additional constraints in power processing circuitry of solar cells. In addition, low efficiency is another drawback for these units [9]. Commercially available solar cells are usually

manufactured from silicon, and have efficiencies on the order of 10% [9]. Cells with other materials have higher efficiencies of up to 40% and power densities on the order of 30mW/cm^2, but are costly to manufacture [10-12]. Currently, III-V materials are being explored for the development of high-efficiency and low-cost solar cells for electrical systems [9].

Vibration is another source of energy present in the ambient. The focus in utilizing the ambient vibration has been to couple this mechanical energy to a singly or doubly clamped cantilever/diaphragm on a microchip. Various transduction mechanisms have been used for the conversion to electrical energy including electrostatic, electromagnetic, and piezoelectric [9]. As their power density is highly dependent on the vibration frequency, values on the order of 10mW/cm^3 have been achieved [13-17]. The availability of vibration in most environments is the thrust behind the research performed for improving vibration harvesters. However, the low frequency of ambient vibrations is a huge drawback for these devices. Accordingly, research in this field has been focused on hybrid harvesters bringing together different transduction mechanisms with tuning capabilities as well as on-chip charge storage units [9, 13-14].

Thermal gradients in the environment also present an opportunity for on-chip electrical power generation. The Seebeck effect is the physical phenomenon behind thermal-to-electrical power conversion, where the temperature difference in two junctions of different materials induces a voltage difference and hence an electric current. Examples of such devices are presented in [18-26] with power densities on the order of 0.2W/cm^3. Reliability and low noise are the advantages of these systems,

however the difficulties along with the cost in material processing are the key disadvantages of thermal scavengers.

1.3.2. Microbatteries, Micro Fuel Cells, and Micro Combustion

Due to many advantages including providing direct current with no conditioning circuitry, absence of moving parts, and reliability, microbatteries are good solutions for low power electronics [9, 27-32]. These power sources are developed using thin films of anode, cathode, and current collectors in various architectures and material systems. The high energy density of lithium ion microbatteries has caught much attention amongst other types of batteries and resulted in the concentration of most of the research efforts in this direction. Due to the nonlinear scaling of the battery size with respect to the transistor power consumption in portable electronic circuits, primary efforts have been focused on improving the power density of microbatteries. Materials such as $LiCoO_2$ and $LiMn_2O_4$ have been explored for high capacity [33] and three dimensional hierarchical architectures have been designed for improved total area and hence power density [34-37]. Specific challenges in realizing high power density lithium ion microbatteries also include the limitations on the intercalation of sufficiently high volumes of lithium, the irreversibility of the structural changes on thin films during this intercalation process, and material degradation during charge and discharge cycles. Consequently, much of the ongoing work has been focused on improving the material system used in microbatteries [9, 27-30].

Fuel cells convert chemical energy into electricity through electrochemical reactions involving fuel and oxidant at the anode and cathode, respectively. These reactions result in ions that move through the cell, and electric charges that flow through an external load, providing current and power [38]. There are different types of fuel cells such as proton exchange membrane fuel cells (PEMFC), direct methanol fuel cells (DMFC), reformed methanol fuel cells (RMFC), molten carbonate fuel cells (MCFC), solid oxide fuel cells (SOFC), and many others. Due to the high operation temperatures, additional required components, and materials issues associated with many of these types, significant portion of the research has been focused on micro scale PEMFC and DMFC. In both micro fuel cells, positively charged hydrogen ions are generated from H_2 (for PEMFC) and methanol (for DMFC) and passed through a proton exchange membrane [38] while electrons are passed through a circuit. The electrons and H^+ ions recombine at the cathode side through reactions with an oxidant, usually air, to produce water. H^+ production rate and H^+ diffusion through the membrane are amongst the factors determining the performance of micro fuel cells. Power densities up to $200mW/cm^2$ have been reported [9, 39-47]. Challenges associated with microfluidic system design and temperature and water management still remain for the development of reliable micro fuel cells to be integrated with portable electronic systems [9, 38].

High energy density of hydrocarbon fuels (such as propane and butane) on the order of 50MJ/kg is very attractive for high-density power generation for small scale systems. Therefore, converting the energy from micro combustion into electricity is quite advantageous to realize a compact power source package that can meet the

9

requirements of most micro scale systems [48]. Miniaturization of large scale combustion engines pose significant challenges including sustaining flames in micro-combustors in millimeter scale, achieving short reaction times, and heat loss [9, 48]. Extensive work has been conducted on miniature scale micro combustion including the MIT microengine project to realize a compact, reliable, and efficient micro combustion device [49-56], and numerous studies are still underway to address the challenges. Due to the potential high energy densities achievable with a hydrocarbon-based power generator, the study on micro combustion engines is still regarded as one of the promising frontiers of MEMS [48].

Thermophotovoltaic (TPV) devices provide a mechanism to convert the energy released by combustion into electricity through the photovoltaic effect. In such systems, the energetic photons emitted as a result of a combustion event create free electric charge in TPV cells that are able to move under electric field, thereby producing electrical power [9, 48]. Power densities on the order of $1W/cm^3$ have been demonstrated with such devices [57-62]. The direction in this field is geared towards the design and manufacturing of low band gap and high quality TPV cells to replace silicon solar cells and to improve the efficiency and power density [48].

Similar to large scale systems, electromechanical microgenerators, which are the topic of this dissertation, can also be used to generate electricity at high power densities from hydrocarbons through the use of a micro combustion engine [7]. In such systems, chemical energy is first converted to rotational energy in the combustion engine, and then to electricity by the rotary electromagnetic generator. The physical phenomenon behind this conversion is the Faraday's law of

electromagnetic induction, where moving magnetic fields on top of stationary coils induce a voltage difference between coil ends. The next section reviews MEMS rotary electromagnetic microgenerators in detail.

1.3.3. Electromagnetic Rotary Microgenerators

Several studies have been conducted to investigate the effect of downscaling on electromechanical energy conversion devices [63-66]. It has been demonstrated that inductance or switched reluctance machines are not feasible for miniaturization due to the unfavorable scaling of electrical currents required to establish necessary magnetic fields. Therefore, small scale devices mostly use permanent magnets (PMs) as the magnetic flux density of a PM does not depend on its size [7]. In such machines, the magnetic fields sourced by PMs interact with coil windings typically made of copper (Cu). A relative velocity created between the PMs and the windings by a prime mover results in a time varying magnetic flux that induces voltages on the coils. When connected to a load, the coils deliver electrical power. Rotational magnetic microgenerators have the same operating principles as that of their macroscale counterparts. They are designed for continuous rotational motion under a steady driving torque available from a fluid powered turbine or a heat engine [7].

The first micro power generation system was developed by Wiegele in 1996 [67]. He designed a gas flow powered planar microturbine system to be operated as a switched reluctance generator. The 3.5mm diameter device was fabricated and rotated at 4.5krpm. However, no output power was reported as this module was never implemented.

11

An axial flow microturbine-based axial flux PM microgenerator has been reported by Holmes *et al.* at Imperial College [68-69]. Microfabrication techniques together with laser etching have been used to fabricate the 7.5mm diameter device with a total volume of $0.5cm^3$. The generator was designed to have an SU-8 polymer rotor supported by off-the-shelf ball-race bearings over a silicon stator with Cu windings. A picture of the rotor of the device is shown in Figure. 1.2.
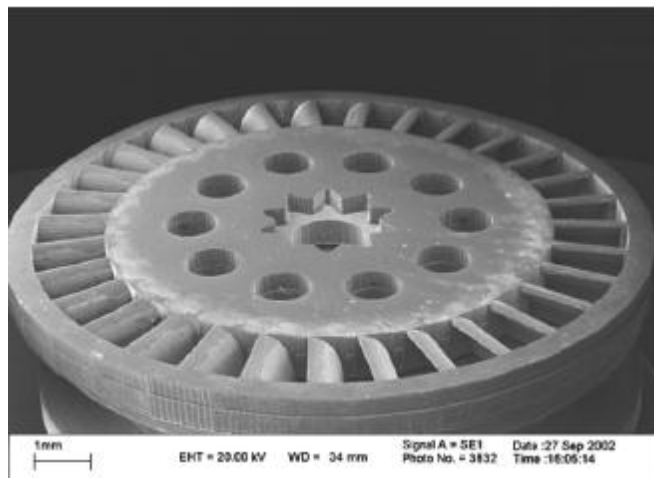
Figure 1.2. An SEM image of the rotor in [69].

Axial air flow results in rotation due to the laser etched rotor blades as shown in Figure 1.2. The device uses 10 pieces of NdFeB PMs inserted into the bottom side of the rotor as the source of the magnetic field. After the stator fabrication, the coil resistance and stator-to-rotor air gap were measured to be 45Ω and 120μm, respectively. A prototype of the device was operated, without the ball-race bearings, by a DC motor and the device delivered a maximum power of 1.1mW at 30krpm. They observed that the implementation of soft magnetic materials increases the output voltage by 33%. To increase the output power, the authors also designed a

two-stator approach located on the top and bottom of the rotor. However, this design was never tested.

Pan and Wu reported a similar axial flux eight pole PM generator [70-72] that measures 5mm in diameter. An alternative coil fabrication was developed to create a four layer Cu winding on the stator (Figure. 1.3) while NdFeB magnets were used for the rotor.

Figure 1.3. Stator with filament windings in [70]. Only one layer is shown.

The fabrication resulted in a total coil resistance of 30Ω. When the rotor was spun using a spindle, the generator delivered a maximum power of 0.412mW at 2.2krpm at an air gap of 1mm. The authors later reported the fabrication of stator coils using low temperature co-fired ceramic materials. With this technique and some modifications in the test setup, output power levels as high as 1.89mW at 13,325 rpm have been measured [72].

Researchers at Laboratoire d'Electrotechnique de Grenoble (LEG) developed a three phase planar micro-turbo-generator [66, 73-74]. Coil housings were first etched in silicon and electroplated with Cu up to a thickness of 20µm that resulted in a total coil resistance of 2-5Ω per phase. The rotor was an 8mm diameter 30 pole SmCo or NdFeB magnet which was patterned using electro discharge machining (EDM) technique to have turbine blade structures. The device used magneto-pneumatic bearings where the compressed air creates the rotation while a SmCo ring provides the normal force that keeps the rotor in place (Figure. 1.4). Depending on the rotor speed, the air gap was measured to be between 10µm and 50µm.
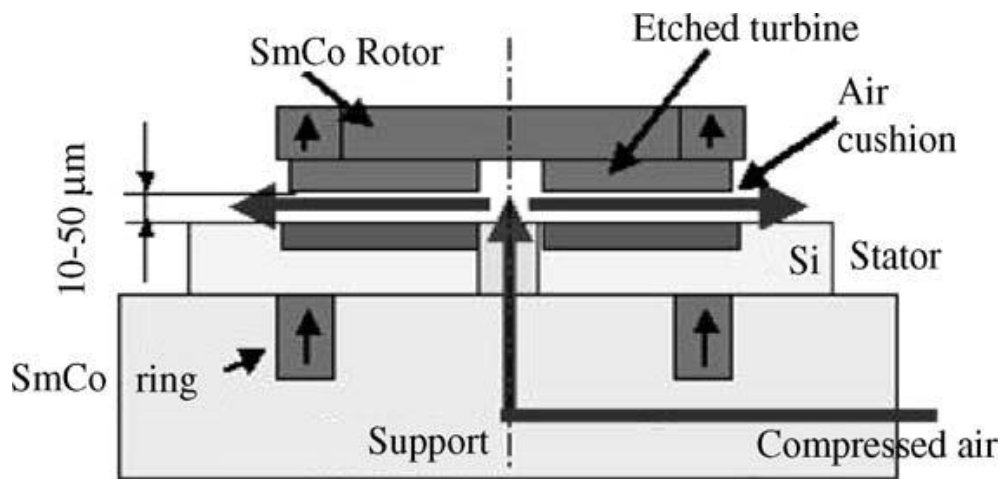
Figure 1.4. Schematic illustration of the microgenerator on magneto-pneumatic bearings in [74].

The device was operated up to 58krpm with compressed air, and delivered a maximum power of 14.6 mW. By using a rectifier circuit with Schottky diodes, they were able to generate 5mW DC power with an electrical efficiency of 33%. To spin the device at higher speeds, the authors used a dental drill and achieved rotational

speeds up to 400krpm. Using wye-connected 12Ω resistors, the device delivered 5W

power at a stator-to-rotor air gap of 50μm.

It can be concluded from the aforementioned devices that high coil resistance

is one of the obstacles in reaching higher output power levels. A joint research group

from Georgia Institute of Technology (GATECH) and Massachusetts Institute of

Technology (MIT) focused on overcoming this factor by thick coil fabrication. Das *et

al.* first reported a comprehensive study of the electromechanical energy conversion

principles together with power loss mechanisms such as winding loss, eddy currents,

and hysteresis that play important role in device efficiency [75-76]. A three phase

axial flux PM generator with low resistance windings was then designed and

fabricated for high speed operation [77-81]. By electroplating the Cu coil windings up

to 120μm, they decreased per phase coil resistances down to 0.1Ω for an 8 pole 2

turns per pole stator. The coils were fabricated on a permalloy substrate rather than

silicon to increase the magnetic flux density from the PMs. The 9.5mm diameter rotor

is composed of SmCo magnets with hiperco50 attached on the back side to prevent

magnetic saturation. The schematics of the rotor and stator are shown in Figures 1.5

and 1.6, respectively.
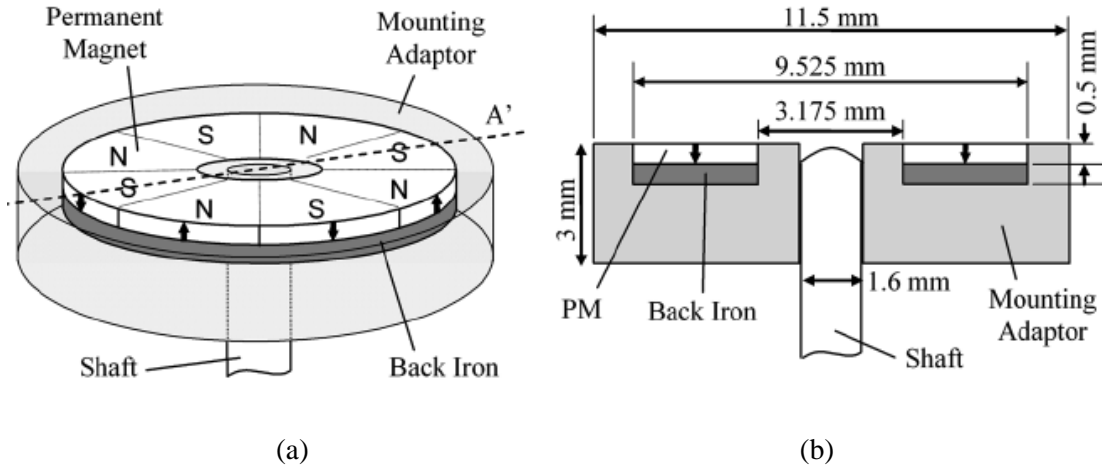
Figure 1.5 (a) The schematic (a) angled and (b) side views of the rotor in [77].
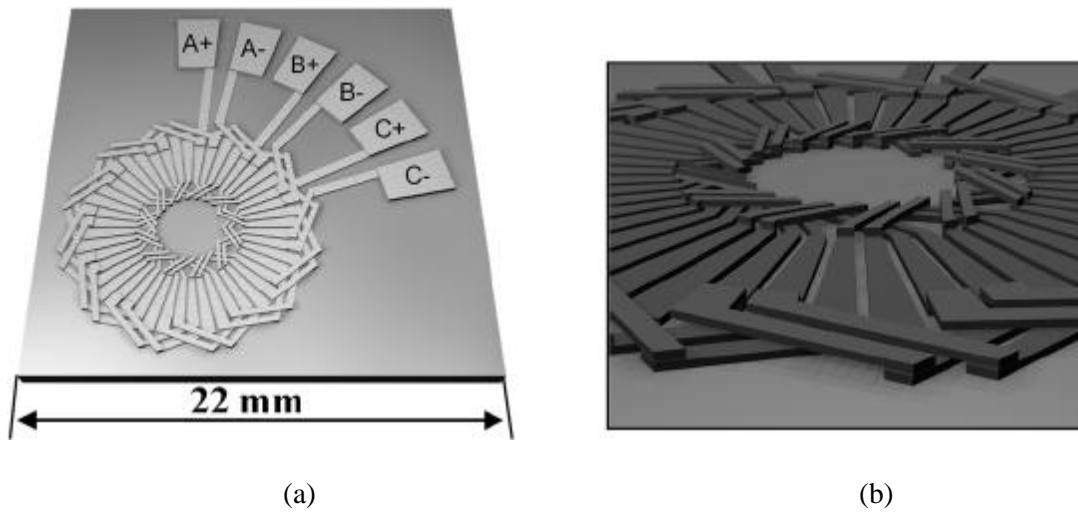
Figure 1.6. The (a) top, and (b) side views of the stator winding pattern in [77-81].

Due to the lack of an integrated rotor bearing, the rotor was run using a spindle. Before the operation, a micropositioner was used to set the air gap to 100μm that was the smallest reliable distance possible with the test setup. With this setup, the rotor was rotated up to 120krpm while the stator coils were connected to a three phase diode bridge rectifier through a delta-wye transformer. The output power was

measured under different electrical loads and it was observed that the device delivered a maximum DC output power of 1.1W to a 25Ω matched load. At higher speeds, the magnets broke into pieces due to the high centrifugal forces. High speed mechanical characterization of the device was also reported in [82].

The same group designed and fabricated a second-generation device with more efficient coil design and a more robust rotor with a titanium housing to support the magnets at higher speeds [83]. The 8 pole 3 turns per pole device had a per phase coil resistance of 0.16Ω and was spun at speeds up to 305krpm. An AC and DC output powers of 12W and 8W, respectively, were measured across a matched load of 37Ω with an overall generator efficiency of 28%. The device was also characterized at high temperatures [84-85] and an output power of 4W at 200°C was reported.

In parallel, the researchers at MIT developed an air bearing-supported turbine rotor and demonstrated rotational speeds over 1 million rpm [86]. Through some modifications in the device in [83], the rotor of [86] and the stator of [83] were integrated using a drop-in winding method (Figure 1.7). In operation, the NdFeB magnets integrated into the rotor introduced a huge mass loading to the system. Therefore, the highest achievable speed was limited to 40krpm above which the rotor could not be stably rotated. At this speed, a maximum power of 19mW was delivered to a matched resistive load [86-87].
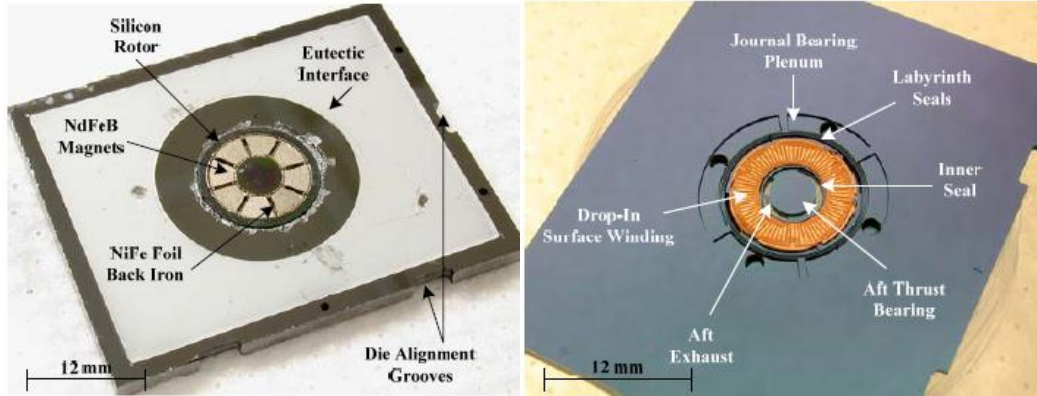
Figure 1.7. The rotor (left) and stator (right) of air bearing micro-turbo-generator [86-87].

Finally, Herrault *et al.* further miniaturized the device in [88-91] and fabricated an axial flux PM generator with a diameter of 2mm. The rotor was located 50µm above the stator and was spun at 392krpm using a spindle. Under these conditions, the 4 pole 6 turns per pole stator with 1.53Ω per phase resistance delivered a maximum output power of 6.6mW. They later designed a microfluidic package with off-the-shelf ball bearings for a compact system and demonstrated a rotational speed of 203krpm and an output power of 0.8mW [92]. The same authors have improved the design presented in [83] by adding laminated permalloy structure on the stator. Using an externally driven spindle, they reached rotor speeds up to 200krpm and demonstrated a maximum AC power of 1.05W which is 225% improvement compared to the device without laminated stator core [93].

Although very rare, approaches such as manufacturing a small gas turbine and attaching an off-the-shelf motor in generation mode exist, but are out of the scope of this review [94]. In addition, a gas turbine with a generator component has been conventionally machined with dimensions on the order of several centimeters, and

spun up to 700krpm [95]. The device was not tested for power delivery, but the expected power at this speed was reported to be 55W.

Table 1.1 and 1.2 summarize the important features and performance parameters of the microgenerators discussed above, respectively.

	Radius (mm)	Volume (cm^3)	Magnets	Bearings	Number of poles	Turns per pole
Holmes *et al.* [69]	3.7	0.041	NdFeB	None	10	NA
Pan *et al.* [72]	2.5	0.081	NdFeB	None	8	NA
Raisigel *et al.* [74]	4	0.023	SmCo - NdFeB	Magneto-pneumatic	30	Not given
Arnold *et al.* [83]	4.75	0.136	SmCo – NdFeB	None	8	3
Yen *et al.* [87]	4.75	0.041	NdFeB	Air	8	3
Herrault *et al.* [88]	1	0.0034	NdFeB	None	4	6
Herrault [93]	4.75	0.15	NdFeB	None	8	3

Table 1.1. Parameters of previously reported microgenerators.

	Resistance	Max. speed	Output voltage	Output power (AC)	Power density (W/cm^3)	Normalized power density (W/cm^3.rpm^2)
Holmes *et al.* **[69]**	45Ω	70krpm	2.5V	1.1mW at 30krpm	0.027	2.9×10^{-11}
Pan *et al.* **[72]**	13Ω	13,325rpm	0.2V	1.89mW	0.023	1.3×10^{-10}
Raisigel *et al.* **[74]**	2-5Ω	400krpm	10V	5W at 400krpm	220	1.37×10^{-9}
Arnold *et al.* **[83]**	0.2Ω	305krpm	2V	12W	88	0.94×10^{-9}
Yen *et al.* **[87]**	0.33Ω	40krpm	0.2V	19mW	0.46	2.9×10^{-10}
Herrault *et al.* **[88]**	1.53Ω	392krpm	0.12	6.6mW	1.95	1.27×10^{-11}
Herrault [93]	0.32Ω	200krpm	0.7	1.05W	9.5	2.37×10^{-10}

Table 1.2. Performance of previously reported microgenerators.

A major aspect for the development of a fully integrated microgenerator is the incorporation of a stable bearing mechanism that can enable simple and reliable device operation at high speeds without external components. Due to their robust nature and simple fabrication, microball bearings have been rigorously studied at the MEMS Sensors and Actuators Laboratory at the University of Maryland, College Park, and have been shown to provide a stable and low-friction support structure to dynamic MEMS devices [96-128]. Modafe *et al.* and Ghalichechian *et al.* demonstrated the first linear micromotors supported on microball bearings. The devices used a variable capacitance actuation mechanism and reached speeds on the order of 7mm/s [100-106]. The implementation of a closed-loop control system improved the actuation-motion synchronization and enabled speeds up to 20mm/s [107-112]. A rotary version of this device was later demonstrated by Ghalichechian with a rotational speed and net produced torque of 517rpm and 5.62µNm, respectively, with friction coefficient values on the order of 0.02 [113-117]. In parallel, Waits *et al.* developed encapsulated microball bearing technology and utilized it to fabricate a micropump with a microturbine structure for fluid delivery in small scale [8, 118-121]. Rotational speeds up to 87krpm have been achieved with pneumatic actuation. A detailed friction and wear characterization of encapsulated microball bearings was performed by McCarthy *et al.* [122-123]. Dependency of friction on rotational speed and normal force was thoroughly investigated and reported. In addition, a study by Hanrahan *et al.* investigated the effect of hard film coatings on friction and wear [124-125]. Finally, a rotary microactuator with electro-pneumatic thrust balance was presented by McCarthy *et al.* in [126-128]. The

21

reduction in normal load due to pneumatic thrust balance enabled the device to reach 2000rpm with reliable operation. These works have demonstrated the robustness, stability, simple-to-operate, high-speed, low friction, and low wear properties of microball bearings, which are very important advantages in a support mechanism to realize a robust, reliable, and high-speed microgenerator with a high-density power generation capability.

1.4. Thesis Objective and Structure

The purpose of this research is to develop the first integrated MEMS micro-turbo-generator with a simple actuation mechanism and a robust support structure for hydrocarbon-based microscale power source development. Specifically, this work targets the power-limiting factors evident from the reported devices to improve output electrical power. Accordingly, the micro-turbo-generator presented in this dissertation combines three key advantages and technologies, namely encapsulated microball bearings, incorporation of thick and high flux magnetic materials, and wafer-thick three-dimensional stator coils. The use of encapsulated microball bearings enables reliable and stable device operation at high rotational speeds [96-128] and eliminates the need for extra pneumatic or magnetic support to the rotor. Robustness and stability of microballs also allow for integration of thick, heavy, and high-flux magnetic materials that provide the necessary magnetic flux facilitating electromechanical energy conversion within the device. The unique design of the stator and wafer-thick coil structures optimize the flux linkage from the rotor to the stator while decreasing the coil resistance. This micro-turbo-generator also provides a

design platform for further improvement to achieve milliwatt to watt-level power generation in a compact frame for small-scale electrical systems. The schematic of the device showing these integral components is presented in Figure 1.8.

ROTOR

Microball Bearings

Magnetic Materials

Backside Connections

Wafer-Thick Coils
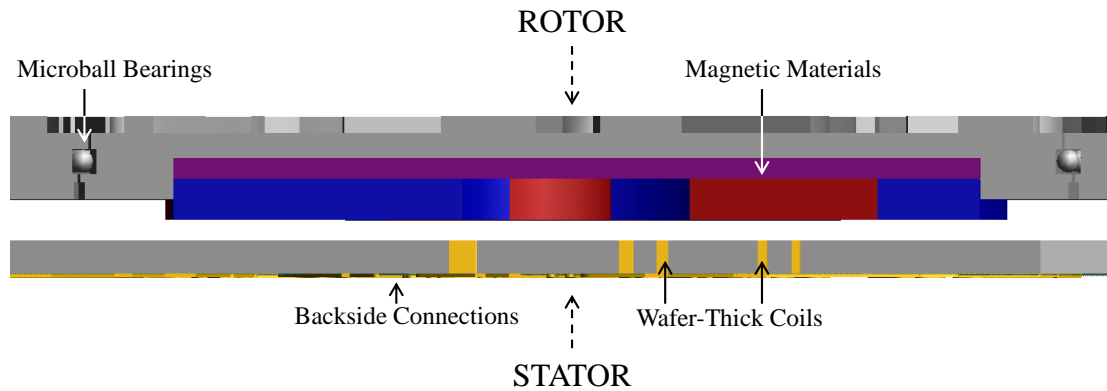
STATOR

Figure 1.8 Schematic of the micro-turbo-generator showing the rotor, stator, microball bearings, integrated magnetic materials, and coil structure with backside coil connections.

Chapter 1 presented the motivation for the development of compact MEMS microgenerators. MEMS-scale power generation architectures were introduced and key research in MEMS microgenerators was reviewed. In addition, contributions of this work to the field along with the objectives were presented.

Chapter 2 focuses on the theory, device analysis, simulation, modeling, and design of the micro-turbo-generator. Fundamental equations governing the device operation are explained and a mathematical analysis is presented. Simulations on physical phenomena such as magnetic leakage and saturation are provided for more accurate device performance estimations. Based on this analysis and considering microfabrication limitations, different device designs are presented.

Chapter 3 describes the microfabrication of the micro-turbo-generator. Rotor and stator fabrication along with magnetic material integration are thoroughly discussed. Process development leading to a novel microfabrication technique for wafer-thick copper coils is also presented.

Chapter 4 focuses on the testing procedure and device characterization. The test setup along with the performance testing procedure is thoroughly explained. Experimental results regarding the mechanical and electrical performance of the device are reported. The results are thoroughly discussed and compared with the theoretical analysis and estimations.

Chapter 5 concludes this dissertation with a summary of key achievements and contributions to the field. Future work for potential improvements on device performance and other opportunities to utilize this technology are discussed.

2. Analysis and Design

This chapter begins with a general description of theory of operation and governing physics. These concepts are applied to a MEMS frame to design the general device structure. Certain electrical and mechanical performance parameters such as open circuit voltage, magnetic flux linkage, resistance, inductance, torque, and normal force along with power losses are analyzed and simulated. Device geometry and parameters are optimized and different designs are presented. Performance estimations are also calculated based on this analysis.

2.1. Principle of Operation

The microgenerator described in this dissertation is of synchronous type and composed of a stator that employs windings and a rotor with permanent magnets. Unlike most macro-scale generators, winding design is chosen to have a planar structure mainly due to the limitations in microfabrication technology and the planar nature of MEMS. Due to the same reasons, permanent magnets have a flux density in the axial direction rather than radial. The windings on the stator are three phase copper coils separated with 120° spatial phase angle while permanent magnets on the rotor are distributed radially on a circular pattern with alternating polarity. Figure 2.1 shows a basic configuration of three-phase coils and permanent magnets. This configuration is not the final design and presented here for a visual illustration.
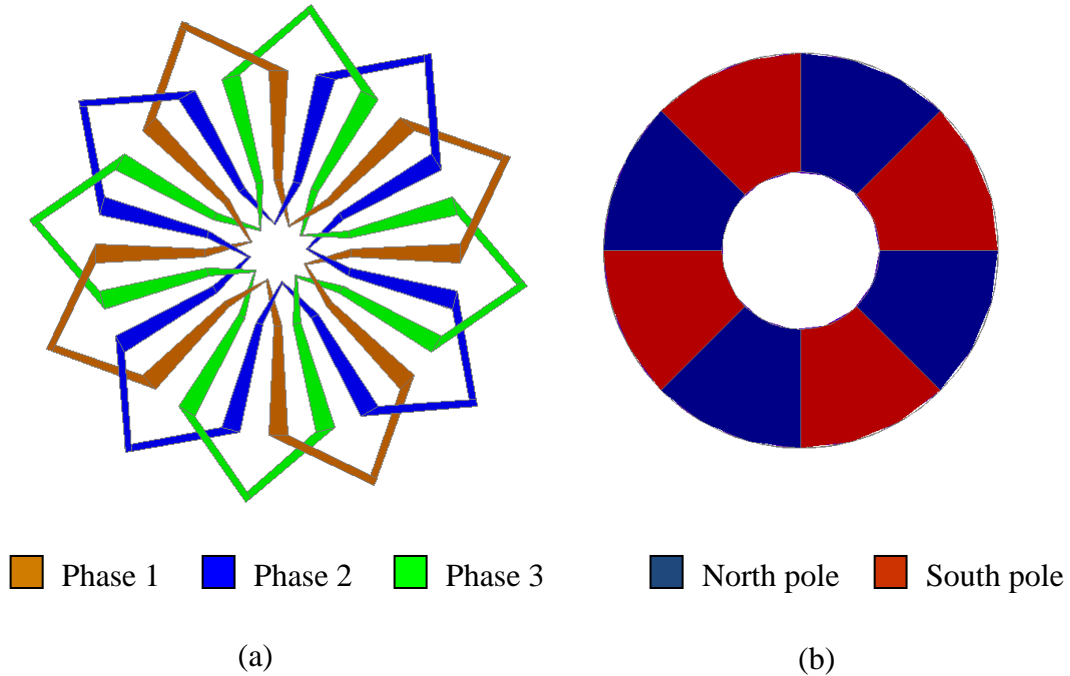
Figure 2.1. Structures of (a) three-phase coils and (b) rotor magnets with eight poles.

The rotation of the discrete magnetic poles creates a time varying magnetic field passing through any given coil loop. This alternating field induces a voltage V on the coil according to Faraday's law of electromagnetic induction given by the following equation [129-131];

$$V = -\frac{d\Phi}{dt} \tag{2-1}$$

In this equation, Φ is the total magnetic flux linked from the magnets to the coil area that is described by the surface integral;

$$\Phi = \int B.dS \tag{2-2}$$

where B represents the effective magnetic flux density on the coils. The same phenomenon can also be described by the flux-cutting electromotive force [131];

$$V = \int (\upsilon \times B) \bullet dl \qquad (2\text{-}3)$$

where υ is the velocity of the magnetic field relative to the coil and l is the length. The integration in eq. 2-3 is nonzero only for the radial portions of the coils, leading to the same result obtained by using eq. 2-1. When an electrical load Z_L is connected to the coils with an intrinsic impedance Z_{coil} and an induced voltage V, the current I flowing through the coils can be described as,

$$I = \frac{V}{Z_L + Z_{coil}} \qquad (2\text{-}4)$$

Therefore, electrical work P_{el} is done in the system with the following formula;

$$P_{el} = \frac{V^2}{Z_L + Z_{coil}} \qquad (2\text{-}5)$$

with the maximum power transfer on the load occurring at $Z_L = Z_{coil}$ as described by Thevenin's power transfer theory. This work is sourced by the mechanical torque T provided by the prime mover, i.e. either a shaft or an air driven turbine spinning at a rotational speed of ω. In a lossless system, the generated electrical power P_{el} is equal to the input mechanical power P_{mech} where,

$$P_{el} = P_{mech} = T \times \omega \qquad (2\text{-}6)$$

Through these physical phenomena, commonly referred to as electromechanical energy conversion principles [129], the mechanical energy is converted into electrical energy. Same principles apply for MEMS devices as well as macro scale electromagnetic generators that are used in large power systems.

2.2. Design

Stator: The stator is comprised of three phase planar Cu coils embedded in a silicon substrate. The choice of low resistivity Cu decreases the coil resistance and thus minimizes the power loss in the coils. Silicon is selected as the substrate and the structural material due to the well-developed micromachining technology which allows for the fabrication of high aspect ratio coil housings. The design also includes a permendur (FeCoV) ring as a back iron with high magnetic permeability to decrease the magnetic reluctance of the device for a higher magnetic flux density. As stator design and optimization is based on the integration of this component, it is not included in this work to decrease the complexity and minimize the normal load on ball bearings that will be explained later in this dissertation.

The three phase planar coils mandate the design of a three dimensional coil structure where the first layer of coils are integrated in a silicon substrate and the second layer that includes connections is patterned on an isolation layer. Figure 2.2 shows one of the three phases with 8 poles 1 turn per pole and 8 poles 2 turns per pole to demonstrate the coil structure as well as the planar turns per pole concepts. Due to the microfabrication constraints limiting the device structure to a planar design, each turn is slightly shifted in space compared to the original turn. A three phase construction of this design is shown in Figure 2.3. Note that these figures are to help the reader visualize the coil structure and that this is not the final design.

(a)   (b)
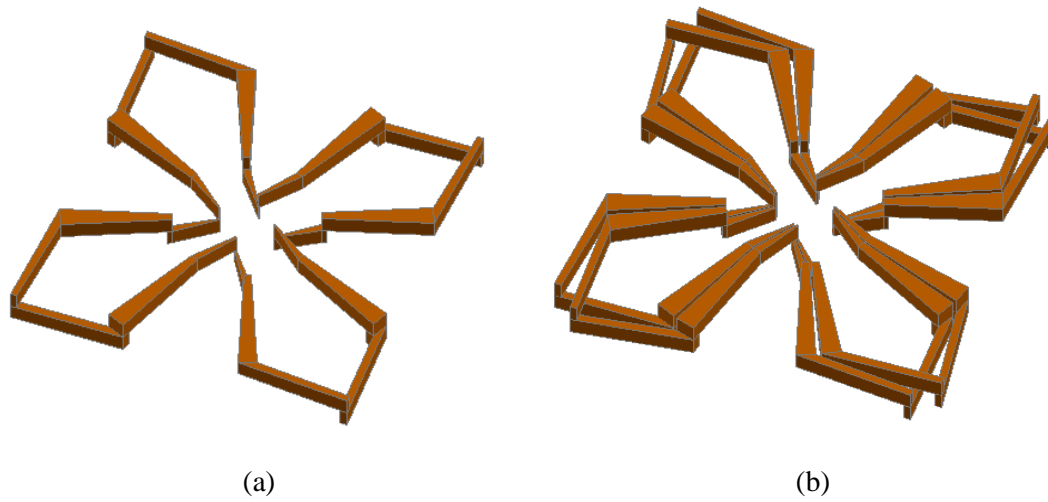
Figure 2.2. One phase 8 pole coils with (a) 1 turn per pole, (b) 2 turns per pole
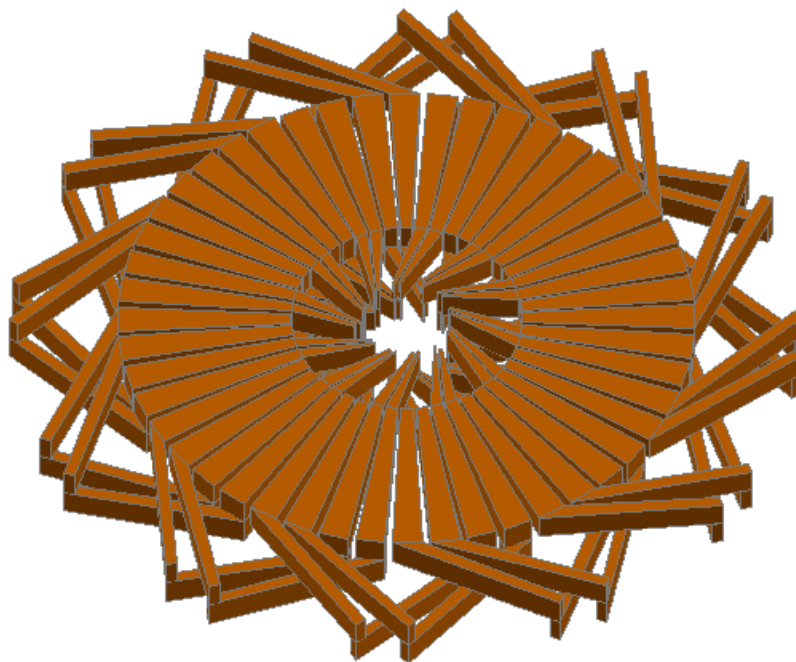
Figure 2.3. Three phase 8 pole 2 turns per pole coils

The integration of these coils in the stator structure as well as future incorporation of the permendur back iron is shown in Figure 2.4. Six electrical pads to extract signals from three different phases are also demonstrated.

Copper coils integrated in silicon

Silicon substrate

(a)

Electrical pads

Backside coil connections

Back iron (permendur)

Isolation layer

Silicon substrate
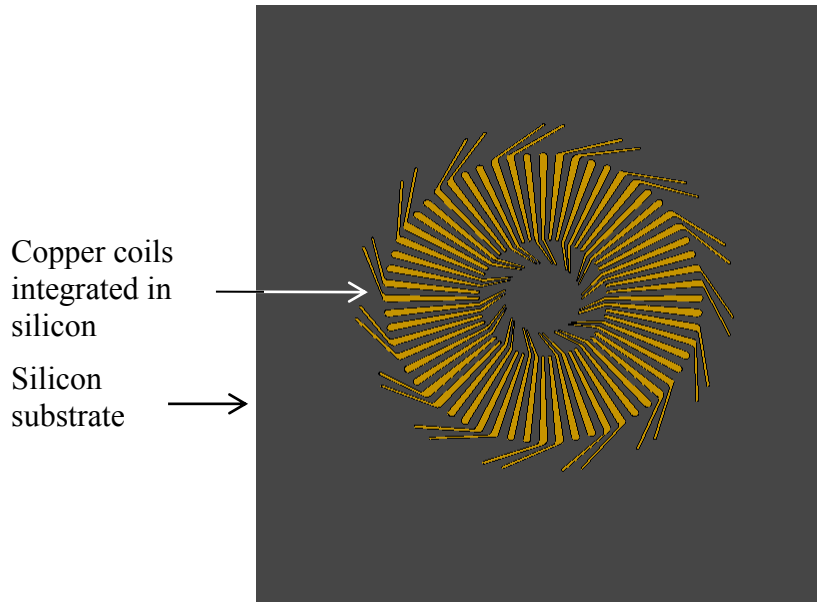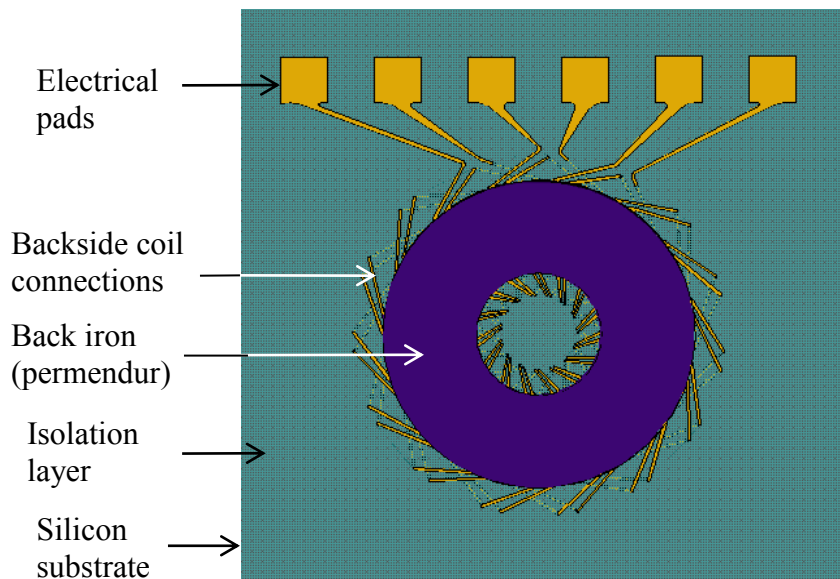
(b)

Figure 2.4. Complete stator design (a) top view, (b) bottom view. The back iron shown in (b) is not integrated in this work to decrease the complexity of the device.

Rotor: The rotor is comprised of two silicon wafers bonded together encapsulating microballs for mechanical stability, low friction and wear. The center rotor is released from the peripheral silicon frame and is free to rotate. NdFeB permanent magnet pieces having a remanence magnetic flux density of B_r=1.4T and another permendur disc are embedded in the bottom wafer (Figure 2.5) to maximize flux linkage to the stator. Turbine structures are etched on the top wafer to drive the rotor using pressurized gas. To accommodate the space for 200μm high turbine blades, magnets, and permendur in the two 500μm thick silicon wafer stack, the thicknesses of magnets and permendur disc are set to be 500μm and 250μm, respectively. Figure 2.5 shows a rotor with the microballs, magnetic materials, and turbine blades for illustration. Another wafer piece, which is referred to as plumbing wafer, is also placed on top of the rotor to inlet the pressurized gas from the rotor sides and direct the gas flow through the turbine blades. This component is not shown in Figure 2.5 and will be described in Chapters 3 and 4.

Bearings: The rotor utilizes stainless steel microball bearings (Ø=285μm) encapsulated in between the two rotor wafers (Figure 2.5b) with 290μm-wide ball raceways. Bearing design is inherited from [8] that ensures the rolling of microballs on smooth silicon surfaces due to the asymmetric release of the central rotor from top and bottom sides. The robustness of microballs provides a mechanically stable support mechanism while the rolling motion yields low friction and wear. The simplicity of bearing structure eliminates any external testing equipment required to support and actuate the rotor, resulting in an uncomplicated device operation. The decoupled nature of the stator and the rotor provided by the simple microball bearing

structure allows for the manufacturing of these components separately, which enables the integration of the rotor and stator by simply placing them on top of each other using a spacer in between. This configuration also results in easy access to the electrical components on the stator. In addition, the microball bearings embedded in the rotor provides a free rotating silicon platform accessible from the top side that simplifies the integration of the micro-turbo-generator with other possible system components.

Turbine blades   Permendur (FeCoV)

Microballs   NdFeB permanent magnets
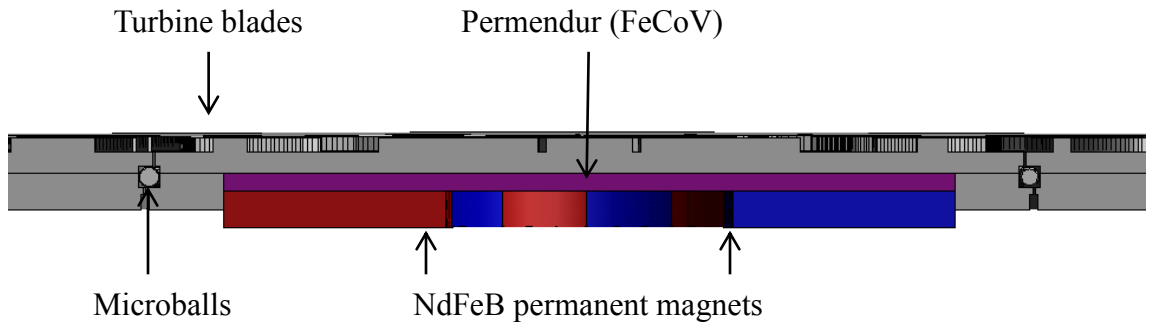
(a)
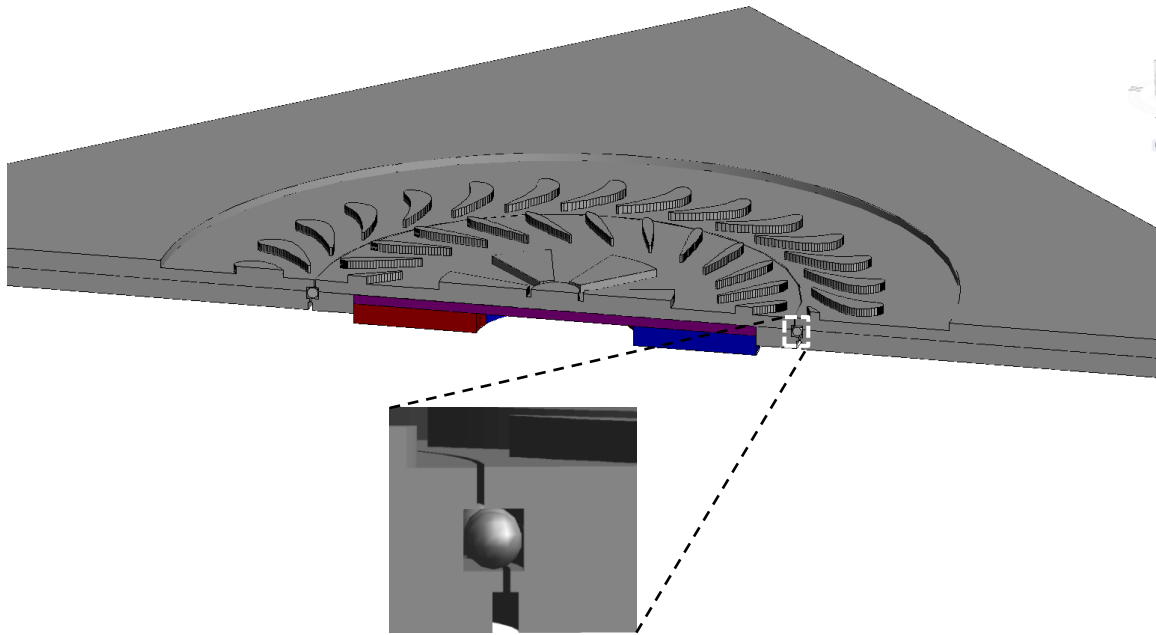
(b)

Figure 2.5. Schematic of the (a) side and (b) angled view of an 8 pole rotor with a close up
view of ball bearings.

A schematic picture of the complete generator with a plumbing wafer on top
is demonstrated in Figure 2.6. The effect of the design parameters such as number of
poles, turns per pole, and coil thickness on power are discussed in the following
sections of this chapter along with detailed analysis and simulations regarding the
device performance.
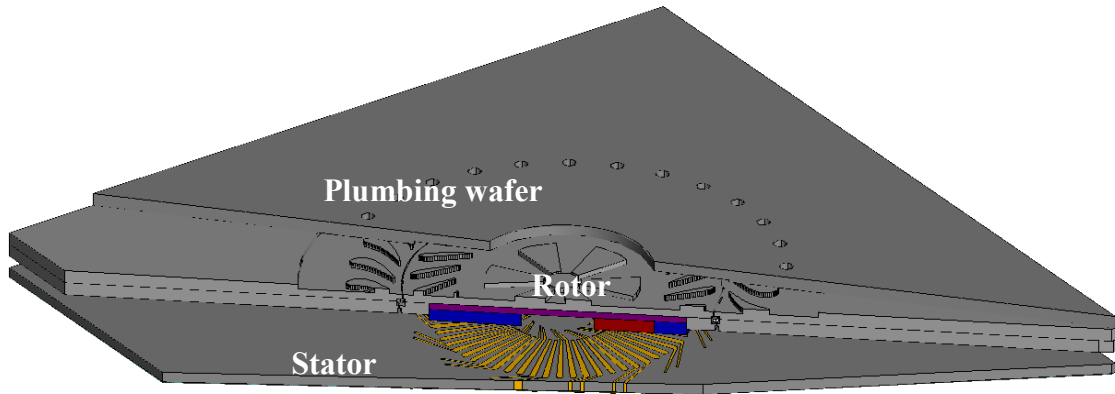
Figure 2.6. Angled view of the complete device.

2.3. Device Modeling

2.3.1. Equivalent Circuit Modeling

It is important to construct a device circuit model for defining the conditions for optimum power generation. The micro-turbo-generator generates voltage described by eq. 2-1, and therefore can be modeled as a voltage supply. Since the voltage is generated on the stator coils, the corresponding coil resistance and inductance should be taken into account. With these considerations, one phase coils can be modeled as a series connection of these circuit elements as shown in Figure 2.7 [129-131].
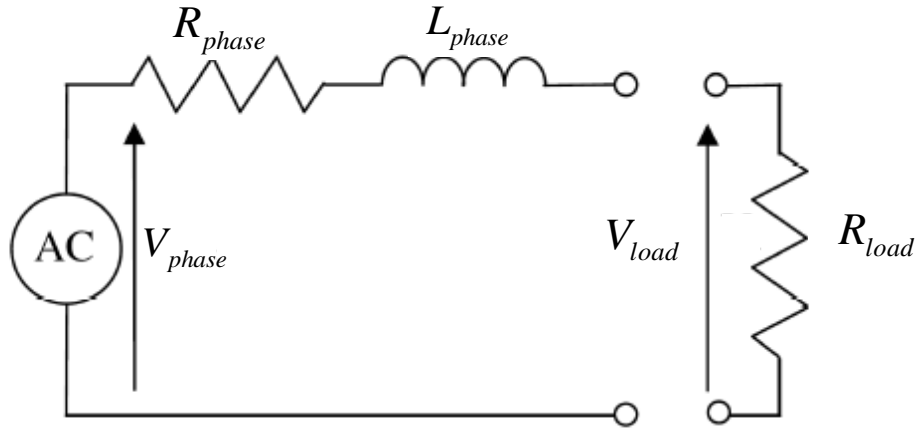
Figure 2.7. Equivalent circuit model of the micro-turbo-generator.

2.3.2. Open Circuit Voltage

The open circuit voltage given in eq. 2-1 (V_{phase} in Figure 2.7) should be further analyzed and expressed in terms of device parameters. To simplify this analysis, it is essential to derive the voltage for one coil loop in one turn of one phase with magnetic flux passing through it, shown schematically in Figure 2.8.
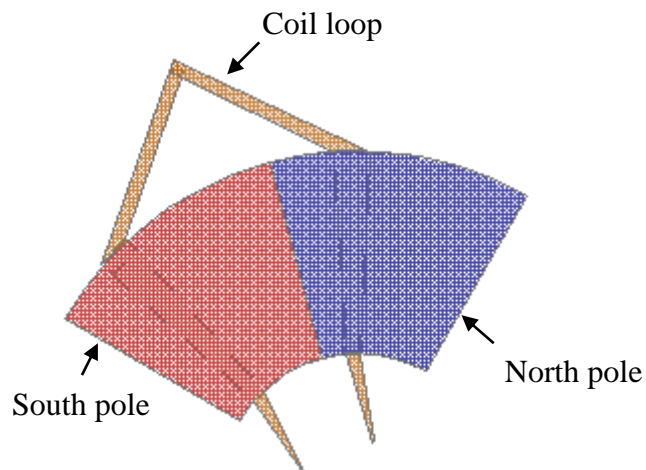
Figure 2.8. Schematic of one coil loop with two pieces of magnet on top.

Assuming the magnetic flux density around the rotor surface varies in a square waveform with amplitude B_g (the case where the magnet pieces are perfectly magnetized), the magnetic flux passing through the loop will generate a triangular wave with respect to time as shown in Figure 2.9.
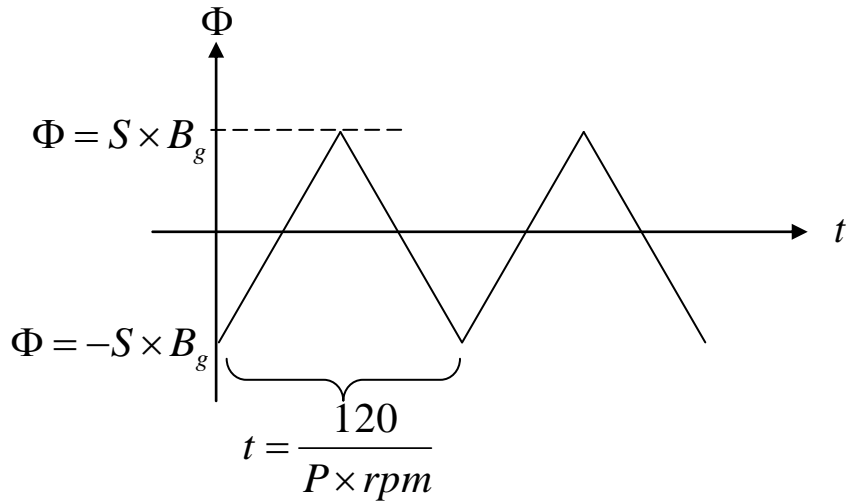
Figure 2.9. Variation of magnetic flux acting on one coil loop.

where S is the one magnet area, P is the number of poles, and rpm is the angular speed in rotations per minute. Since there are P poles, there will be $\frac{P}{2}$ triangles in one rotation, making the period to be $\frac{120}{P \times rpm}$. Therefore for one loop, eq. 2-1 becomes

$$V_{oneloop} = 2 \times S \times B_g \times P \times \frac{rpm}{60} \qquad (2\text{-}7)$$

Rewriting S as $\dfrac{\pi(r^2_2 - r^2_1)}{P}$ with r_2 and r_1 being the outer and inner radii of the

magnets respectively, and considering there are $\dfrac{P \times N}{2}$ of these loops in one phase for

a N turns per pole device, the peak voltage for one phase becomes:

$$V_{phase} = P \times N \times B_g \times \pi(r^2_2 - r^2_1) \times \frac{rpm}{60} \qquad (2\text{-}8)$$

This can also be derived from eq. 2-3. For any radial conductor under one pole, the

voltage will be $\int_{r_1}^{r_2} (\omega r \times B_g)\, dr$, where ω is the rotational speed in radians per second.

This integral yields $V_{conductor} = B_g \times \pi(r^2_2 - r^2_1) \times \dfrac{rpm}{60}$. The connection scheme for

one phase with N turns and P poles will then result in the total voltage given in eq. 2-8. The shifted nature of the phase turns causes the voltage to possess a gradually increasing profile rather than a square wave, as shown in Figure 2.10.
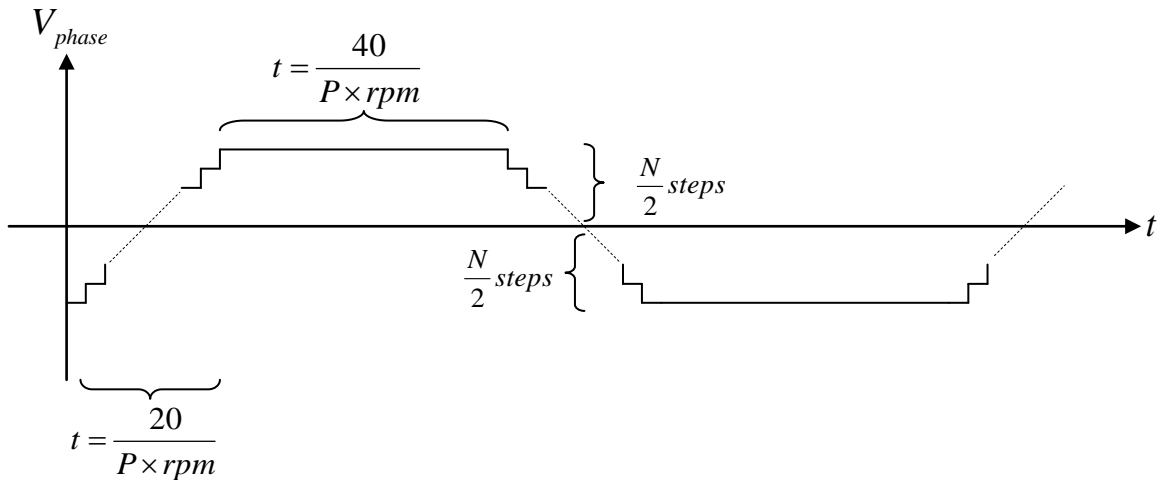
Figure 2.10. Generated voltage waveform under the assumption of perfect magnetization of magnets.

37

With leakage fluxes and a non-perfect rotor magnetization profile, the magnetic flux will deviate from a perfect square wave and the induced voltage will approach to a sinusoidal function with the amplitude given in eq. 2-8, where B_g becomes the average flux density. Note that, the amplitude of the induced voltage is linearly proportional with the speed, magnetic field, and the area. While the increase in these terms results in higher output power, the increase in $P \times N$ product does not affect the power, as will be discussed later in this chapter. However, it is best to maximize this product within the fabrication limitations in order to generate power at a high voltage and a low current. This will result in less power loss (due to diode voltage drops and $I^2 R$) in power conversion and/or extraction electronics.

2.3.3. Magnetic Field Distribution

A reluctance model is used to analyze the magnetic flux density term in eq. (2-8) for the estimation of open circuit voltage. The magnet pieces are assumed to be fully magnetized up to the remanence value B_r. Consider the cross section of the device as illustrated in Figure 2.11. While each domain is modeled with their corresponding reluctance, the permanent magnets are modeled as sources of remnant flux Φ_r in parallel with the magnet reluctance [80, 86, 129].
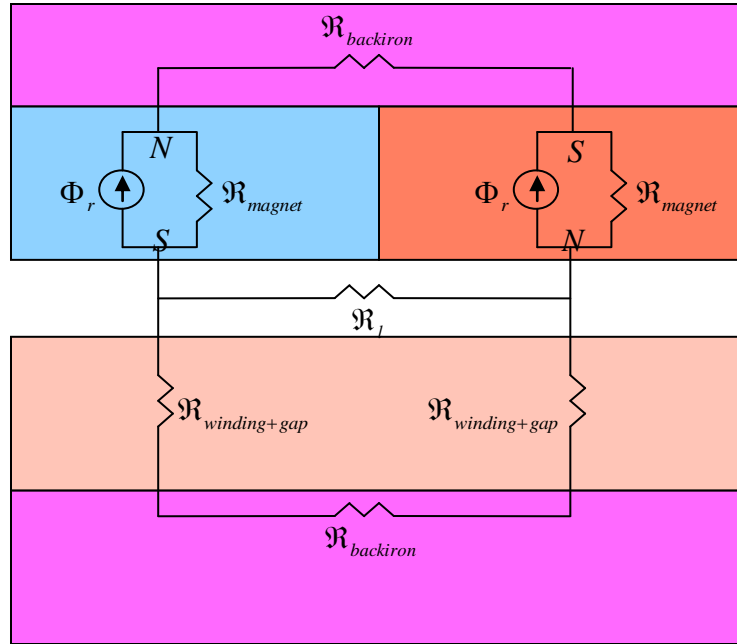
Figure 2.11. Device cross section showing the magnetic circuit components.

The $\Re_l$ represents the leakage flux and is ignored in the first order calculations. As the eventual goal is to integrate a permendur back iron on the stator backside in the future generations of this device, this component is included in the device analysis and optimization. By applying Thevenin's and Norton's theorems, the magnetic circuit can be reduced to the one shown in Figure 2.12.
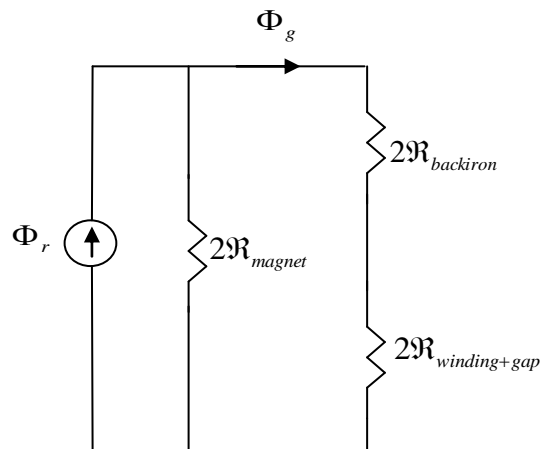
Figure 2.12. Simplified magnetic circuit representing the device.

Since the reluctances of the back irons are negligible due to their high permeability (

$$\Re = \frac{t}{\mu_r \mu_0 A}, \quad \mu_r \gg 1 \text{ for back irons, } \mu_r = 1 \text{ for the remaining domains}), \text{ the gap flux}$$

turns out to be $\Phi_g = \dfrac{t_{PM}}{t_{PM} + t_g} \Phi_r$, which leads to;

$$B_g = \frac{t_{PM}}{t_{PM} + t_{coil} + t_{gap}} B_r \tag{2-9}$$

Reexamining the output power, one will see that;

$$P \alpha \frac{V^2_{phase}}{R_{phase}} \alpha \frac{B^2_g}{\dfrac{1}{t_{coil}}} \alpha \frac{t^2_{PM} t_{coil}}{(t_{PM} + t_{coil} + t_{gap})^2} \tag{2-10}$$

It can be shown that the power is maximum when;

$$t_{coil} = t_{PM} + t_{gap} \tag{2-11}$$

This is the main reason why the coil thickness is chosen on the order of permanent magnet thickness within the fabrication limitations. An air gap of 50μm is also incorporated in the design as a safety zone to avoid a possible magnet-stator contact due to the surface roughness of the magnets. When a B_r value of 1.4T and t_{coil} value of 0.5mm are used in eq. 2-9, B_g and B^2_g are calculated to be 0.66T and 0.43T^2, respectively.

A more accurate magnetic flux density value and its distribution over the stator were found by using the finite element simulation software COMSOL which includes leakage fluxes and saturation effects into a three dimensional model. The remanence magnetic flux density of the NdFeB magnets was set to be $\pm 1.4T$ for north and south poles while a saturation flux density and relative magnetic permeability of

2.34T and 3200 were used for the permendur back iron, respectively [132]. To decrease the computation complexity, the saturation effect was only considered in the rotor permendur disc with a nonlinear model shown in Figure 2.13 since this effect is not expected to take place on the stator back iron due to its distance to the magnets. Under these conditions, the magnetic flux density normal to the surface of 500μm thick coils for an eight pole device is simulated and shown in Figure 2.14. Eight poles and 500 μm coil thickness are randomly chosen as an initial starting point in the analysis of the optimum pole number and coil thickness. The corresponding magnetic flux densities on the top and bottom surfaces of one coil loop are shown in Figure 2.14-a and -b, respectively.
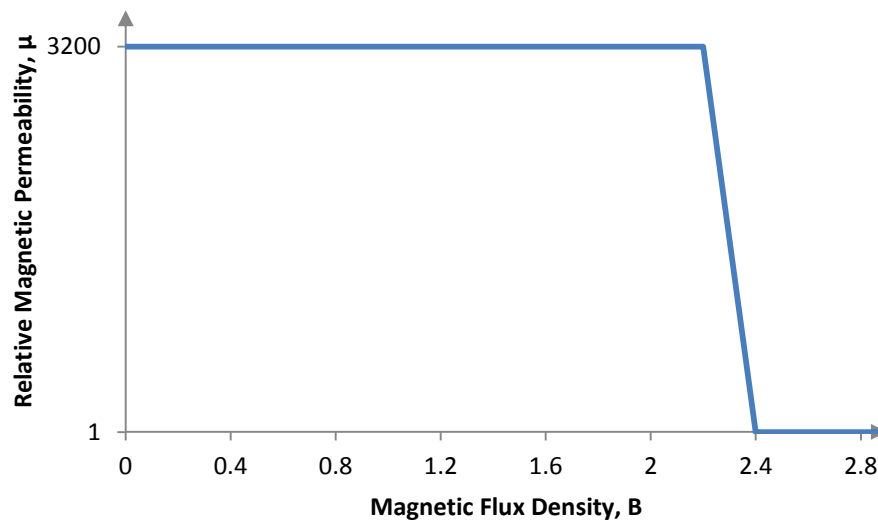
Figure 2.13. Simplified nonlinear model of permendur material for simulating saturation effects.
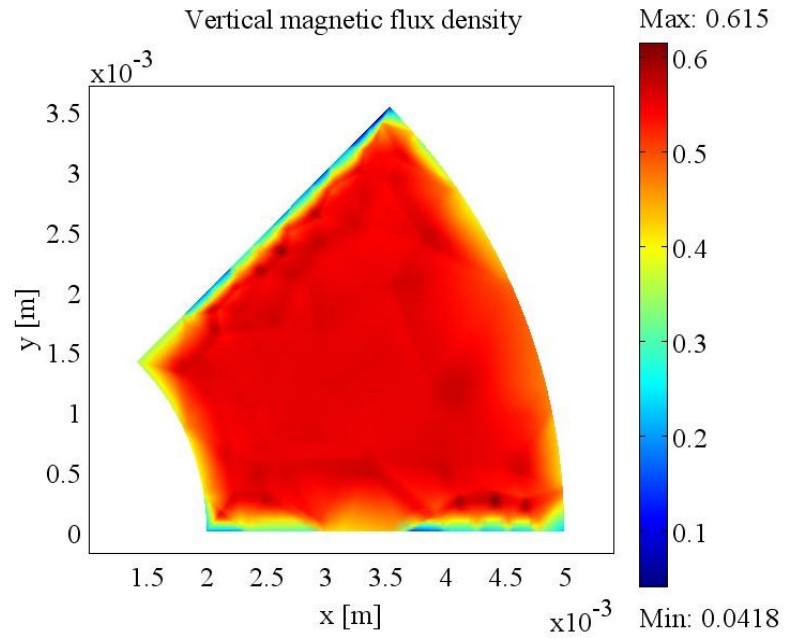
(a)
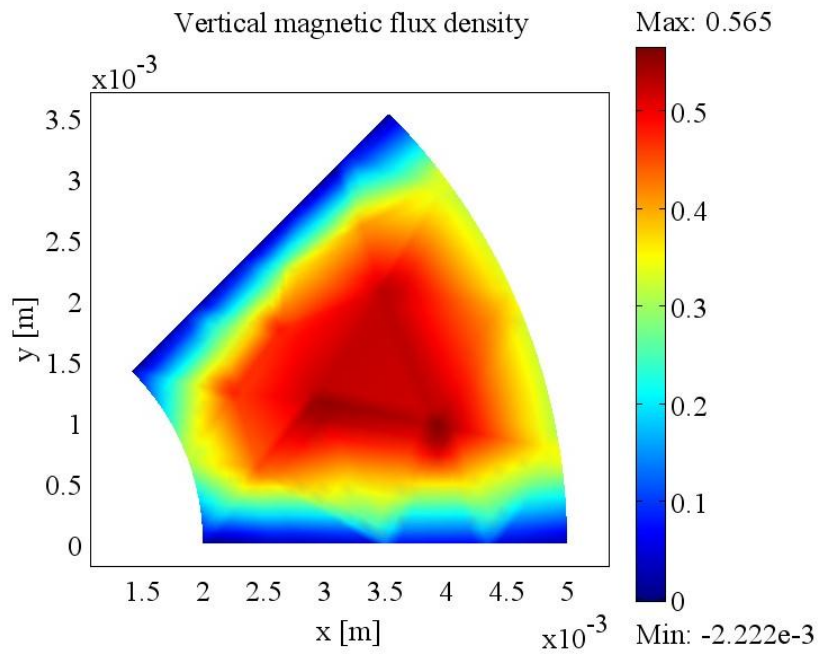
(b)

Figure 2.14. Magnetic flux density normal to the (a) top surface, and (b) bottom surface of a

coil loop from a 500μm-thick 8 pole stator.

It is apparent from the above figure that there is a significant difference between the values and distribution of top and bottom magnetic flux densities. As the number of poles is decreased, the number of north-to-south pole transition regions will likewise decrease, leading to less total leakage flux in the device. However, this will result in a higher degree of saturation in the permendur disc due to the increase in the pole area, and therefore magnetic flux per pole passing through the disc. The saturation effect can be reduced at large number of poles while simultaneously increasing leakage flux lost in the transition regions. The existence of these two competing effects suggests that there is an optimum number of poles that yields the most magnetic flux linked to the stator. Considering the difference between the magnetic fields through the top and bottom surfaces and dependence of power on the magnetic flux density (eq. 2-10), and assuming that the $P \times N$ product is maximized and roughly the same for the given rotor area, the best way to determine the optimum pole number is to compare the volume average of the magnetic flux density squared within a stator pole volume. Performing the same simulation with different pole numbers, the best value for 500μm thick stator was found to be 8 poles, as demonstrated in Figure 2.15.
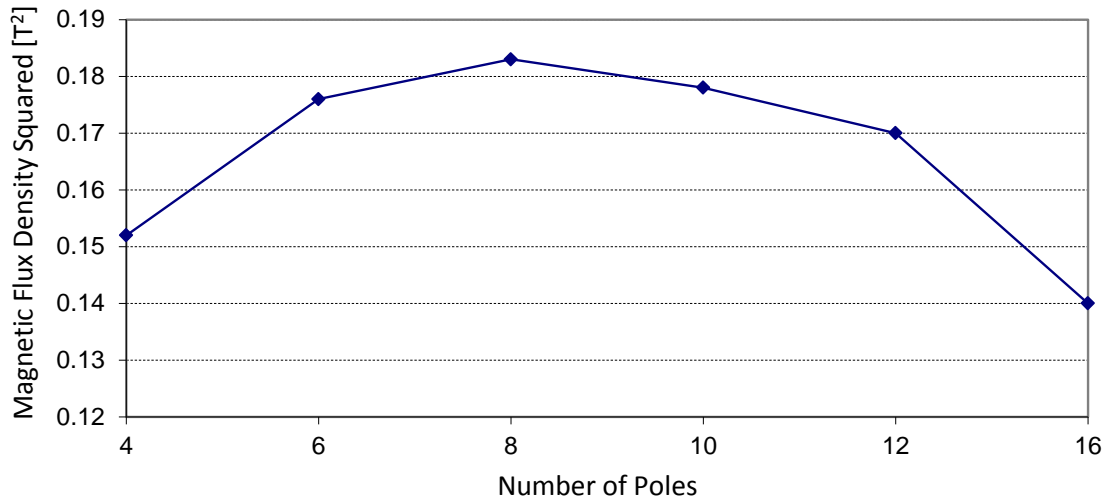
Figure 2.15. Volume average of magnetic flux density squared for 500μm thick coils.

The average values of B^2_g are lower than that estimated by the analytical model. This shows that both the leakage effect and magnetic saturation play quite a major role in decreasing the flux density with the given dimensions bound to fabrication limitations. The thickness of the stator, however, can be decreased to enhance the magnetic flux density as the flux density is mostly determined by the distance between the magnets and stator magnetic ring. This will, however, result in thinner coils that decrease the output power, since the power is proportional to the $B^2 \times t_{coil}$ (eq. 2-10). This shows that there is an optimum stator coil thickness that would yield the maximum electrical power. To find this thickness, the simulations are repeated for different coil thicknesses and numbers of poles and the values of $B^2 \times t_{coil}$ for each simulation are compared (Figure 2.16).
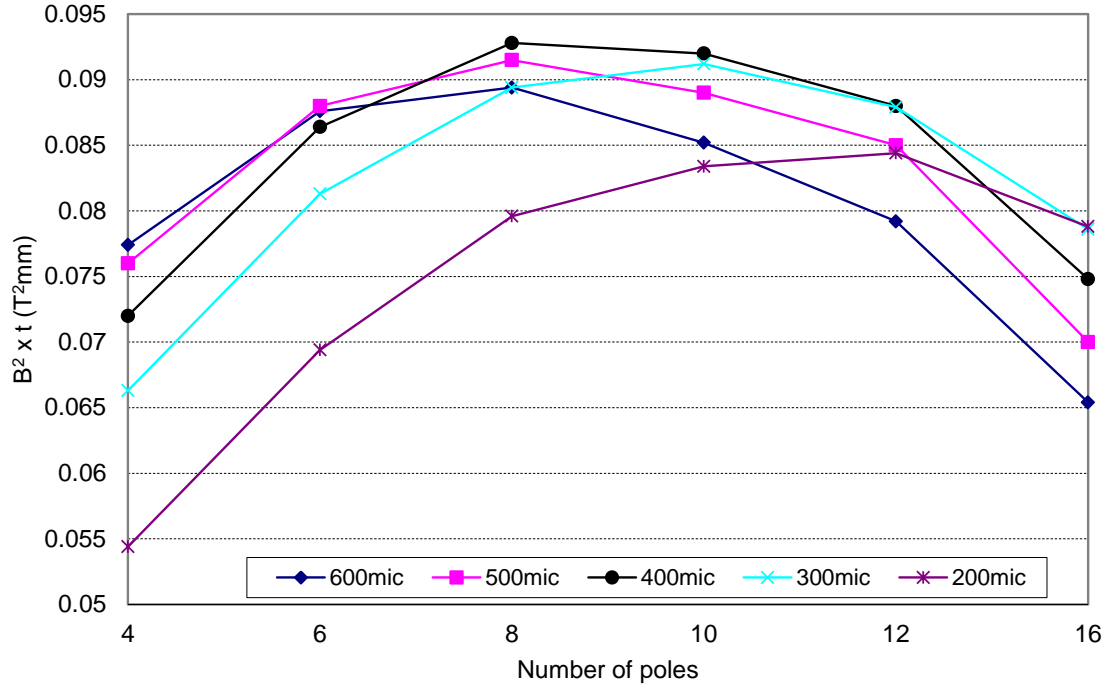
Figure 2.16. The multiplication of the volume average of magnetic flux density squared and

stator thickness for various coil thicknesses and number of poles.

These graphs show that given the magnet and rotor disc dimensions, the maximum $B^2{}_g \times t_{coil}$ is obtained with 400μm coils. Therefore, the thickness of the stator wafer is set to be 400μm. Based on the graph shown in Figure 2.16; three devices with 8, 10, and 12 poles yielding the maximum $B^2{}_g \times t_{coil}$ are designed. The 10 pole design yields the maximum power while 8 pole and 12 pole designs yield a higher efficiency due to lower eddy current loss (explained in the following subsections) and less I^2R loss due to higher voltage/lower current generation, respectively. Discussions on these aspects, excluding the I^2R loss which depends on the power electronic circuitry and components, are given at the end of this chapter. Using COMSOL, the corresponding average magnetic flux density (B_g) values are

calculated to be 0.461T, 0.453T, and 0.441T, for 8 pole, 10 pole, and 12 pole designs, respectively. Turns per pole values are determined by the fabrication process that limits the total number of radial coils to approximately 100. Therefore, *three different three phase micro-turbo-generators are designed with 8 poles - 4 turns per pole, 10 poles - 3 turns per pole, and 12 poles - 3 turns per pole with 400μm stator coils.* In addition to the three main designs, a fabrication safe (10 pole 2 turns per pole 3 phase) and a fabrication risky (12 pole 9 turns per pole 1 phase) device are also designed. While 10 pole 2 turns per pole device is simpler to fabricate due to fewer number of radial coil lines, 12 pole 9 turns per pole 1 phase device is more difficult to fabricate and yields the maximum generated voltage.

2.3.4. Effect of The Exclusion of Stator Back Iron

Although included in the design for future implementations, the first generation of the micro-turbo-generator presented in this dissertation does not include a stator back iron, mainly for normal force concerns explained later in this chapter. Accordingly, it is essential to perform similar magnetic flux distribution simulations for performance estimates of the three device designs. The effect of the exclusion of this component arises from the increase in the magnetic reluctance of the stator, which corresponds to the increased $\Re_{backiron}$ value of the stator backside in Figure 2.11. This, in turn, adds to the total resistance of the rightmost branch of the equivalent circuit shown in Figure 2.12. Finally, the flux passing through the magnets increase while the flux within the stator (Φ_g), and hence the magnetic flux density, decrease to keep the voltage equal on the two branches. As the model presented in

46

Figure 2.12 is simplified and does not take the leakage fluxes and magnetic saturation into account, it is best to observe this effect in COMSOL normal magnetic flux density simulations on top and bottom surfaces of a coil loop shown in Figure 2.17. For this simulation, the design with 8 pole 400μm-thick stator is randomly chosen amongst others discussed above.
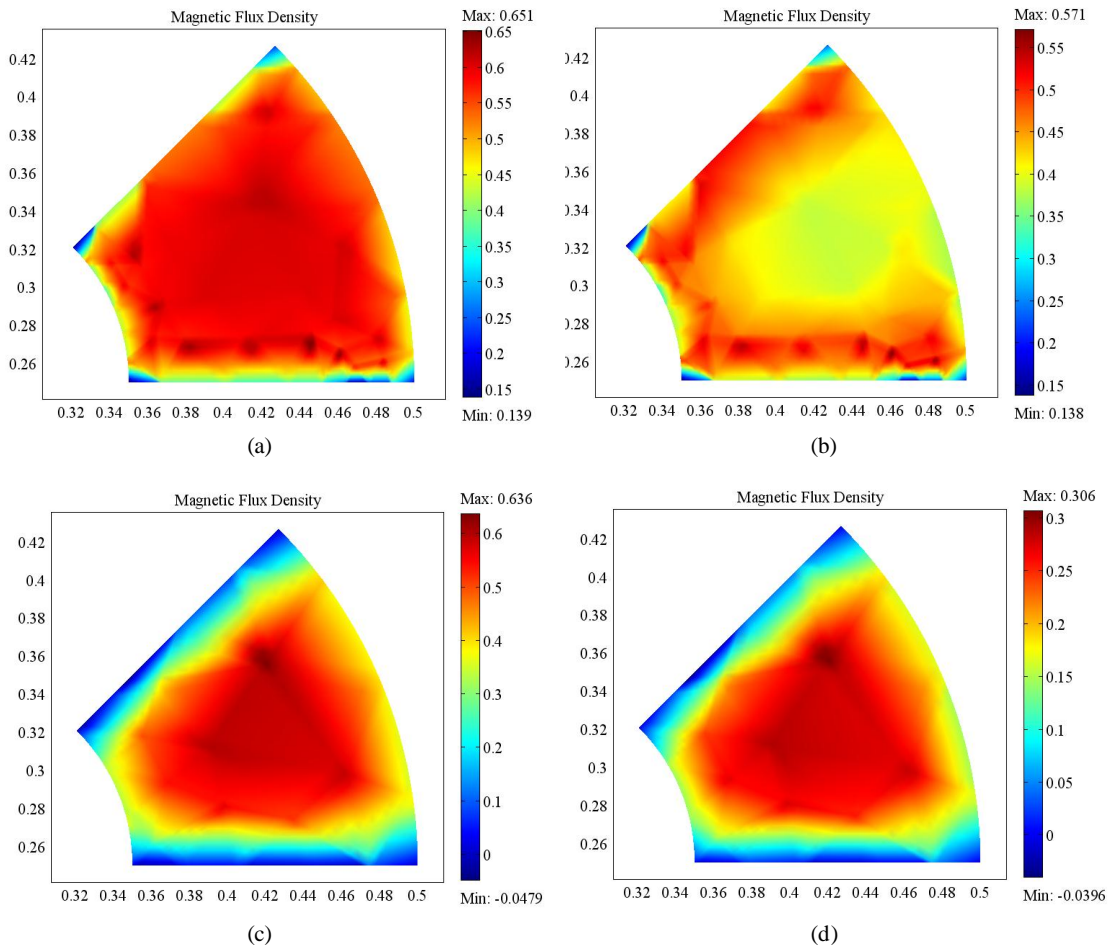
Figure 2.17. Magnetic flux density normal to the top surface of one coil loop (a) with back iron, (b) without back iron, and bottom surface of one coil loop (c) with back iron, and (d) without back iron of an 8 pole stator with 400μm thickness.

Figure 2.17 clearly shows the reduction in the maximum magnetic flux density values on both the top and bottom coil surfaces of the stator without a permendur back iron. As the difference in the peak flux density values is on the order of 10% on the top surface, the percentage significantly increases through the stator thickness down to the bottom surface. In addition to this expected result, another major difference is the flux density profile on the top coil surfaces. While the magnetic field is mainly uniform on the stator with permendur back iron, a non-uniform profile with relatively sharp peaks on the edges are observed for the stator without a permendur back iron. This is also expected as the field will intensify on the closest path possible, which is between the edges of neighboring magnetic poles. When these effects are combined, a substantial drop in the magnetic field (normal to the stator surface) arises. The volume average of magnetic flux density squared for the stators with and without a permendur back iron are calculated to be $0.232 m^3 kg^2/s^4 A^2$ and $0.096 m^3 kg^2/s^4 A^2$, respectively, representing a 59% reduction.

An analysis for optimum pole number and thickness, similar to that presented in Figure 2.16, was performed for the stators without a permendur back iron, and is shown in Figure 2.18. Due to the absence of this component, both the coil resistance and the average flux density squared favor an increase of the stator thickness over the thickness range of interest. In parallel, saturation and leakage effects are also observed for each different simulation. As the results presented in Figure 2.18 do not change the current design, it sheds light on the optimum device structure if a back iron is excluded from the device design.

48
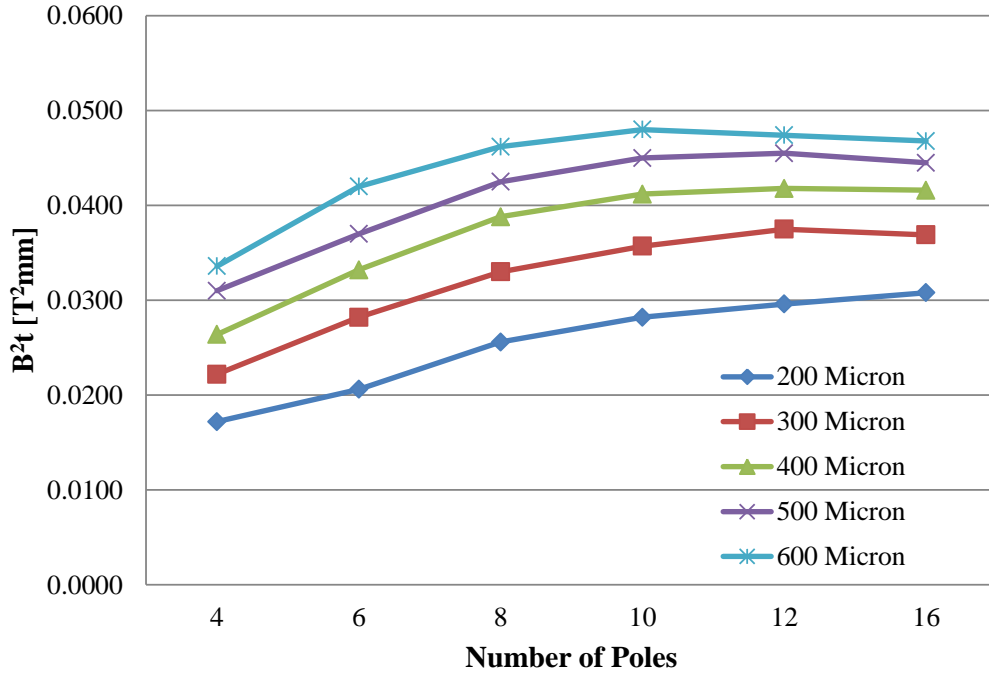
Figure 2.18. The multiplication of the volume average of magnetic flux density squared and thickness for various coil thicknesses and number of poles for a stator without a back iron.

2.3.5. Coil Resistance

The resistance of the different parts of one loop has different resistances and should be calculated separately (Figure 2.19). While $R_{coil} = \int_{r_1}^{r_2} \dfrac{\rho dr}{2\pi t r \dfrac{\theta}{360}}$ is used to find the resistance of the coil, the remaining resistances can be found by the simple formula $R = \dfrac{\rho l}{A}$, where ρ, θ, t, l, A are the resistivity, conductor angle, thickness, length, and cross sectional area, respectively. The resistance of one phase will then be,

$$R_{phase} = N \times P \times (R_{coil} + R_1 + R_2 + R_{c1} + R_{c2}) \qquad (2\text{-}12)$$

49
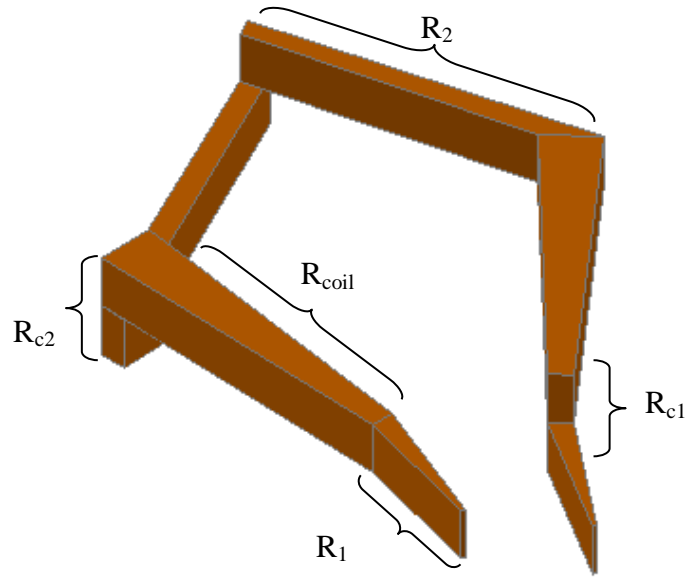
Figure 2.19. Different resistance components of one coil loop.

where R_1, R_2, R_{c1}, R_{c2} are the inner end turn, outer end turn, inner connection, and outer connection resistances, respectively. For a given volume, the $P \times N$ product and the total resistance are not independent from each other. To increase the voltage by increasing the $P \times N$ product, the coils should be equally longer. Moreover, the coils should be narrowed with the same scale factor to fit more of them in the available space. Multiplying $P \times N$ with a scale factor k therefore increases the voltage and resistance by k and k^2 times, respectively, cancelling the effect on maximum power as given by eq. 2-5. However for the same $P \times N$, the power can be slightly increased by using less number of turns and higher number of poles as the total phase resistance will be lower due to the inverse proportionality between the number of poles and R_1 and R_2.

The skin effect needs to be considered at speeds up to 100krpm, which is at the high end of the speed range of this device, and the resistance equation should be modified accordingly. Skin depth for a good conductor is given with the following formula:

$$\delta = \frac{1}{\sqrt{\pi f \mu \sigma}} \qquad (2\text{-}13)$$

where μ, σ, f are permeability, conductivity, and electrical frequency of the generated waveform. For a microgenerator rotating at a specific rpm, the electrical frequency will be:

$$f = \frac{rpm}{60} \times \frac{P}{2} \qquad (2\text{-}14)$$

If a pole number of twelve is considered (highest generated frequency), the skin depth at 100krpm will be 650μm, that is larger than the width and the depth of the conductors. This leads to the conclusion that the difference between the AC and DC resistances are negligible. As this analysis provides a basis for the estimation of phase resistances, fabrication effects such as variety in metal deposition processes and misalignments play important role in significantly altering the expected resistance values. As the expected values are on the order of 1 ohm, it is difficult to predict the exact phase resistance of each design due to these effects.

2.3.6. Coil Inductance

The inductance of the coils can be found by multiplying the per loop inductance by $\frac{NP}{2}$. Assuming a current of I flows through the loop shown in Figure

2.19, the inductance can be calculated by taking the ratio of the flux through the loop

generated by the current to the current itself, i.e. $L_{loop} = \dfrac{\Phi}{I}$. The flux, Φ, however is

difficult to calculate due to the complex geometry of the loop. Therefore COMSOL

software is used to calculate the total flux passing through the coil surface (Figure

2.20). The simulation has been performed for a device with 12 poles, however the

results are similar for all other devices as the area of the loop slightly changes for

each different design.
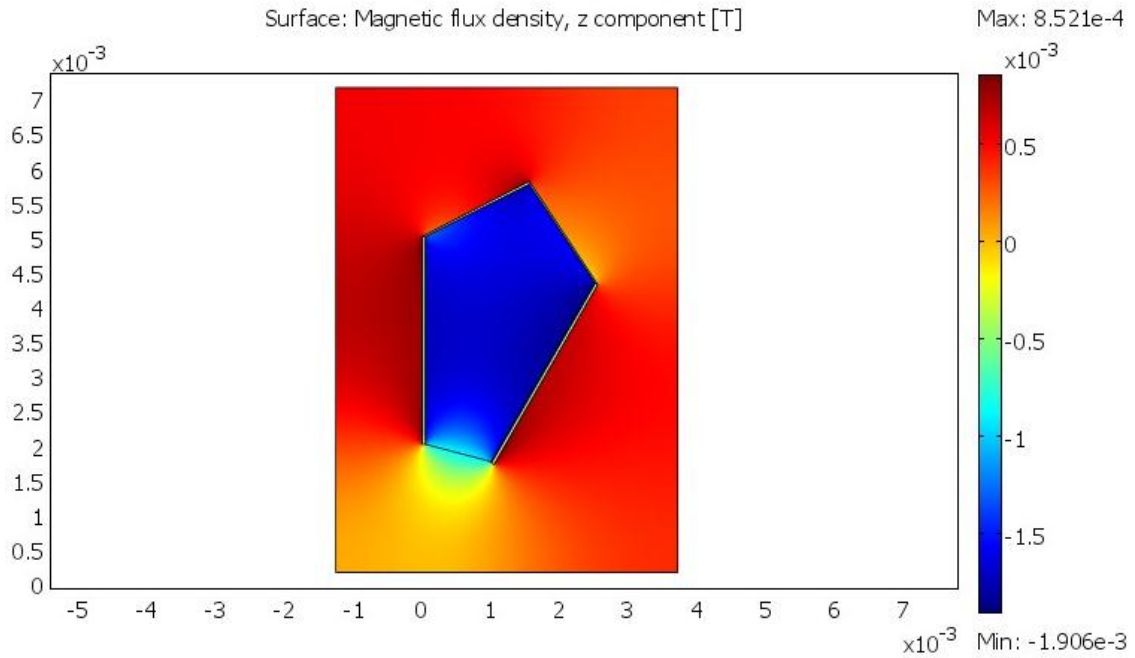
Figure 2.20. The simulation result for calculating inductance. 1A current is passing through

the coil loop and the flux density is integrated over the coil surface to find the flux value.

1A current results in 10.7nWb on the coil surface. This shows that per loop

inductance of a 12 pole device is 10.7nH. At the maximum speed of 100krpm, which

corresponds to the electrical frequencies up to 10kHz (eq. 2-14), the impedance of the phase inductance reaches $\omega L \approx 12m\Omega$. In addition to the inductance of each coil, there are mutual inductances between different coils. Since both the calculation and the simulation of this effect is computationally complex, the total inductance will be determined experimentally. However, the final inductance value is still expected to be on the order of milliohms. This value is much smaller than the expected per turn phase resistance on the order of ohms and therefore, the inductance is omitted from the model given in Figure 2.7. The simplified model resulting from this analysis is given in Figure 2.21.
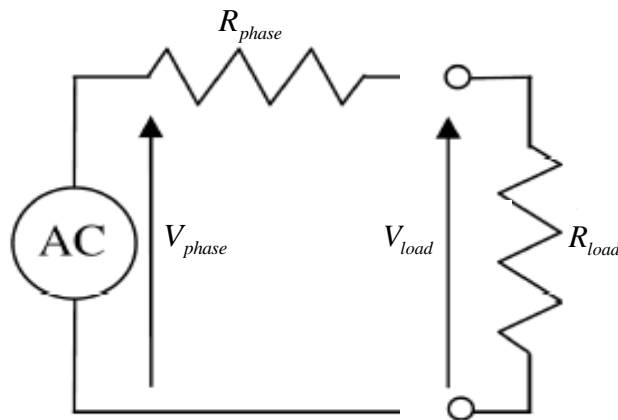
Figure 2.21. Simplified device model: V source in series with R_{phase}

In large scale systems, the situation is exactly the opposite; the resistance of the coils is negligible compared to the inductance given a certain stator design. This contradicting result can be explained by scaling laws. If we take a simple circular wire loop with circumference l, cross sectional area A, wire radius a, and a radius r, the resistance and inductance of this wire is $R = \dfrac{\rho l}{A}$ and $L = r(\ln\dfrac{8r}{a} - 2)$,

respectively [129-131]. If we scale every dimension by a factor of k, then the resistance goes up by a factor of k while the inductance goes down by the same factor. Therefore on the MEMS scale, resistance is the dominant factor in coil impedance.

2.3.7. Power

The per phase maximum AC power generation will be achieved by connecting a resistive load with a resistance matching that of the coils. Under these conditions with a sinusoidal voltage $V_{phase} \sin(wt)$, the delivered per phase RMS power is calculated with eq. 2-15 below;

$$P_{phase,\max rms} = \frac{(\frac{V_{phase,rms}}{2})^2}{R_{phase}} = 0.125 \frac{V^2{}_{phase}}{R_{phase}}$$ (2-15)

The maximum per phase AC power achievable with this device depends on the phase resistance, device area, magnetic flux density, and rotational speed as indicated by equations 2-8 and 2-15. With all the optimizations presented in the previous sections based on the theoretical analysis and simulations, the device is capable of generating a per phase AC output power on the order of 1W at the maximum estimated speed and phase impedance of 100krpm and 0.1Ω, respectively. The maximum power is mainly defined by the restrictions in the fabrication technology limiting the device dimensions to cm-scale, and by the bearings providing necessary stability and robustness up to 100krpm. As it is difficult to push the fabrication limits to fabricate larger devices, higher output power levels will be

achievable through improvements in the bearing design that are explained in Chapter 4.

Connecting a three phase diode bridge rectifier, the generator can deliver a DC voltage with ripples. Assuming the diodes instantaneously turn on and ignoring the voltage drops on the diodes, the maximum DC output power can be found by eq. 2-16 [133]. These voltage ripples on the load can be suppressed by using an inductor. The delivered power will, however, be less than the calculated values due to the power dissipation in the diodes and external connections.

$$P_{DC,\max} = \frac{[\sqrt{3}V_{phase}\sqrt{0.5 + \frac{3\sqrt{3}}{4\pi}}]^2}{8R_{phase}} \approx 0.342\frac{V^2_{phase}}{R_{phase}} \tag{2-16}$$

2.3.8. Armature Reaction

The magnetic field created by the stator currents can be found similar to the inductance analysis. Eq. 2-8 and 1Ω (lower end of the expected range) per turn for a 12 pole device suggests that the expected current in the device is on the order of 1A. When this current is simulated in COMSOL, an average magnetic flux density of 1.5mT is obtained per loop, generating an armature reaction of 4.5mT which is very small compared to the flux density from the magnets. Therefore, the effect of armature reaction on the total axial flux distribution over the stator is neglected.

2.3.9. Loss Mechanisms

Eddy Currents are the most dominant power loss mechanism in this micromachine. These are the currents induced in the stator back iron due to the time

varying magnetic field passing through the material. This effect will not be observed in this work due to the absence of the stator back iron, but is explained here for future implementations. The dissipated power due to the eddy currents can be estimated with the formula [134]:

$$P_{eddy} = \frac{1}{6\rho}\pi^2 t^2 f^2 B_m^{\,2} V \qquad (2\text{-}17)$$

where t is the width (in this case, the thickness), f is electrical frequency, B_m is maximum flux density and V is the total volume of the material. Using eq. 2-17 together with eq. 2-14 and the maximum azimuthal flux density in COMSOL simulations, the eddy current loss at the maximum speed of 100krpm for a future generation device with stator back iron for the 8 pole, 10 pole, and 12 pole designs are determined to be 2.7W, 3.7W, and 4.6W, respectively. These values are provided to demonstrate how significant such losses can be in future implementations. Eddy currents are induced in copper coils as well and can be described by the same equation (eq. 2-17). While it is difficult to calculate this loss due to the complex geometry and structure, it is still expected to be negligible due to the laminated structure of the stator coils.

Hysteresis loss is the energy loss due to the change in orientation of the magnetic domains in the high permeability material, in this case stator permendur back iron. The per volume energy loss is the area in the B-H curve of the specific material. Approximating this area by $4H_c B_{sat}$ (the original value is less than this value), the power loss in the to-be-integrated stator back iron will be

$P_h = 4H_c B_{sat} \times V \times f$, where H$_c$ is the coercive force. The H$_c$ and B$_{sat}$ are 31.83A/m

and 2.34T, respectively [135]. For a non-saturated back iron with a maximum

azimuthal flux density of B$_\Phi$, this equation can be written as;

$$P_h = 4H_c B_{sat} \times V \times f \times \frac{B^2{}_\Phi}{B^2{}_{sat}}$$ (2-18)

The hysteresis loss of 8 pole, 10 pole, and 12 pole machines at 10krpm are calculated

to be 0.026W, 0.028W, and 0.029W, respectively. These values are negligible

compared to the eddy power loss, and again will not be observed in this first device

implementation.

Winding loss is the $I^2 R$ losses in the stator coils. At the matched load

condition, the lost power will be equal to the delivered power given in eqs. 2-15 and

2-16. For other loads, the power dissipation in the coils can be calculated by eq. 2-19

below:

$$P_w = (\frac{R_{phase}}{R_{phase} + Z_{load}} \times V_{phase,rms})^2 \times R_{phase}$$ (2-19)

Mechanical power loss (P$_{mech}$) is the dissipated power in the bearings in the

form of friction. The frictional loss depends on the normal force and speed. The

previously developed model in [122] is used to calculate this loss, which can be

written as;

$$P_{mech} = krpm^2 \times F_N{}^{0.444} \times 10^{-5}$$ (2-20)

where krpm is the rotational speeds in kilo rpm, and F_N is the normal force in mN on the rotor. At maximum speed of 100krpm and an estimated normal load of 1N, the mechanical power becomes 2.14W. In addition to friction, mechanical power loss also includes viscous drags in the rotor. Calculations in [122-125] show that the friction torque per rotational speed associated with viscous drag in a similar microturbine rotor with 5mm radius and no integrated magnetic materials is $1.25 \times 10^{-11} \frac{Nm}{rpm}$ that corresponds to 13mW power dissipation at 100krpm. As the viscous drag force is proportional to the device area, device miniaturization benefits from the reduction in viscous drag forces.

2.3.10. Torque

The eq. 2-5 can be rewritten to account for all the power delivered to the load and the power dissipated through the loss mechanisms. With these additions, the required torque to drive the rotor turbine will be;

$$T = \frac{P_e + P_{ring,eddy} + P_{coil,eddy} + P_h + P_w + P_{mech}}{\omega} \qquad (2\text{-}21)$$

2.3.11. Normal Force

Normal force is an important parameter to examine that determines the load in the ball raceways, and hence the long term reliability of the device. There are two main contributors of normal force, namely the inherent normal force due to the pressurized gas flow and the normal force due to magnetic forces. The former has been investigated in [122] and the frictional torque versus speed and normal force

data has been presented. The magnetic forces present in the machine are due to the repulsion between the rotor magnets and the magnetic field created by the stator currents, and the attraction between the rotor magnets and the stator back iron. The simulation results using COMSOL shows that the coil current-magnet interaction with a 1A coil current yields a negligible total repulsion force on the order of 2mN while the magnet-stator back iron attraction produces a net force of 5N. *Since this high force will result in excessive wear and friction on the bearings, it is excluded from this first device implementation and may be integrated later with future enhancements in the encapsulated ball bearings.* It is quite difficult to estimate the gas flow-induced normal force due to the complex relationships between the friction, total normal force and required flow rate. However, given the results presented in [122] and depending on the packaging and the operational speed, the force is expected to be on the order of 100mN-1N which is suitable for this application.

2.3.12. Efficiency

The efficiency of the whole system is simply written as:

$$\eta = \frac{P_e}{P_e + P_{ring,eddy} + P_{coil,eddy} + P_h + P_w + P_{mech}} \qquad (2\text{-}22)$$

For an ideal lossless system, the theoretical maximum efficiency is 50% that corresponds to the matched load condition (the case where winding losses are equal to the delivered power) as mentioned previously. Among the other loss contributors, the back iron eddy currents on the stator are the most dominant, and will be avoided due to the exclusion of the stator permendur back iron.

59

2.4. Systems Integration

Integration with other components such as a miniature combustion engine, a shaft, or electronic elements requires a systems approach in the design process. Although the focus of this work is to demonstrate the first working micro-turbo-generator, the following design aspects should be considered in the next phase of this technology that will aim systems-level integration of various components.

2.4.1. Mechanical Aspects

To convert high-density hydrocarbon energy into electricity, the micro-turbo-generator should be eventually coupled to a similar-scale combustion engine either through gas exhaust, or by using a shaft that can spin the rotor. When direct gas exhaust is used to actuate the rotor, an additional component should be developed to filter the input flow and remove other contaminants, such as oil, that can potentially affect the performance of the micro-turbo-generator. In addition, thick oxide layers should be used to increase the thermal resistance and to prevent temperature rise in the bearings and permanent magnets. Specifically, the temperature of the permanent magnets should be less than their curie temperature, which is 80ºC for the high-grade NdFeB used in this work, to maintain the remanence magnetic field that facilitates electromagnetic voltage induction.

When the rotor is actuated by the shaft of a combustion engine, mechanical issues including vibration and high normal loads (>1N) that would result in excessive friction and wear should be considered in the device design. While the similar microturbine rotors in [122-125] can support normal loads on the order of 1N, radial

strength of such devices has not been characterized. To extend the range of normal loads and vibrations that the micro-turbo-generator can withstand, bearing design should be improved to increase the contact area between the microballs and the bearing raceway, which is discussed in Chapter 4.

2.4.2. Materials Aspects

Device materials should be carefully selected based on the operating conditions of specific applications. Bearing material system may be altered from silicon and stainless steel to other materials that have closely-matching hardness to decrease the wear in the device. Due to the possible vibrations in the overall system, permanent magnet materials can be changed from NdFeB to SmCo, or AlNiCo that are less fragile. The same materials can also be selected for their higher curie temperatures for applications with elevated operating temperatures. In addition to the magnet materials, stator coils can also be made from other metals to decrease the difference between the coefficient of thermal expansions of the coil metal and silicon. This can decrease the possibility of wafer cracks at high operating temperatures.

Temperature considerations are also important in the monolithic integration of the micro-turbo-generator and other electronic components. If the electronic components are to be integrated on the silicon rotor or the stator, these components should be fabricated first as most CMOS fabrication processes involve very high temperatures that can result in the loss of remanence magnetic field, and fracture on the stator. Alternatively, these electronic components can be integrated on the micro-turbo-generator using epoxy or flip-chip bonding.

2.5 Design Summary and Estimated Performance

The critical device dimensions were determined by considering the above discussions and fabrication limitations, and summarized in Table 2.1. Given the geometry, the performance of each different design was estimated using the developed models and simulations detailed above, and given in Table 2.2.

Parameter	Value
Inner radius (active layer)	2mm
Outer radius (active layer)	5mm
NdFeB magnet thickness	0.5mm
Number of poles/ turns per pole	8/4, 10/3, 12/3, 10/2, 12/9
Rotor permendur back iron thickness	0.25mm
Stator permendur back iron thickness	-
Stator coil thickness	0.4mm
Air gap	50μm

Table 2.1. Critical device parameters

	P=8 N=4	P=10 N=3	P=12 N=3	P=10 N=2	P=12 N=9
Phase voltage (V)	$0.0104 \times$ krpm	$0.010 \times$ krpm	$0.0112 \times$ krpm	$0.0067 \times$ krpm	$0.0336 \times$ krpm
Maximum three phase AC power (W)	$0.45\text{e-}4 \times$ $krpm^2/\Omega$	$0.43\text{e-}4 \times$ $krpm^2/\Omega$	$0.57\text{e-}4 \times$ $krpm^2/\Omega$	$0.19\text{e-}4 \times$ $krpm^2/\Omega$	$1.64\text{e-}4 \times$ $krpm^2/\Omega$
Winding loss (matched load) (W)	$0.45\text{e-}4 \times$ $krpm^2/\Omega$	$0.43\text{e-}4 \times$ $krpm^2/\Omega$	$0.57\text{e-}4 \times$ $krpm^2/\Omega$	$0.19\text{e-}4 \times$ $krpm^2/\Omega$	$1.64\text{e-}4 \times$ $krpm^2/\Omega$
Mechanical loss (W)	< 0.2W (estimated)	< 0.2W (estimated)	< 0.2W (estimated)	< 0.2W (estimated)	< 0.2W (estimated)

Table 2.2. Performance values as a function of rotational speed. P represents the number of poles and N represents the turns per pole parameters.

3. Fabrication

This chapter explains the microfabrication of the micro-turbo-generator along with a novel process technique developed for the realization of wafer-thick stator coils. Fabrication has been one of the most challenging aspects of this doctoral work due to the complicated device geometry and the large number of different components and device layers. Initially, the process flow used a total of 20 optical masks. However during the course of device development, total number of masks was decreased by making some simplifications in the device structure at the expense of performance in order to demonstrate the first working device. The final process flow used a total of 15 masks with 110 process steps, which illustrates the complexity in device microfabrication.

3.1. Stator Fabrication

The stator shown in Figure 2.4 is composed of three-phase planar copper coils integrated in a low-resistivity silicon substrate. Due to the geometrical limitations in the connection scheme, more than 80% of the coil structures are integrated in the silicon substrate while the remainder connections are patterned on the substrate backside. To maintain a relatively uniform geometry during the electroplating process, which will be described in subsequent sections, large-area electrical pads that are used to extract generated power are not integrated in the substrate and are fabricated on the backside. This also makes the testing scheme simpler which is described in Chapter 4.

3.1.1. Novel Process Development: Bottom-Up Electroplating with Planar Surfaces

Fabrication of thick (>10µm) metal structures in MEMS is most commonly possible with the electroplating technique. Accordingly, this method is used for the microfabrication of three-phase copper coils in the stator component. In this process, the desired metal is electrodeposited in a mold by applying potential difference between the plating site and a metal anode in an electroplating solution that contains the metal ions of interest. Due to the required copper thickness of 400µm with aspect ratios on the order of 16, a readily available silicon substrate is preferred as a plating mold over other polymers including SU-8 and KMPR. A bottom up electroplating technique was previously reported in [136, 137] to fabricate such thick structures with high aspect ratios in silicon, and thus suits best for the manufacturing of stator coils. However, due to the problems associated with after-plating processes resulting in cracks in the plated metal, a new electroplating method improving upon this bottom up technique has been developed [138].

For this process, low bow (<10µm) p type, low resistivity (1-10Ωcm for electrical isolation), <100> silicon wafers were selected as the substrate. Initially, test patterns were created in the top wafer using deep reactive ion etching (DRIE) with the recipe given in the Appendix section. These through etched structures were then oxidized using thermal oxidation to provide electrical isolation of radial test structures. Although the substrate is not very conductive, a 0.3µm thick good quality oxide film ensures complete electrical isolation between the etched patterns. This

wafer is used as a mold for the subsequent electroplating process, and is referred to as the **_mold wafer_**.

Another wafer, referred to as the **_seed wafer_**, was prepared in parallel as part of the bottom up electroplating process. 1.5μm-thick Shipley 1813 photoresist was first spun on the seed wafer for easy detachment later in the process. The photoresist on the edges of the seed layer wafer was removed to avoid photoresist build-up on the wafer periphery and maintain a constant layer thickness throughout the wafer. Next, a 0.1μm thick gold seed layer was deposited on the seed layer wafer over the photoresist layer. The gold on the very edges of the wafer was etched away to prevent lateral copper growth on the sides of the wafer during the electroplating. A second layer of 1.5μm thick photoresist was spun on gold and the two wafers were bonded with this photoresist layer. The photoresist was exposed, developed, and oxygen plasma-cleaned through the silicon mold wafer, leaving the gold seed uncovered. Next, a DC electroplating process with a current density of 50mA/cm^2 at room temperature was performed to fill the silicon mold with copper. The seed layer wafer was separated from the mold wafer by removing the photoresist bonding layer in an acetone bath that takes a total of two days. A final lapping step was performed to remove the excess copper on the top side. This process flow is summarized in Figure 3.1 below.
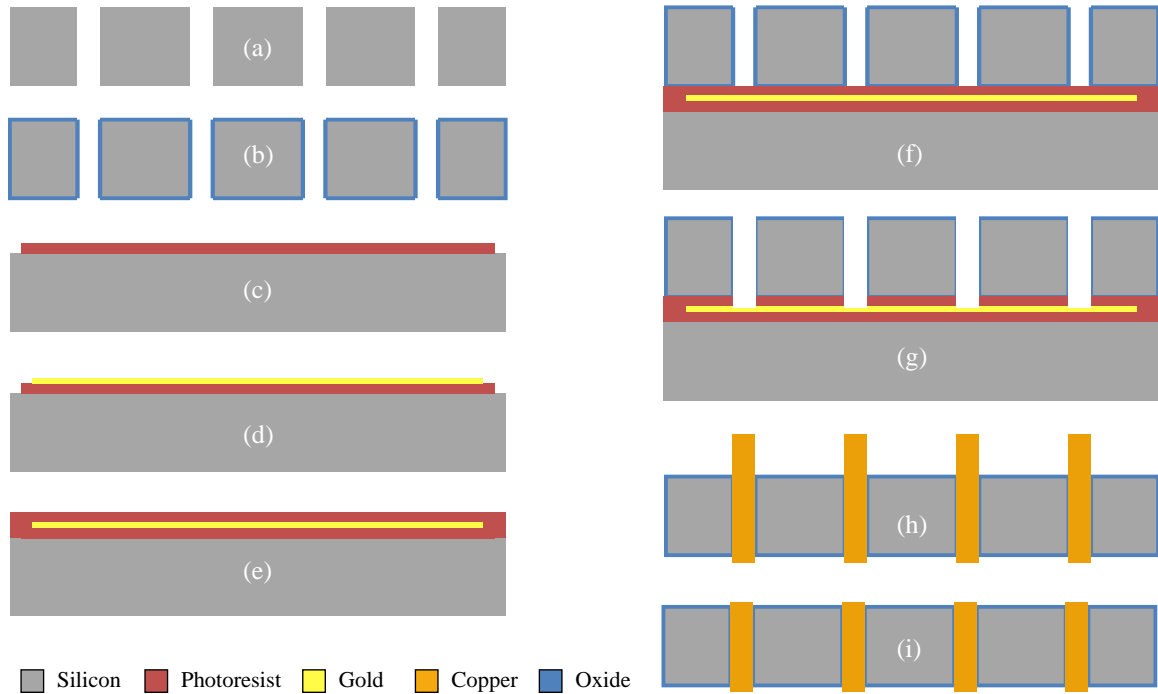
Figure 3.1. Fabrication technique for high aspect ratio copper structures. (a-b) Mold wafer DRIE and oxidation, (c-e) seed wafer preparation, (f-g) wafer bonding and lithography, (h) seed wafer detachment, and (i) mold wafer top-side lapping [138].

The top and bottom sides of the radial structures at the inner radius are shown in Figures 3.2 and 3.3, respectively. Due to the uneven plating profile resulting from simple DC plating, the top side of the wafer was over-plated to ensure all the etched patterns were filled. Figure 3.2 shows a scanning electron microscope (SEM) image of successfully plated patterns after the lapping process. The bottom side of the wafer does not require further processing due to the seed layer detachment step, which was the goal of this process development. A profile scan of these patterns is also presented in Figure 3.3b. The average height of the copper protrusions together with the gold seed was measured to be 2.3µm, which is on the order of the planarity achievable with conventional polishing techniques [138]. This plating process is not only

essential for the micro-turbo-generator fabrication presented in this dissertation, but it also enables the development of power MEMS devices with low-resistance connections and high electrical efficiency.
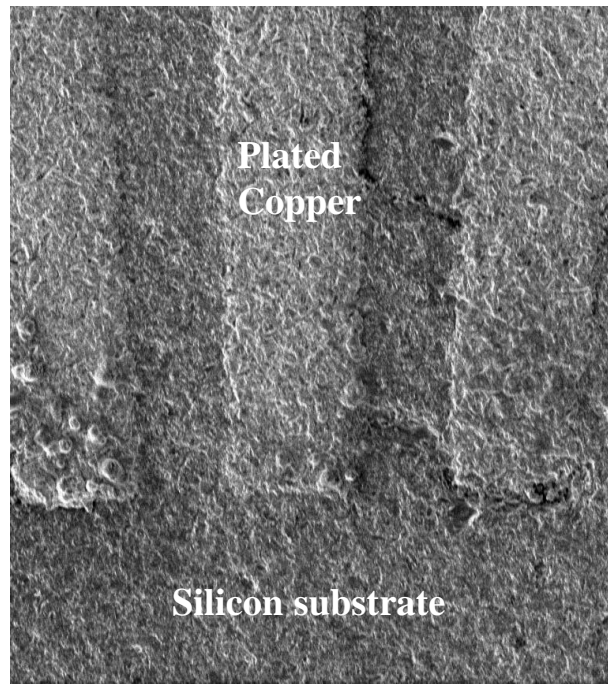
Figure 3.2. Top side of the mold wafer showing the void-free copper electroplated in silicon. The patterns were over-plated then lapped to ensure successful pattern-filling and planarization.

(a)   (b)
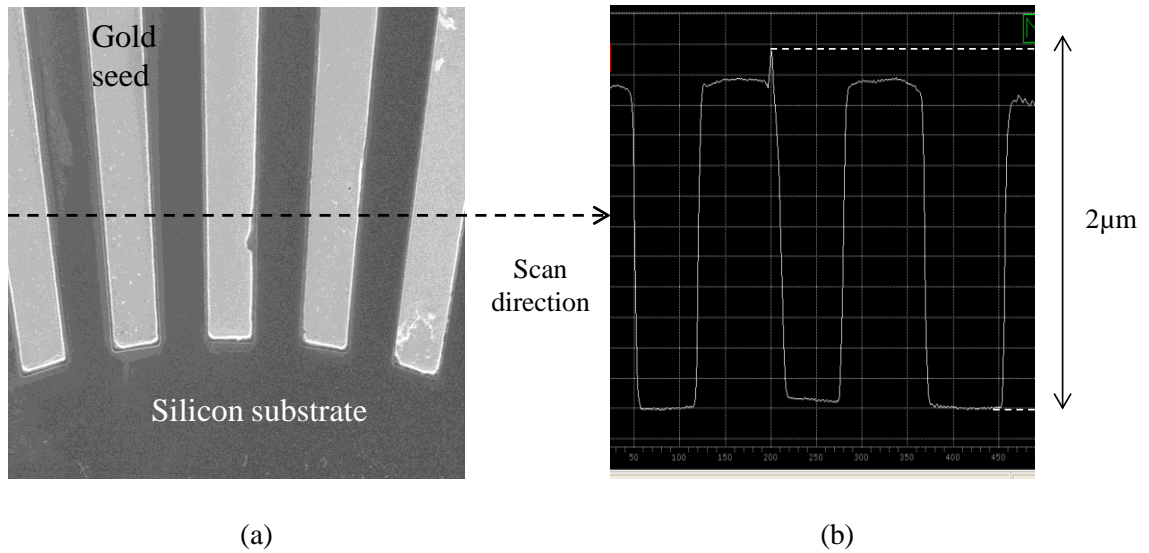
Figure 3.3. (a) Bottom side of the mold wafer showing the gold seed on the plated copper. The remaining gold seed between the plated structures was lifted off in the ultrasonic acetone bath, (b) profile scan of the bottom side in the direction shown in (a).

Next, the wafer was diced to inspect the copper film under the microscope. Figure 3.4 shows the side view of the successfully plated void-free copper in a silicon trench. The first order resistance calculation and the actual four probe measured resistance of the structures are 55mΩ and 71mΩ, respectively. The increase in practical values is due to the neglected geometry effects in the calculation and the slight mismatch between the dimensions of the designed and fabricated structures. These results show that the plated Cu in the trenches is of sufficient quality.

Copper →

Silicon ←

Dirt from
dicing saw →
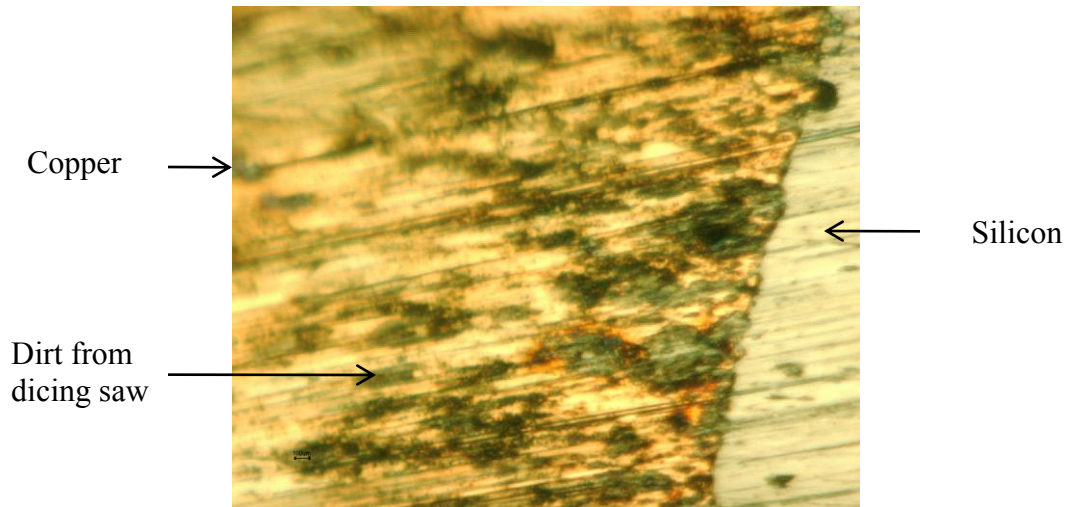
Figure 3.4 Side view of the copper. Residues on the plated copper are from the dicing saw.

Test structures later showed that increasing the temperature of the substrate to about 100°C, a temperature which was necessary for future processes, results in cracks and finally fracture of the silicon substrate, specifically between the sharp corners of silicon-copper interfaces (Figure 3.5). This was mainly due to the mismatch between the linear coefficients of thermal expansion of silicon (3×10^{-6}/°C) and copper (17×10^{-6}/°C). Since the pressure induced by copper expansion within the silicon is higher at these corners, the substrate starts breaking along the lines connecting them first. To resolve this issue and distribute the pressure more evenly, new test structures were designed and plated with rounded edges. Rising the temperature to 100°C proved that the silicon wafer can withstand the copper pressure at such temperatures and accordingly, the device coil design is slightly modified to possess rounded edges.
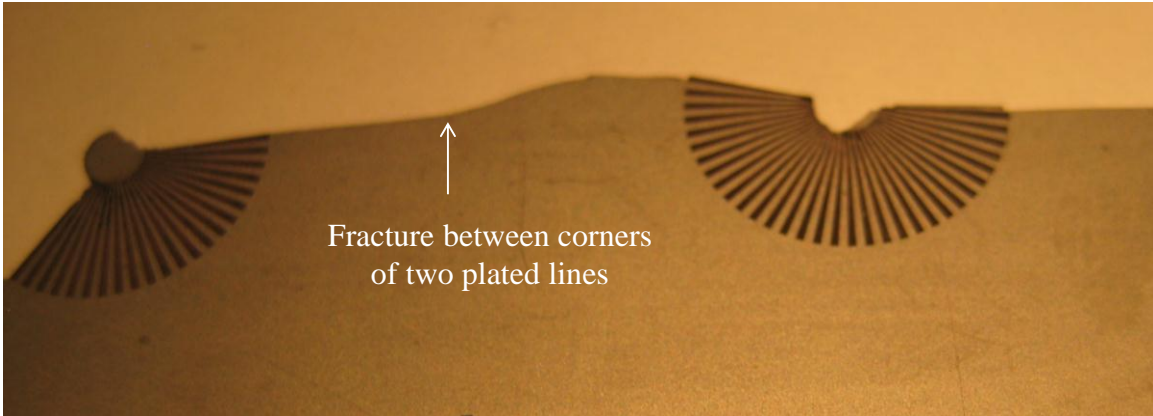
Figure 3.5. Fracture due to the coefficient of thermal expansion mismatch between copper and silicon.

3.1.2. Fabrication of Integrated Coil Structures

The bottom-up electroplating technique with the described seed wafer detachment method constitutes the back bone of silicon-integrated coil fabrication. The process flow shown in Figure 3.1 was followed to fabricate the coils, schematically illustrated in Figure 2.4a, with the only exceptions that 400µm-thick substrates were used and a copper seed layer was used instead of gold to wet etch the bottom side protrusions more easily. Removing these protrusions is especially important for dielectric material patterning process later in the fabrication.

A major problem that was encountered at this point in fabrication was the cracking of the copper-plated silicon wafer resulting from:

- the separation of wafer from lapping chuck by melting the wax holding the two together at 100ºC on hot plate

- the curvature of the wheel in lapping process

Fractures were mostly observed along the lines connecting the edges of plated coil lines similar to those shown in Figure 3.5. The resulting fractures despite the rounded coil design are attributed to the densely packed geometry along with longer coil design compared to the test structures used in preliminary process development. Accordingly, the applied 100ºC temperature to melt the wax and break the wax bond between the silicon wafer and lapping chuck is thought to induce enough stress between the copper and silicon. A study conducted by Hu showed the fracture strength of silicon with damaged surfaces can decrease down to 0.3GPa [139], supporting this argument further. Therefore, an alternative process was developed to remove the silicon wafer from the chuck after lapping step. In this process, a solution made of Alconox soap and water was heated up to 70ºC and the chuck-wafer assembly was immersed in it. After an overnight immersion with occasional agitation, the wafer was successfully detached from the chuck.

In addition to high temperature, slight curvature of the lapping wheel produces adequate stress to break the silicon wafer. Although the normal force used in lapping process was decreased to mitigate this effect, no decrease in the fractures was observed. An alternative to this problem was to develop an AC electroplating process that would yield a smooth top surface, eliminating the need for a lapping step. Although several studies were conducted on AC electroplating, finding the right processing conditions such as AC pulse width, amplitude, solution pH, temperature, and stirring speed highly depend on the geometry of the structures to be plated. Since developing such an electroplating process that would work for every different device design would be a research topic on itself, it was left out of the scope of this work.

Therefore, the DC plating – lapping sequence was kept and the device fabrication was modified from wafer-level to chip-level to decrease the total area and hence the total stress throughout the lapped surface. However this change brought significant challenges to the microfabrication of this device. The main challenges of the chip-level fabrication are:

- increased misalignments in lithography steps

- necessity to develop new recipes

- equipment issues

Initially, the masks were designed for wafer-level processing with alignment marks at the two sides of the wafers shown in Figure 3.6. The geometry of these alignment marks was designed such that the maximum alignment tolerance at each layer would be less than 5μm.

Figure 3.6. Alignment marks with multiple levels of tolerance designed for wafer-level processing that would yield ~5μm maximum misalignment.

Chip-level fabrication requires dedicated alignment marks on each of the five different chips across the wafer, which were not built into the original design. The

patterns were instead roughly aligned during the lithography processes by looking at the features on the mask and patterns. This change in the processing made alignment challenging, specifically when using thick polymers in the fabrication.

In addition to misalignments arising from the absence of alignment marks, new recipes had to be developed for chip-level processing as conventional recipes had been developed for wafer-level fabrication. These recipes are explained below and also given in Appendix section for each process step performed. Finally, since most fabrication equipment is compatible with wafer-level processing, alternative ways to get around such challenges had to be created. However, resolving these problems significantly increased the time spent for the fabrication of the micro-turbo-generator. Due to all of these fabrication changes and challenges, the overall process was simplified as much as possible to decrease the total number of fabrication steps and demonstrate the first successful realization of the device.

To implement the chip-level processing in device fabrication, the wafers were diced after the DRIE step in Figure 3.1b, and the rest of the sequence was performed on single chips. A similar cleaving procedure was also applied to seed wafers. Pictures of stator chips after coil housing DRIE and electroplating processes are shown in Figures 3.7 and 3.8, respectively. The schematic of the stator after this process is as shown in Figure 3.1i, which roughly corresponds to the fabrication cross-section shown in Figure 3.8.
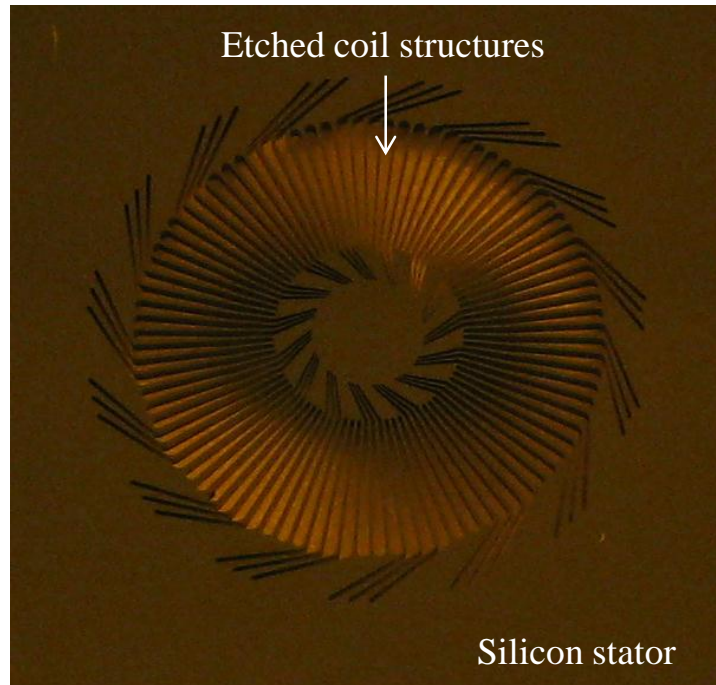
Figure 3.7. Picture of a silicon stator after DRIE of coil structures.
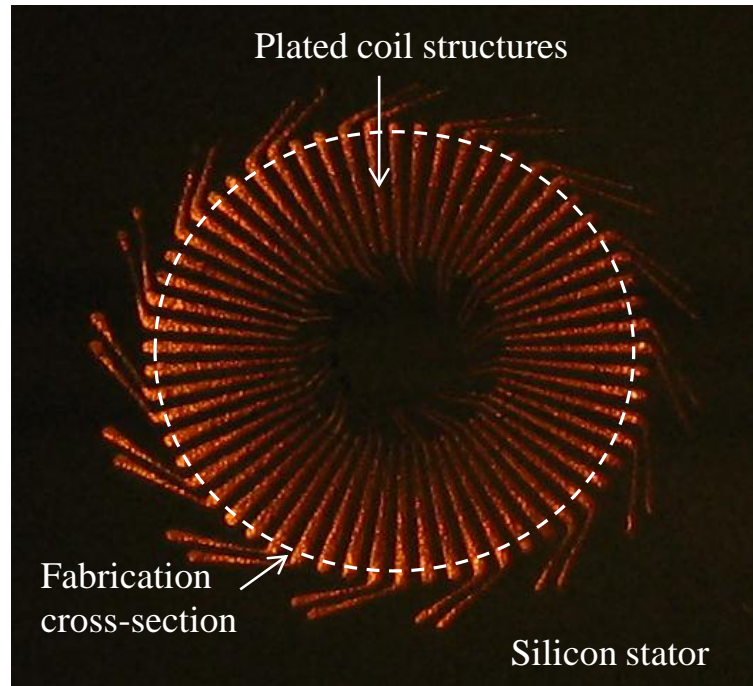
Figure 3.8. Picture of a silicon stator after electroplating of copper structures. The cross-section roughly corresponds to the wafer schematic in Figure 3.1i.

The next step in the original process flow was etching microball pits in the stator substrate for stator-rotor alignment and air gap definition in the final assembly. This alignment technique was first implemented by Waits in [8] to align different wafers of a rotor with encapsulated ball bearings. Similarly, etched pits in both the rotor and stator would result in perfect alignment of these two components with tolerances on the order of ~2µm with a controllable air gap. A schematic illustration of this technique is shown in Figure 3.9. Note that while a detailed stator schematic was provided, no features for the rotor are given in Figure 3.9 as these features will be described in the following subsections.
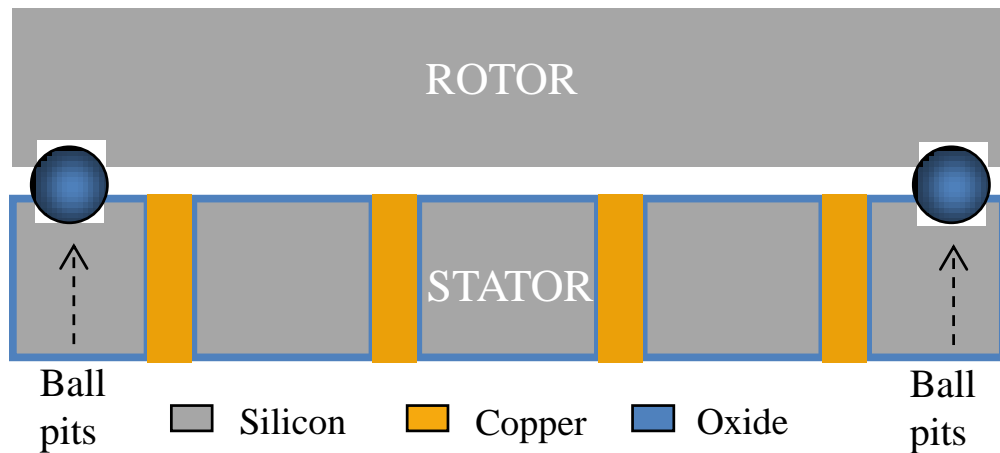
Figure 3.9. Ball alignment technique and ball pits etched in stator and rotor for alignment.

To perform DRIE technique and fabricate pits around the stator, AZ9260 photoresist was used to define the areas to be etched first. Due to fracture issues induced with increased temperature, the steps with heat treatment in the lithography recipe were modified. Accordingly, the normal soft baking procedure performed at 110ºC for 2-3 minutes was changed to a ramped heating from 65ºC to 90ºC for 30

minutes and a gradual cooling from 90ºC to room temperature. In addition, a number of in-house modifications including covering the wafer chuck with aluminum foil and putting extra chips on the chuck had to be developed in order to use the Quintel 4000 mask aligner originally designed for wafer-level processing. After finding the right conditions for a successful lithography given in the Appendix section, the chip was bonded to a carrier wafer for the subsequent DRIE step as the STS DRIE equipment was also designed for wafer-level processing. Finally, the stator chip was etched to create 200µm-deep alignment trenches in silicon. Many cracks were observed after the DRIE process, which were attributed to the heat generated on the chip during the etching step. Therefore, this step was eliminated from device fabrication, and the stator-rotor alignment along with air gap definition between the two was achieved through advancements in the testing package that will be described in Chapter 4.

The next step in fabrication process was the passivation of the top surface shown in Figure 3.8 using a benzocyclobutene (BCB) layer and opening up vias to deposit a metal seed layer for a possible second electroplating step on the stator backside. However, due to the difficulties encountered in the fabrication so far, this step was eliminated to simplify the process as it was not a crucial step for the realization of the device. Instead, the seed layer would be deposited on the whole top surface and etched later after the plating process. The need for the electrical passivation of the top surface was also eliminated by designing a test package that seals the stator top side, as described in Chapter 4.

3.1.3. Fabrication of Backside Coil Connections

The coil structures presented in Figures 2.4a and 3.8 have to be connected to realize three-phase multiple-turn continuous coils around the stator for an additive voltage induction. Since it is geometrically impossible to realize the complete coil scheme without self-crossing in one plane, the rest of the connections had to be realized in a separate layer, as described in the previous sections. Accordingly, a dielectric layer was used to passivate all stator backside with via openings only at the coil tips that should be connected together. The schematic of the wafer after the successful application of such a dielectric layer, following Figures 3.1i and 3.8, is shown in Figure 3.10.
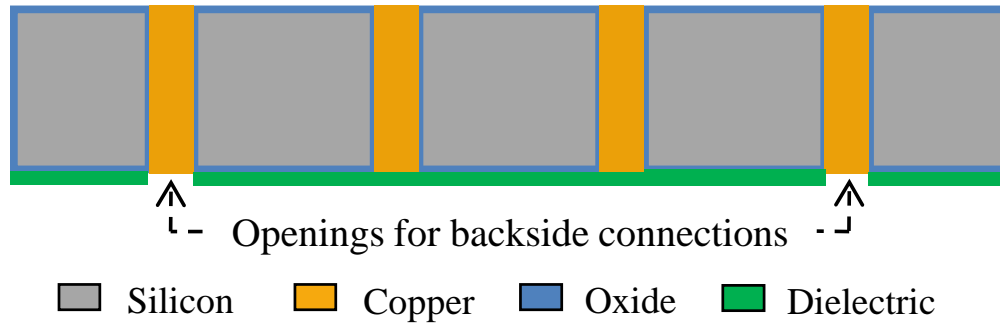
Figure 3.10. Schematic of the stator after patterning a dielectric layer on the backside for passivation and vias.

First, photo-patternable Benzocyclobutene (BCB) was used to create the dielectric layer shown in Figure 3.10. BCB had been used in other previously developed ball-bearing supported devices fabricated by our group [100-117] with a well-established processing recipe. Its chemical inertness along with the capability of UV-patterning makes BCB a good candidate for the dielectric layer. One drawback,

however, is the soft curing step at 220ºC which is part of the process that would lead to stator fracture. As this thermal treatment is not an integral part of the BCB lithography and is only performed to improve the polymerization and chemical inertness of the BCB film, the process was applied on test stator chips first without the final soft curing step. A 3µm BCB layer was successfully deposited and patterned using the previously developed recipes through a rough alignment between the stators and the optical mask performed by eye,.

The metal deposition and patterning step that comes after dielectric layer patterning involves the removal of a photoresist layer using acetone, which is an aggressive solvent. Hence, the dielectric used in the fabrication has to be chemically resistant to acetone and remain its structure after this treatment. In addition, the later fabrication steps also include plating through vias and accordingly, the dielectric layer is expected to withstand the chemical conditions imposed by electroplating. It was observed that BCB that did not experience a soft curing process was severely attacked by acetone which resulted in the cracking of the deposited metal layer. Therefore, BCB had to be replaced with another photo-patternable polymer. The already-designed and manufactured optical mask with clear-field features constrained the lithographic properties of this polymer to a negative resist.

Another negative photoresist that has a well-established process, and is frequently-used in MEMS is SU8. Availability of this product in various viscosities that allows for film thicknesses between 1µm - >200µm along with the durability in acetone makes it another candidate for a dielectric layer. Accordingly, SU8 was the second material of choice after BCB in the stator fabrication. Specifically, SU8-5 has

been selected to form a thin (3µm) dielectric layer with vias that could facilitate a good connection between the through-plated copper structures and to-be deposited back-side connection layer. After successful gold sputtering and patterning to form the connections on top of SU8-5 film, a copper seed layer was deposited on the top side of the stator for a second electroplating on the bottom side. This process was mainly performed to ensure a good and low-resistance electrical contact between the plated copper and deposited connections. The photographs of the bottom side of stators after electroplating process is shown in Figure 3.11 below:
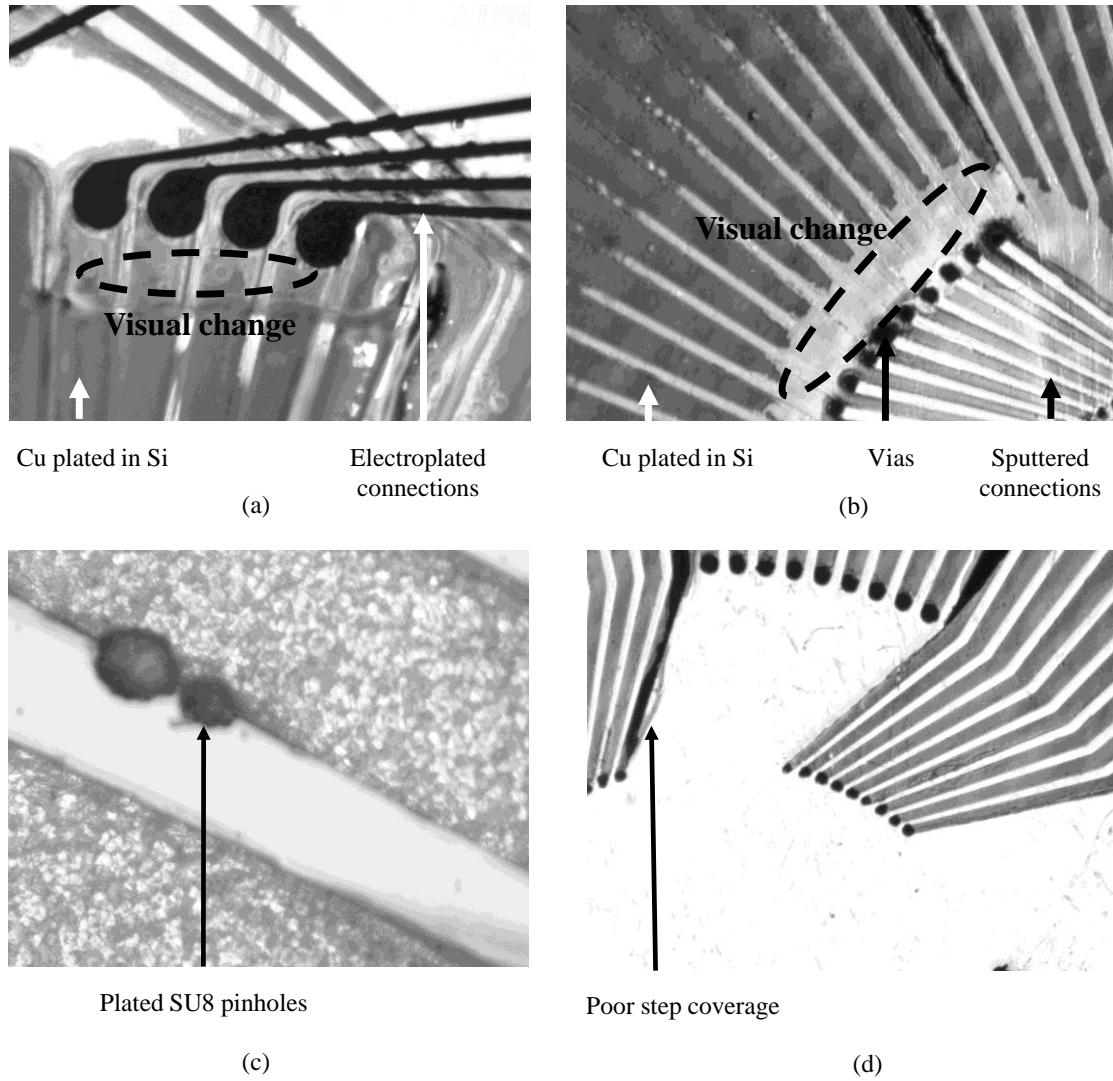
Figure 3.11. Photographs of stator backside after electroplating showing irregularities with (a-b) structural film changes, (c) pinholes, and (d) poor step coverage.

Electrical connections after the plating process showed that all the previously through-plated copper coils were short-circuited together. This was attributed to the same reason causing the visual change of the film shown in Figure 3.11a-b. In addition, pin holes and poor step coverage were observed in the SU8 film which also contributed to short circuiting through electroplating (Figure 3.11c-d). Increasing the

film thickness to 20µm by using a thicker SU8-50 resulted in the same problems shown in Figure 3.11. To observe the problem better, a set of tests was designed involving electroplating through SU8 on simple silicon chips with a copper seed layer and various via openings. For this test, copper was sputtered on a silicon wafer. Next, the wafer was diced and SU8 lithography was performed on individual silicon chips. Finally, these chips were electroplated and SEM pictures of these chips were taken. Figure 3.12 below shows a photograph and an SEM image of a chip with copper electroplating through SU8 vias.
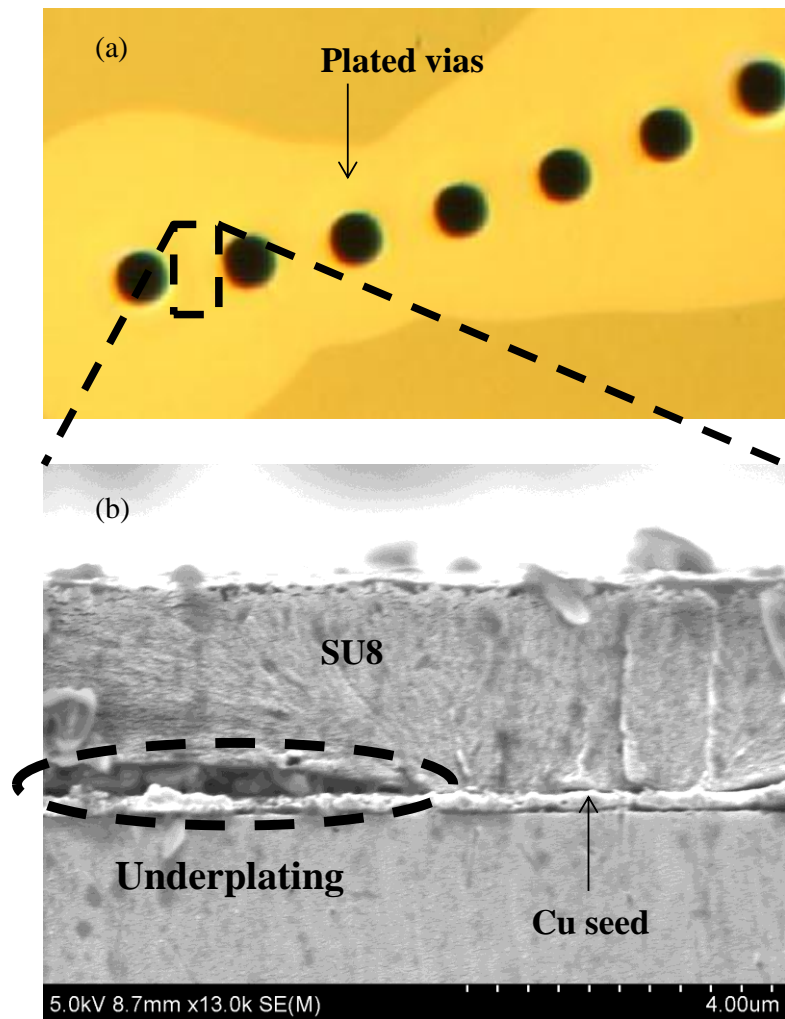
Figure 3.12. (a) Photograph and (b) SEM of plated vias in SU8 showing under plating.

The SEM imaging revealed that the plating also occurs at undesired locations between the vias independent of their sizes, which results in shorting the phases. This is thought to be a result of poor adhesion strength of SU8 in plating conditions. Consequently, SU8 is not suitable for use as a dielectric layer on the stator for the backside connection plating.

Finally, KMPR, which is a relatively new negative photoresist specifically developed for electroplating applications, was used for the fabrication of the dielectric layer in an attempt to solve the delamination issues previously reported. This photoresist is resistant to acetone and can be deposited at thicknesses between 4µm-120µm in a single spin coat process. The low viscosity KMPR1005 formulation was used to obtain a 6µm-thick film for shallow vias. Due to the previously discussed thermal issues, a new recipe had to be developed to safely perform the entire lithography process and define via openings.

KMPR lithography involves two heating treatments to the substrate: namely soft baking and post exposure baking at 100ºC for 5-10 minutes. To lower the risk of fractures, the substrate was gradually heated up to 100ºC. After a number of lithography tests, optimum conditions were found to be ramping the temperature from 65ºC to 100ºC on hotplate for a duration of fifteen minutes. Next, similar plating tests performed on SU8 were followed and SEM images of a sample chip that had different via sizes on it were taken. These images are shown in Figure 3.13 below.
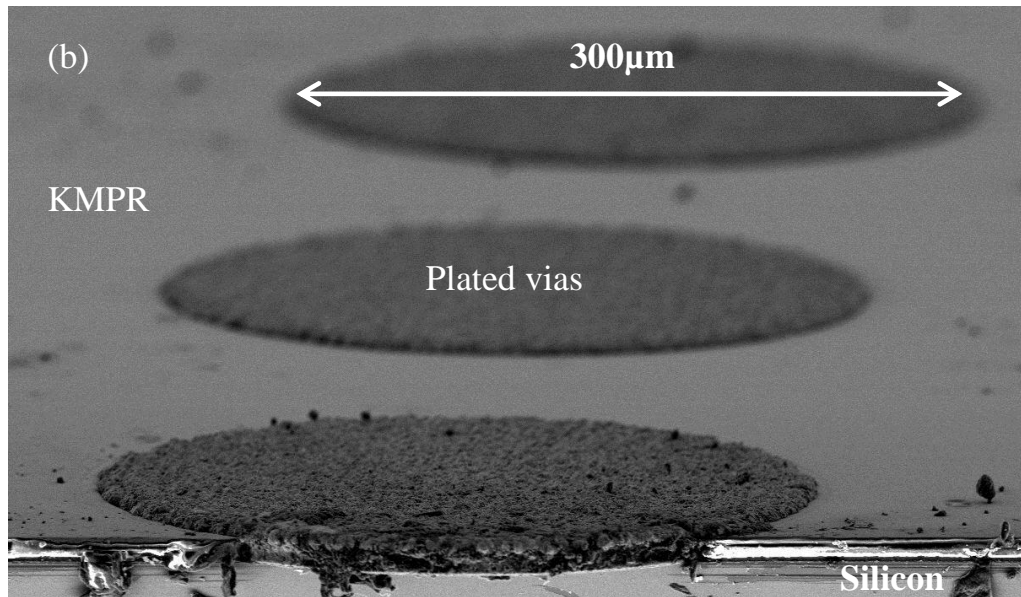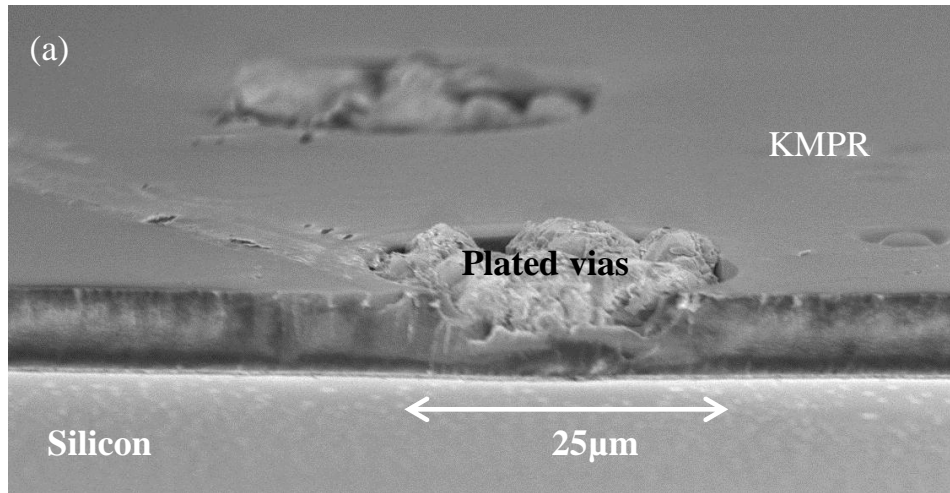
Figure 3.13. SEM of plated vias with (a) 25µm diameter and (b) 300µm diameter with no under plating.

As it is clear from these pictures, no under plating was observed regardless of the size of vias. Therefore, this developed process was applied to a stator with through-plated copper coils and the vias were plated. However, pinhole plating and poor step coverage issues were still observed that are similar to problems observed in

SU8 shown in Figure 3.11c-d. This was attributed to the low thickness of the KMPR film, and accordingly a more viscous KMPR1050 film was used next to increase the film thickness.

The increased thickness and viscosity of new KMPR1050 film mandates a separate optimization on lithography conditions. Therefore, similar procedures followed for SU8 and KMPR1005 were repeated to figure out optimum parameters that leads to a fracture-free substrate with well-defined 20μm-deep KMPR vias. While the gradual temperature increase from 65ºC to 100ºC was kept for both soft baking and post exposure bake steps, a total baking time of half hour resulted in a good-quality lithography process. One major problem with the lithography, however, was the very thick edge beads around the substrate that caused problems in the mask aligner in addition to the increased the mask-to-substrate gap during exposure. Due to the same reason, the features on the mask and the test substrate were not visible at the same time. By adding extra thick silicon pieces around the substrate chip, the lithography could be performed successfully. However as a direct result of the large air gap between the optical mask and the substrate, the features suffered from misalignment as well as size shrinkage due to light leakage which resulted in the exposure of undesired areas. Although the features were not perfectly transferred to the test substrate, the lithography was successfully completed. Next, the same plating tests were repeated and promising results similar to that shown in Figure 3.13 were obtained. Proving the robustness of KMPR1050 as a dielectric layer, the same process was applied to the backsides of stator chips with through-plated copper coils.

After successful KMPR lithography, the via openings were measured to have a depth of 20μm, showing that the topography of the stator did not have any effect on film thickness. Next, the vias were plated to bring the copper surface up to the KMPR level that will help the electrical connection between the to-be deposited gold layer and the plated structures. A copper seed deposited on the top side was used as a seed layer and the features were plated at a current density of 50mA/cm^2. Subsequently, this layer was etched in a wet etching solution while a protective photoresist layer was deposited on the back side to cover the plated vias. Finally, a 200nm thick gold layer was sputtered and patterned using AZ9260 photoresist. The recipes of lithography processes are provided in the Appendix section. During gold patterning by wet etching of exposed areas, the top side of coils was protected using a separate photoresist layer which was later removed in acetone. The schematic of the stator substrate after this step that follows Figure 3.10 is shown in Figure 3.14.

■ Silicon ■ Copper ■ Oxide ■ KMPR1050 ■ Gold
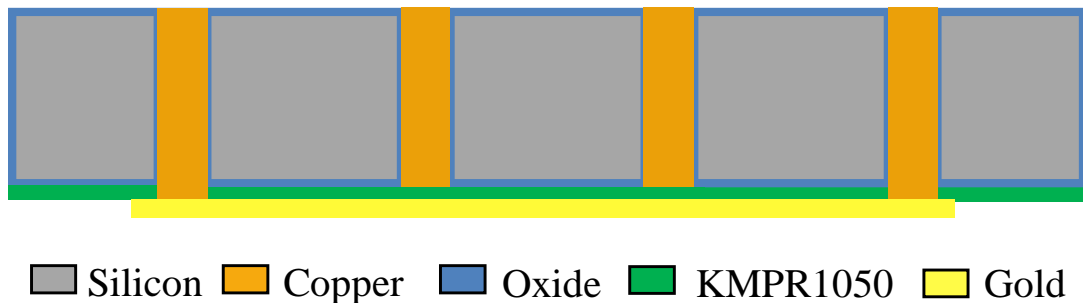
Figure 3.14. Schematic of the stator after the deposition and patterning of backside connections.

A second stator without plated vias was also fabricated with well-connected coils. Further plating the backside connections in a separate KMPR1050 mold with

the same backside connection pattern on this stator was performed to decrease the total resistance. However, due to the increased material complexity and geometry along with increased misalignments, this final plating process resulted in complete shorting of the different phases. Accordingly, this optional step to decrease the resistance was removed from the fabrication process for the first successful device realization. Since the resistance is dominantly determined by the thin backside connections in such a structure, there is no need to completely fill the coil housings in the first electroplating process as the contribution of complete-filling in decreasing the resistance would be negligible. Therefore, the through-hole electroplating was stopped when the copper reached the top stator surface at the relatively wider outer ends of the housings to remove the lapping process and further simplify the fabrication. The housings were observed to be half full with 200μm copper at the inner parts. The final stator process flow is shown in Figure 3.33 at the end of this chapter.

3.2. Rotor Fabrication

The rotor component of the micro-turbo-generator illustrated in Figure 2.5 is based on a microturbine design previously demonstrated by our group in a micro-turbo-pump platform as reported in [8]. While the general structure is similar, significant aspects of the design were changed to incorporate a permendur disc and pie-shaped discrete NdFeB permanent magnets into the spinning rotor.

The rotor component is a stack of two silicon wafers bonded together using a eutectic metal AuSn (74%-26%). To integrate the magnetic materials into the rotor

87

volume, a large cavity was needed in the center of the rotor. Since the permanent magnets are brittle and can break at high rotational speeds, at least half of the magnet thickness (250μm) along with the full permendur disc thickness (250μm), which makes the whole magnetic assembly as thick as one silicon wafer, was required to be embedded in the rotor. Accordingly, the two rotor wafers had to be bonded around the periphery of this magnetic assembly. The additional area required for bonding needs to be minimized to decrease the total radius of the rotor. Since no study on the characterization of the vertical strength of eutectic bonding has been reported, the minimum bonding area that can support the complete assembly was experimentally determined.

For this test, disc-shaped 1μm-thick eutectic metal with 5.1mm inner radius (slightly larger than magnet outer radius) and varying outer radii with a total width of w (r_{out}-r_{in} = w) were deposited on silicon substrates. Due to the use of a shadow mask in the deposition process, ~10º angle from two sides of the disc did not experience metal deposition. Substrates with the same bonding widths were bonded together using EVG 501 bonder at 330ºC and 3000N normal force. T-shaped aluminum fixtures were machined and glued to opposite sides of the bonded chips with epoxy. Finally, the assembly was separated by applying force in opposite directions using MTS 810 hydraulic universal testing machine to test the bond strength of eutectic metal for different values of w. A schematic illustration of the setup and a picture of un-bonded chips after testing are shown in Figures 3.15 and 3.16, respectively.
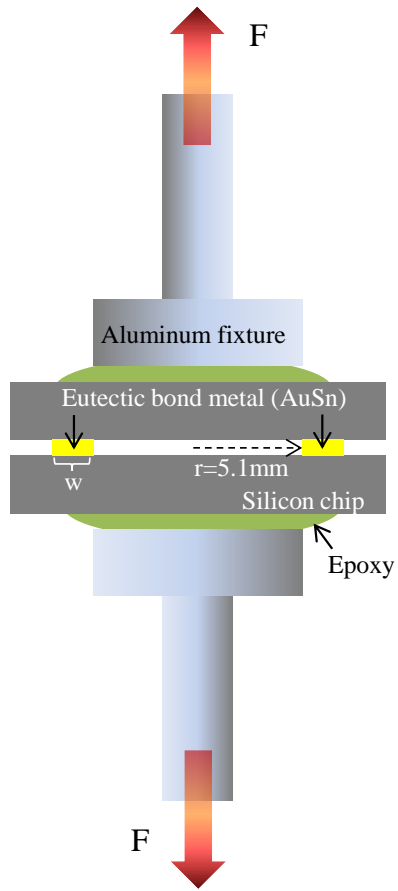
Figure 3.15. Test setup for characterizing the bond strength of AuSn.
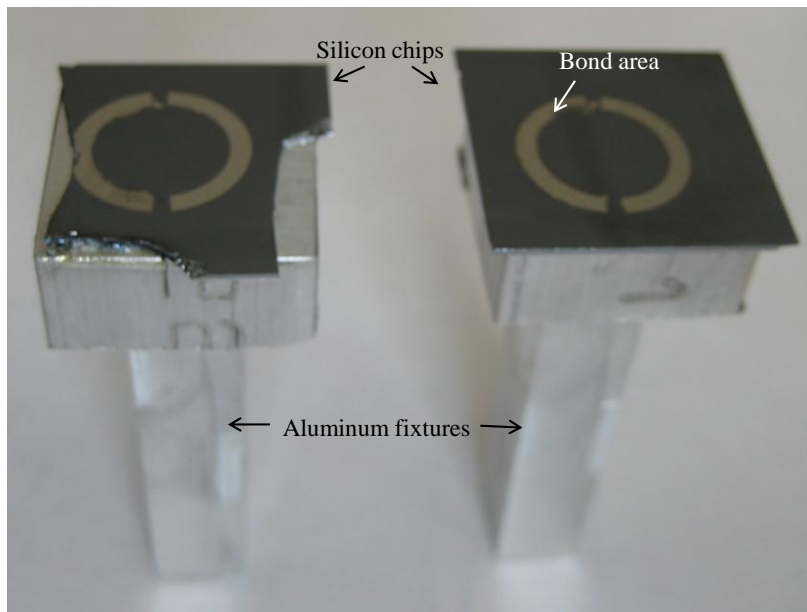
Figure 3.16. Picture of un-bonded chips and fixtures after testing.

The widths of 100µm, 250µm, 500µm, 1mm, 1.5mm, and 2mm were tested. It was difficult to extract quantitative data due to the limitations of the test setup that resulted in the deviation of the direction of applied force from perfectly vertical. However, the widths of 500µm and higher consistently un-bonded at forces greater than 5N, which is adequate to support the rotor assembly. Therefore, the width of the bonding area was determined to be 500µm. An additional 400µm was added to the radius for alignment tolerance and fabrication of a well against metal melting and leakage into the raceway during bonding. With all these additions, the rotor radius was set to be 6mm and the optical masks to fabricate the rotor were designed accordingly.

Rotor substrates were selected to be 4 inch, p-type, <1-0-0>, 515-535µm-thick, 1-10Ωcm silicon wafers with low bow and <2µm variation in thickness. While the electrical properties of the substrates are not important and are determined by the availability from the vendors, low bow and thickness variation were crucial in achieving uniform turbine geometry with good mechanical stability. Initially, alignment and dicing marks were etched on both sides of the top and bottom wafers to make the mask alignment and dicing processes easier with less error. Next, a 3µm-thick silicon oxide layer was deposited on these wafers as a DRIE mask by using plasma-enhanced chemical vapor deposition (PECVD) at 200ºC. AZ9260 lithography was then performed on both sides of the wafers and the oxide layers were patterned using reactive ion etching (RIE). To protect the wafers against RF arching during later DRIE steps, a 100nm of oxide layer was deposited on the top side of the top wafer and the bottom side of the bottom wafer. The schematic of the wafers at this

point in fabrication are shown in Figure 3.17. The oxide patterns are not the same as different features were fabricated on each side.
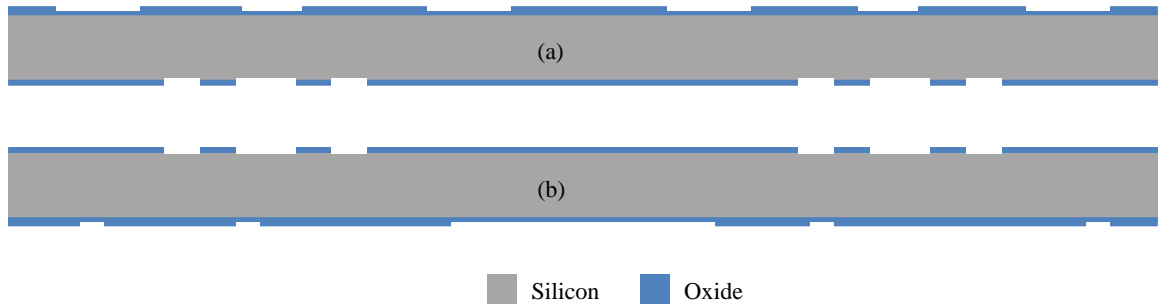
Figure 3.17. The schematic of (a) top wafer, and (b) bottom wafer after oxide deposition and patterning.

A two-step nested DRIE process is required to define asymmetric ball raceways (Figure 2.5a) and 145μm alignment ball pits and wells on the sides of the top and bottom wafers facing each other. Accordingly, AZ9260 lithography was performed on different parts of top and bottom wafers next, and the exposed areas were etched to have a depth of 50μm on each side (Figure 3.18).
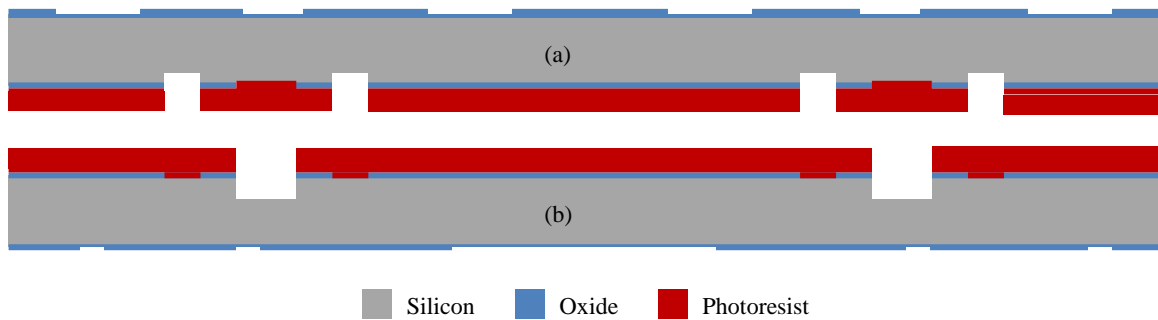
Figure 3.18. Photolithography and the first step of the nested DRIE to define the raceways, ball pits, and wells on (a) top wafer, and (b) bottom wafer.

The second part of the nested DRIE was performed after stripping the photoresist layer in Figure 3.18 and using the oxide mask only. While the top wafer was etched for 95μm, 145μm-deep DRIE was performed on the bottom wafer to create 145μm-deep ball alignment pits and wells on both wafers as well as a 95μm-deep ball raceway on top wafer and 195μm-deep ball raceway on the bottom wafer (Figure 3.19).
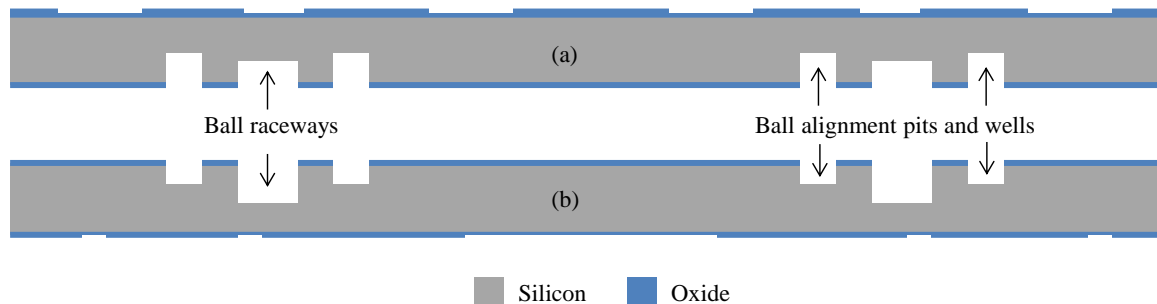
Figure 3.19. Second of the nested DRIE steps using oxide mask to define ball raceways, alignment pits, and wells on (a) top wafer, and (b) bottom wafer.

To make the releasing easier in later DRIE processes, a 30μm-wide area (journals) on the bottom of the raceways were etched for 200μm on the top wafer and 100μm on the bottom wafer. Both the location of these areas and the depths of the raceways are asymmetric to ensure that the microballs will ride on smooth silicon surfaces instead of sharp silicon edges (Figure 3.20).
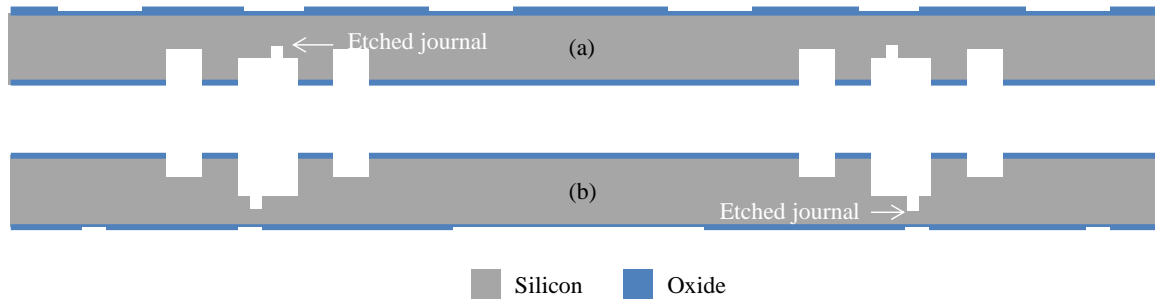
Figure 3.20. Journal etch on (a) top, and (b) bottom wafers.

Eutectic metal AuSn (74/26 wt. %) was then deposited on both wafers as a bonding layer. Since the surfaces of the two wafers already had deep topography, it would be difficult to pattern this layer using a lithography process. In addition, possible residues of lithography and patterning steps may lead to voids during bonding which can result in a bad-quality eutectic bond. Therefore, a shadow mask fabricated from a through-wafer DRIE etched silicon wafer was used as a masking layer during the deposition process. Separate microballs placed in etched pits on both the wafers and the shadow masks were used for alignment with a tolerance on the order of 10μm. Next, the top and bottom wafers were diced into individual rotor chips. This is specifically performed for a higher yield in bonding process as the rotors were bonded one at a time and possible problems during bonding would only affect one rotor assembly instead of a whole set. After successful dicing, around 100 microballs were placed in the ball raceway on one bottom wafer using tweezers, filling up roughly 80% of the raceway periphery. Four microballs on the etched alignment pits were also placed on the bottom wafer, and the two wafers were aligned. These wafers were then bonded at 330ºC and 3000N normal force using

EVG 501 bonder, which are the exact same conditions at which the bond testing had been performed. Figure 3.21 shows the schematic of the two wafers bonded together with microballs in between. The alignment balls are not shown to avoid any confusion and make the illustration simpler. It is once again noted the asymmetry in the locations of bond interface as well as the etched journals.
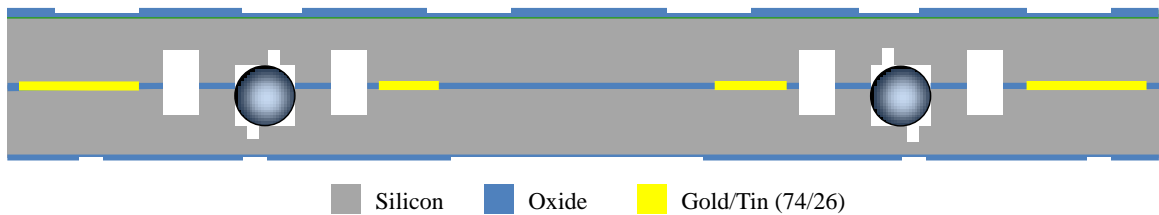
Figure 3.21. Schematic of the bonded wafers with microballs in between.

Another two-step DRIE is required on the bottom side to create 500μm-deep magnetic housing and perform a 200μm-deep etch to release the bottom side. Prior to the first DRIE, the protective oxide layer was etched using RIE, and a lithography with spray-coating process was performed on the bottom side of the wafer. Next, the rotor chip was bonded on a carrier wafer, and the DRIE was carried out. Figure 3.22 shows the schematic of the rotor assembly after these lithography and DRIE steps.
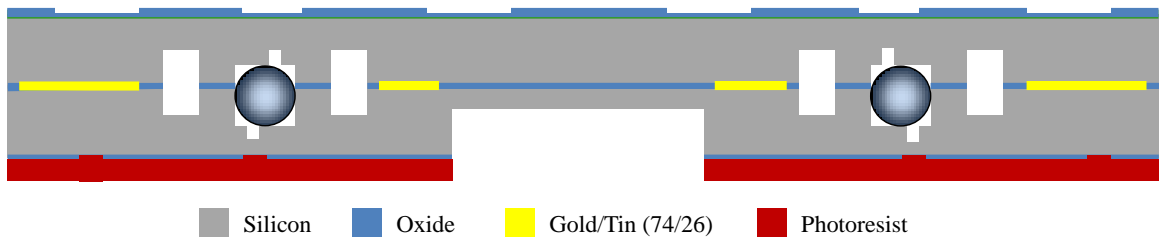
Figure 3.22. First DRIE on the bottom side that defines magnetic housing.

94

The second of the DRIE steps was not immediately performed on the bottom side. The rest of the processes applied on the rotor assembly aims to release the central rotational part from the outer frame, and therefore requires extra care. Considering the final geometry of the rotor, the bottom side is structurally weaker and more fragile compared to the top side. To prevent possible substrate fractures and bond failures, the turbine side was release-etched first. The schematic of the wafer after the top side release DRIE is shown in Figure 3.23. Prior to this process, the protective oxide layer was etched, the chip was bonded to a carrier wafer, and the pre-defined oxide layer was used as an etch mask.
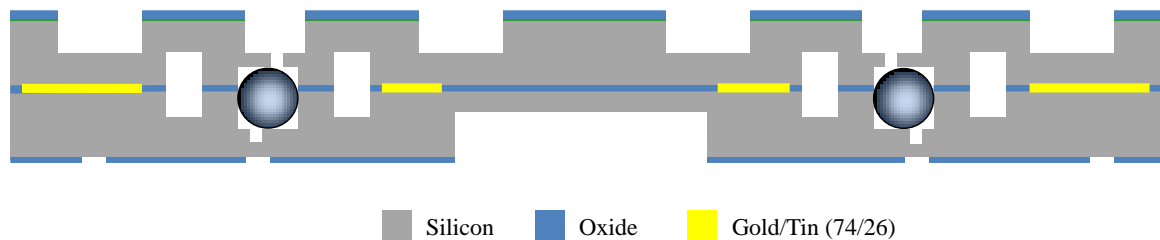
Figure 3.23. Schematic of the wafer after top-side release etch.

Although the top side was released first to improve the yield, an important number of rotor chips suffered from the failure of the eutectic bond after this step. Figure 3.24 shows the remaining of the rotor after un-bonding of the top side while Figure 3.25 shows separated top and bottom pieces of a rotor with a failed bond after the final release.
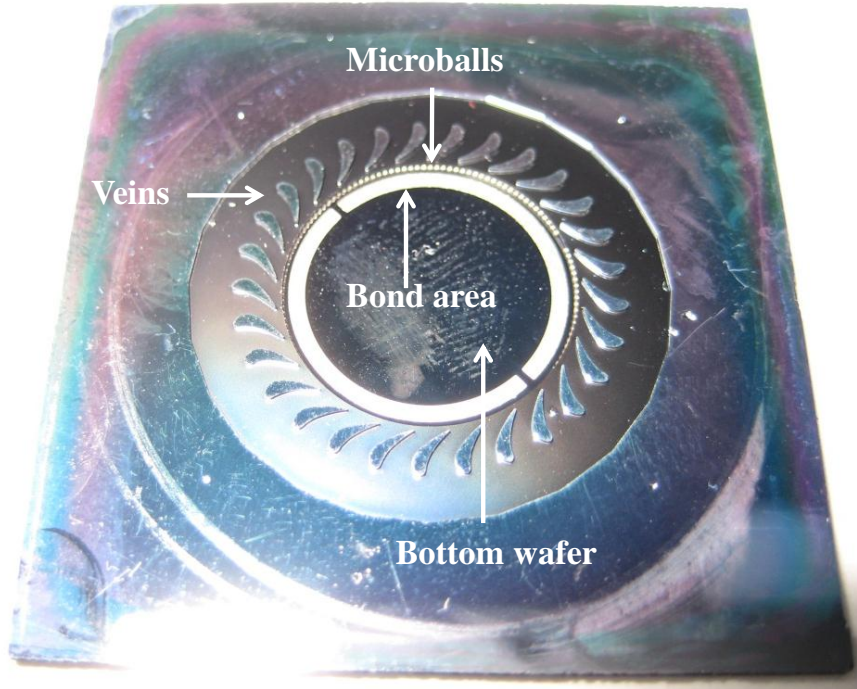
Figure 3.24. Picture of the rotor after top side was un-bonded, showing bond area, microballs,

vanes, and bottom wafer. Microballs are still in the trench and could not fall out.
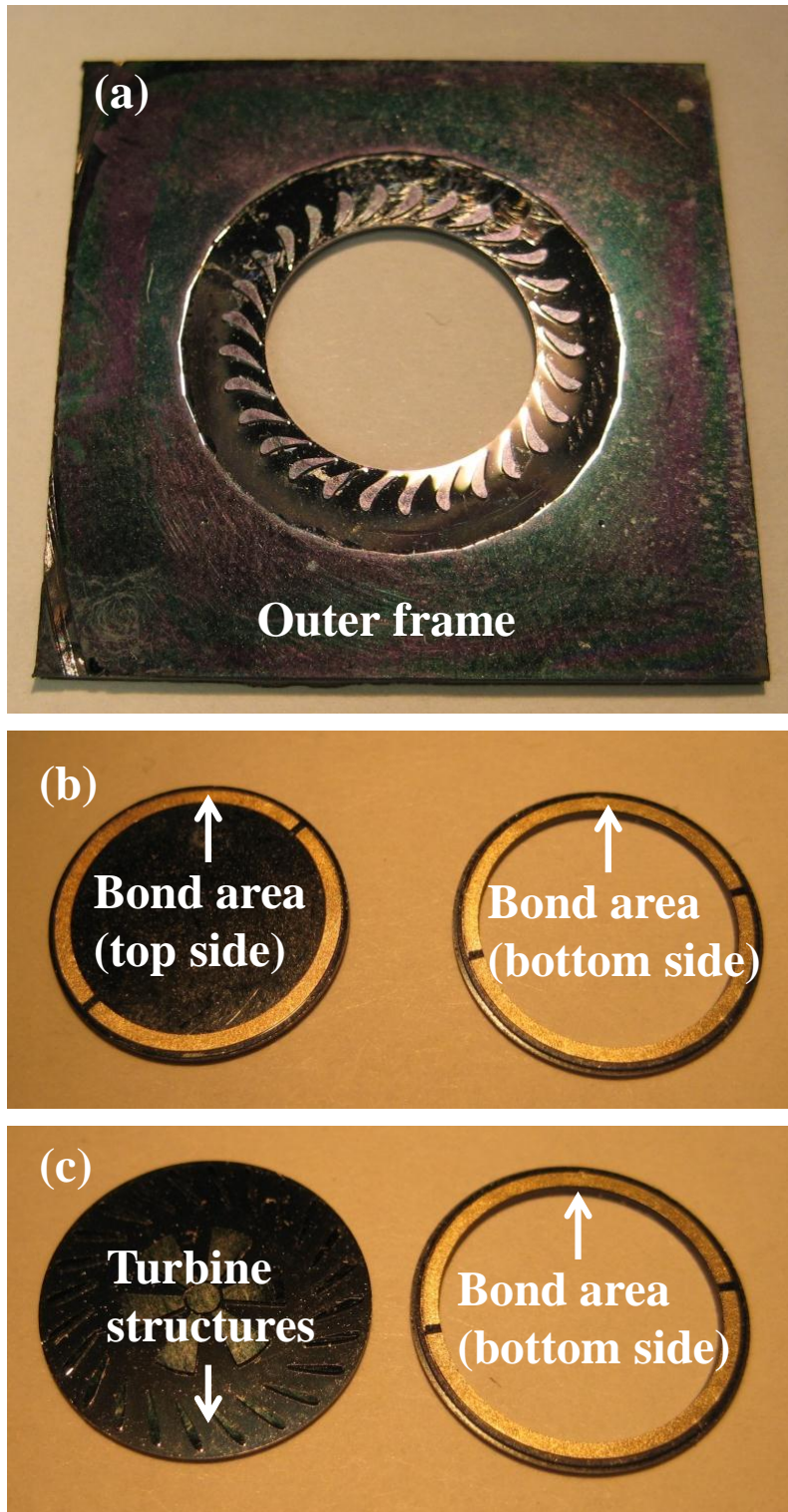
Figure 3.25. Pictures of (a) the outer frame after complete release, (b) bottom/top side of

top/bottom wafer, and (c) top sides of both wafers showing the bond areas and turbine

structures.

To address this problem, the bonding area was extended to cover the complete interface area between the two rotor wafers. The rotor of 10 pole 3 turns per pole device was fabricated following this solution by leaving a ~50µm-thick silicon area on the top side of the bottom wafer at the end of the fabrication that would hold the bonding area. However, significant number of rotors again suffered from the un-bonding of the two wafers. The failure of the rotor eutectic bond was attributed to random tooling problems such as material contamination and oxidation during the deposition, incorrect material composition deviating from 74/26 AuSn, and material oxidation during the bonding process. Some of the un-bonded top wafers were re-bonded in a furnace at 450ºC with 50g weight on top and the fabrication was continued. For the rest of the chips, the bonding was performed at slightly elevated temperatures and forces.

The rotors that survive the first release etch were bonded to carrier wafers and the final release DRIE was performed on the bottom side. The oxide layer on the silicon surface was used as a mask when etching the magnetic housing as well as the release area. Schematic of the rotor after this step is shown in Figure 3.26.
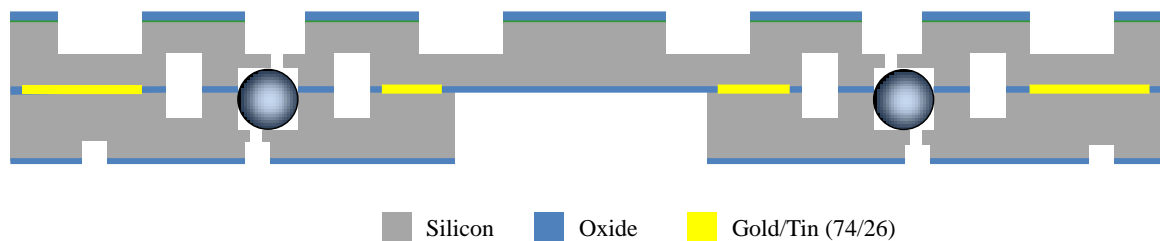
Figure 3.26. Schematic of the rotor after the final release DRIE step.

The final step in completing the rotor is the insertion of magnetic materials. While the outer radius of the magnets and permendur disc is 5mm, the housing etched in the rotor has a radius of 5.1mm to ensure a safe integration. Since the rotor is fragile at this stage, the magnets were assembled separately and the complete assembly was then incorporated in the rotor. Accordingly, a similar magnetic housing with the same dimensions was etched in a stack of two silicon wafers bonded together with photoresist. Next, the permendur disc was inserted in the housing and the pie-shaped permanent magnets, manufactured by Magnet Applications Inc, were inserted sequentially with alternating polarity. While the already-inserted magnet repels the next one in its proximity, there is a net attractive force between them through the permendur disc, helping the approaching magnet to be placed next to the previous one. This force eliminates the need for a special setup and enables manual assembly of permanent magnets using a simple pair of tweezers. The schematic illustration of the forces and magnet insertion are shown in Figure 3.27. Pictures of a single NdFeB permanent magnet and an assembly are shown in Figures 3.28 and 3.29, respectively. Permanent magnets were pre-coated with nickel by the vendor for corrosion resistance. Note that three of the ten magnets were intentionally not integrated for a more clear illustration.
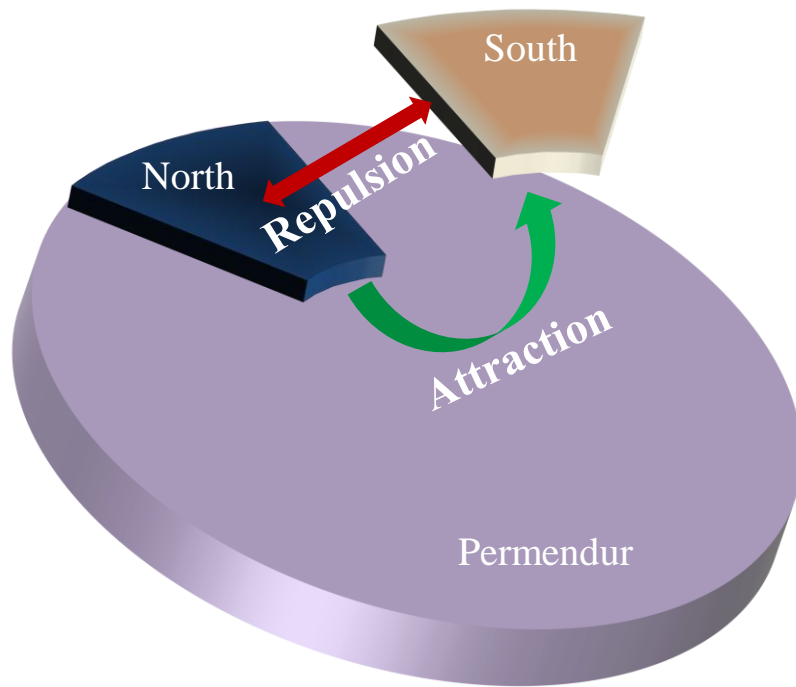
Figure 3.27. Illustration of magnet assembly process and the associated forces.

Figure 3.28. Picture of a NdFeB permanent magnet with Ni coating.
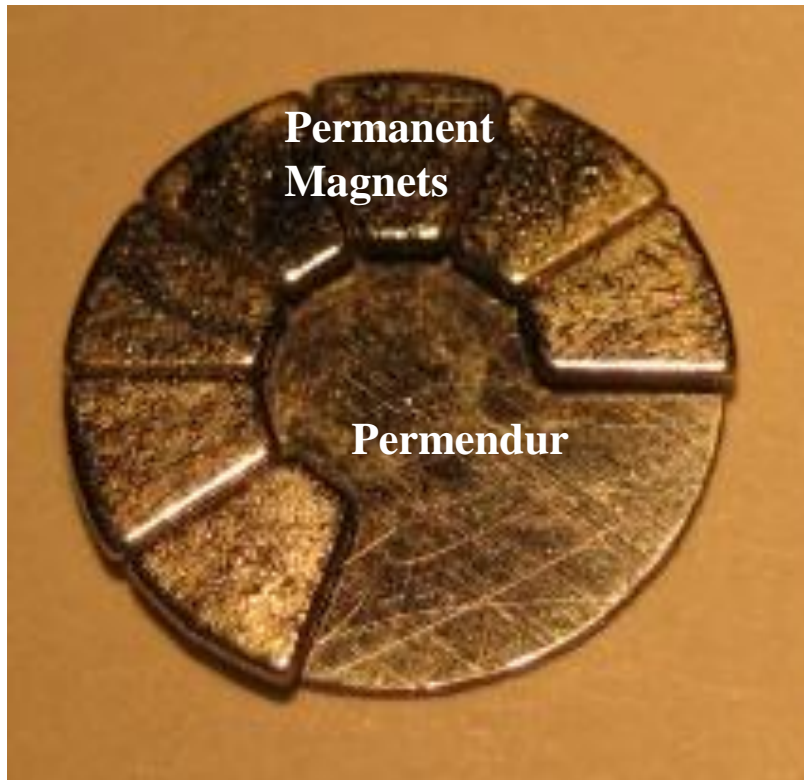
Figure 3.29. Picture of magnets assembled with alternating polarity on the permendur disc.

Three out of ten magnets were not inserted for a more clear illustration.

Once all the magnets were placed on the permendur disc, the complete assembly was taken out of the etched silicon housing and bonded to the rotor housing with epoxy. A manually applied normal force and a subsequent overnight curing at room temperature ensured a robust bond between the assembly and the rotor, completing the rotor fabrication. The final rotor schematic is shown in Figure 3.30. The successful fabrication and testing of the rotor was also presented in [140]. A summary of the rotor fabrication is shown in Figure 3.34.

Silicon   Oxide   Gold/Tin (74/26)   Permendur   NdFeB (North Pole)   NdFeB (South Pole)
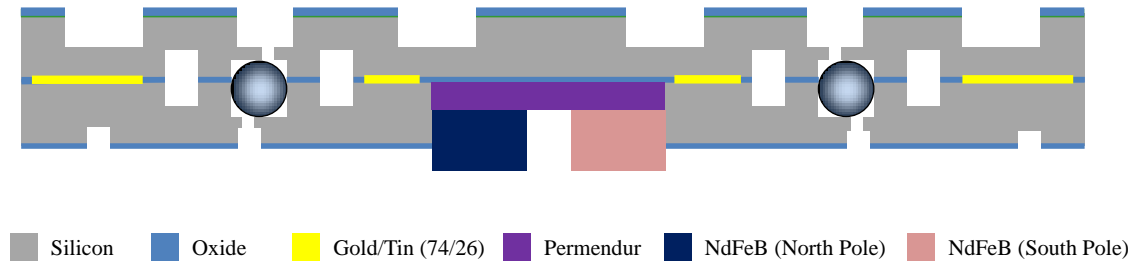
Figure 3.30. Schematic of the rotor after the integration of magnetic materials.

3.3. Plumbing Chip Fabrication

This final component of the micro-turbo-generator, shown schematically in Figure 2.6, is designed to direct the air flow through the device, and is structurally the same compared to the plumbing layer in the micro-turbo-pump presented in [8]. However, the larger device radius due to the reasons explained in the previous sections mandates the redesign of this component with a scaled-up geometry.

Silicon substrates chosen for the rotor were used for these chips mainly for their low bow and low thickness variation. Initially, the alignment and dicing marks were etched on the two sides of the wafer similar to the rotor fabrication. As the depth of this DRIE etch is on the order of 3μm, Shipley 1813 photoresist with 1.5μm thickness was used as an etch mask to improve mask-to-photoresist pattern transfer. The remaining plumbing chip fabrication was performed using two DRIE steps on the two sides of the substrate to create an etched recess and through holes in the center and around a circular path enclosing the micro-turbo-generator. The first DRIE step was performed to define a recess on the bottom side facing the rotor. During device operation, the plumbing chip is brought to contact with the rotor. To ensure that the rotor can spin freely when in contact with the plumbing chip, it's imperative to create

a space between the two directly over the turbine blades. Meanwhile, this space should not be too large in order to utilize the air momentum as much as possible. Accordingly, a ~50μm trench was etched with DRIE as a safety distance on the chip bottom side. Prior to performing DRIE, lithographically patterned AZ9260 was used as an etch mask. Figure 3.31 shows the schematic of the plumbing chip after the first DRIE step in fabrication.
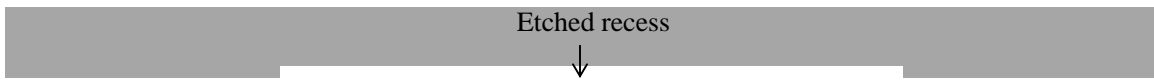
Figure 3.31. Schematic of the plumbing chip after the recess etch.

Successively patterning the recess on the bottom side of the wafer, a separate AZ9260 lithography was performed on the top side to define the peripheral holes that let the air in, and the central hole that guides the air out. Next, the wafer was attached to a carrier wafer. The second DRIE step was then applied and through-wafer holes were created in the plumbing chip. Finally, these chips were diced from the wafer using a dicing saw. The final schematic of the plumbing chip is shown in Figure 3.32 below. The complete fabrication of this component is also summarized in Figure 3.35.

Figure 3.32. Schematic of a complete plumbing chip.

3.4. Fabrication Summary

This section provides a schematic summary of the device fabrication. While 4 masks with 33 process steps were used to fabricate the stator, a total of 11 masks with 65 process steps and 3 masks with 12 process steps were utilized to fabricate the rotor and the plumbing chip, respectively. Figures 3.33-35 briefly shows these steps for the three different components. Pictures of a fabricated device are also shown in Figure 3.36.
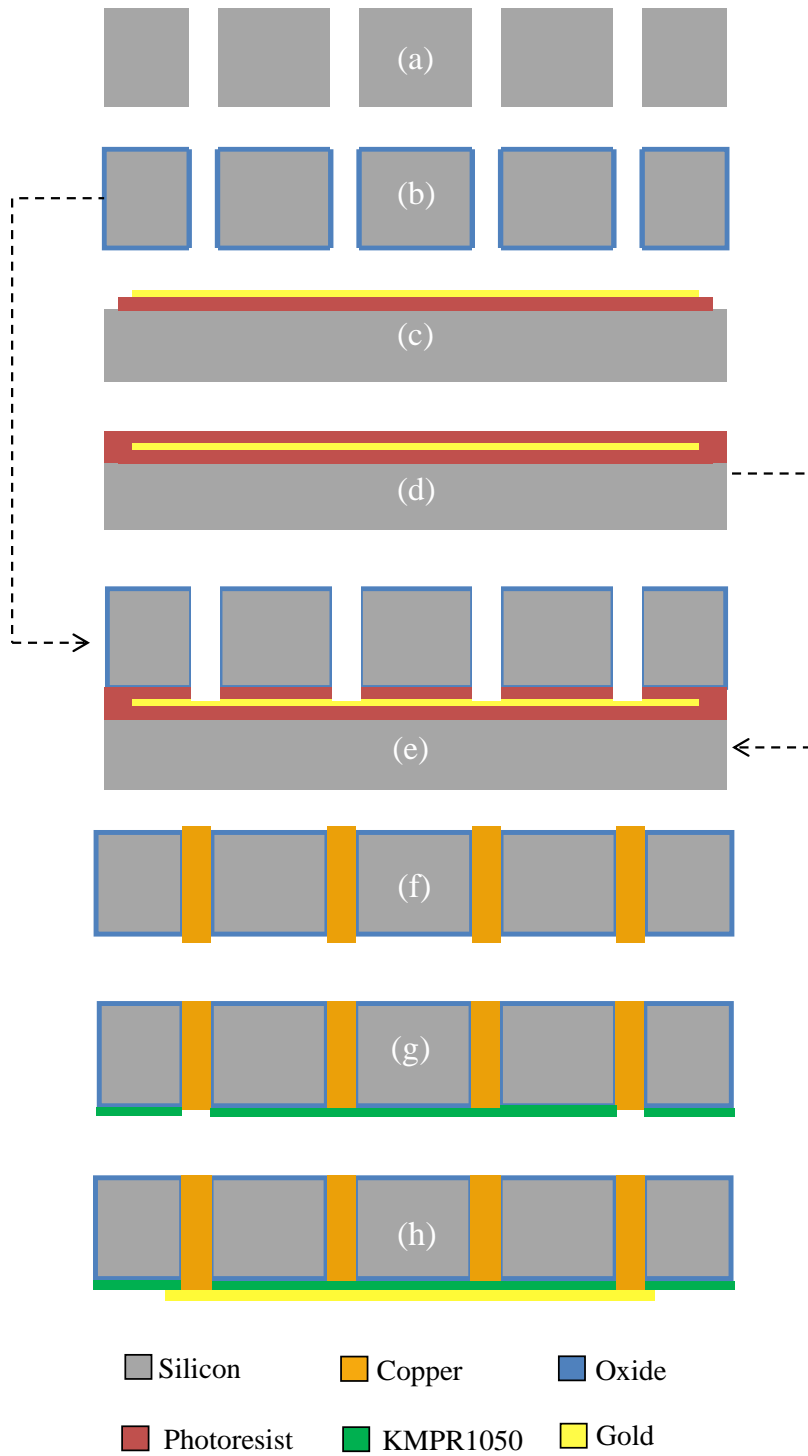
Figure 3.33. The fabrication flow of the stator, (a-b) DRIE and oxidation of coil housings in mold wafer, (c-d) seed wafer preparation, (e-f) electroplating and wafer detachment, (g) dielectric layer deposition, and (f) via plating and deposition of backside connections.

(a-top)

(a-bottom)

(b-top)

(b-bottom)

(c-top)

(c-bottom)

(d-top)

(d-bottom)

(e)

(f)

(g)

Silicon   Oxide   Gold/Tin (74/26)   Permendur   NdFeB (North Pole)   NdFeB (South Pole)
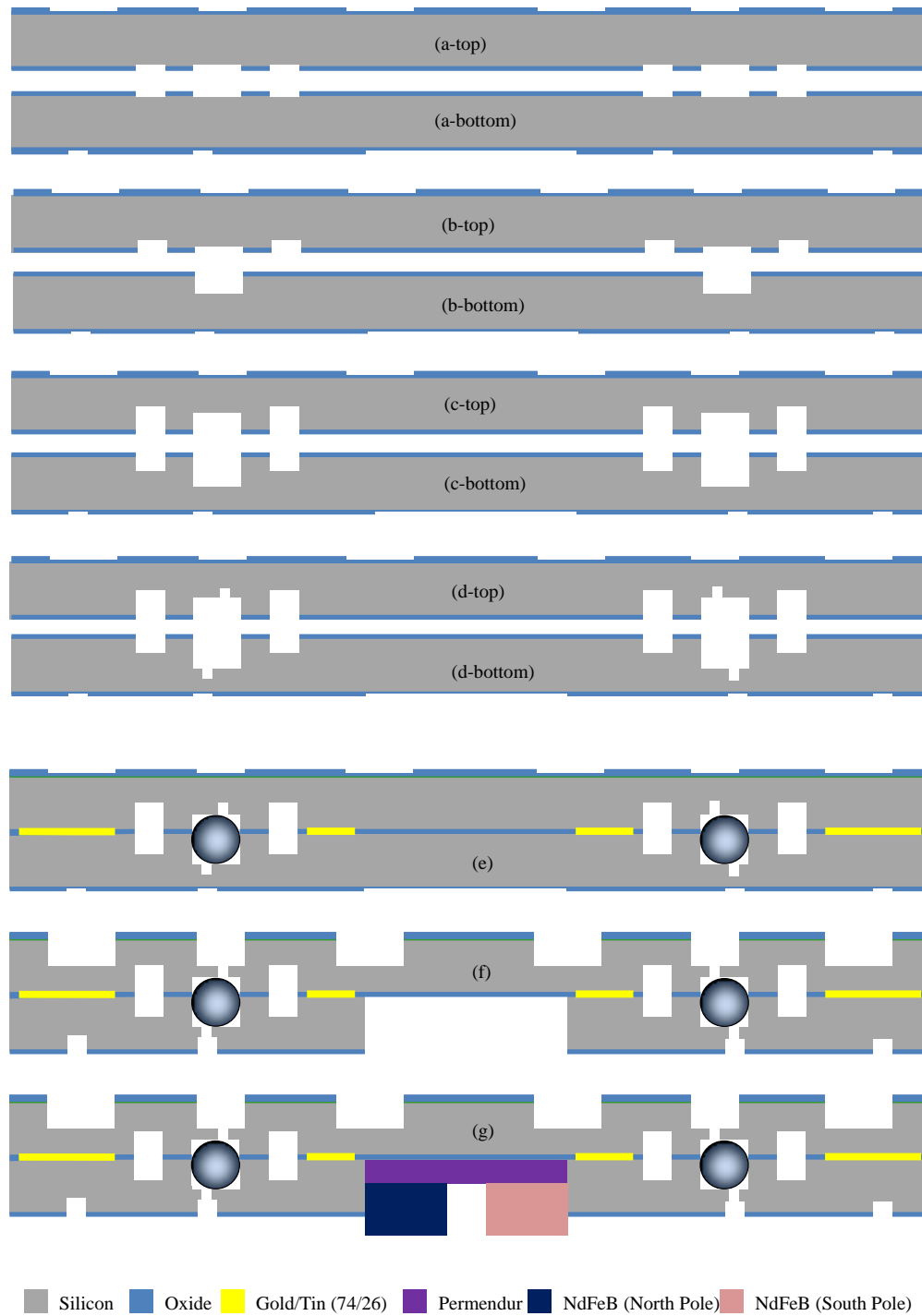
Figure 3.34. The fabrication flow of the rotor, (a-d) DRIE of ball raceways, journals, wells

and alignment pits, (e) wafer bonding with microballs, (f) magnetic housing and release

etches, and (g) bonding magnetic materials.

106
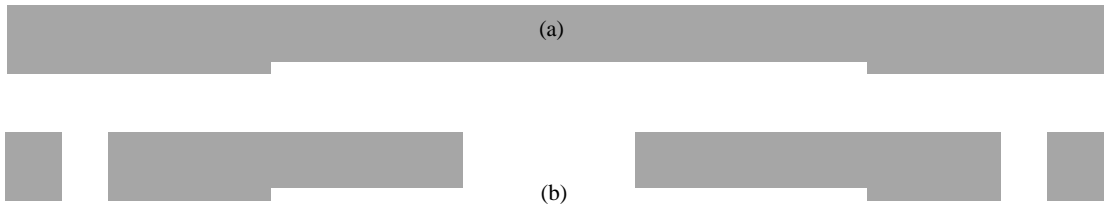
Figure 3.35. Fabrication of the plumbing chip, (a) DRIE of bottom recess, and (b) DRIE of through holes for gas flow.
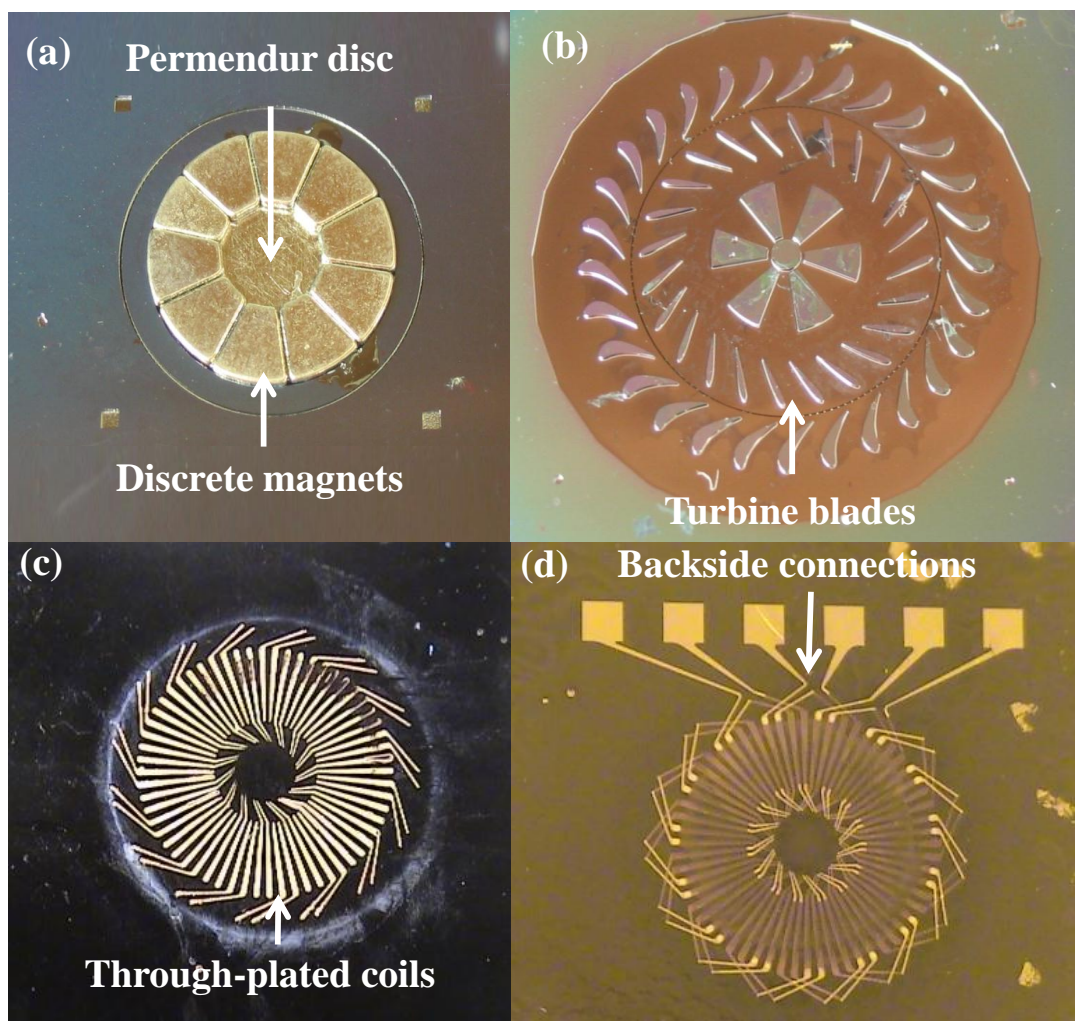
Figure 3.36. Pictures of a fabricated micro-turbo-generator, rotor (a) top and (b) bottom views, and stator (c) top and (d) bottom views.

4. Testing and Discussion

This chapter presents the characterization of the two successfully fabricated micro-turbo-generators with 10 poles 2 turns per pole and 10 poles 3 turns per pole, and their performance measurements. Prior to testing the device, a test setup and a plastic packaging were designed and built, allowing the device to be fully characterized. A systematic approach was taken for the tests where individual components of the micro-turbo-generator were tested first before measuring the complete device performance. Determining the electrical and mechanical parameters such as resistance, inductance, and friction torque for the stator and rotor, the device was tested for open circuit voltage and electrical power delivery. Experimental results are compared with the theoretical analysis and are discussed at the end of this chapter.

4.1. Plastic Packaging Design

Device packaging highly depends on the resting orientation and characterization strategy. To begin with, the electrical signals should be extracted in a convenient manner from the stator. Considering the fact that six electrical pads of the three phases on the stator were fabricated on the stator backside, it is easier to probe the phases if the stator backside is facing up. The alternative would be the backside facing any other orientation which mandates the use of a clamping mechanism for making robust electrical connections. Due to the already built-in copper stress in the stator, this could lead to fracture, and therefore was avoided. Once this was determined, the resting orientation of the device was determined to be stator on top of

the rotor with the turbine side facing down. The schematic illustration of this is shown in Figure 4.1.
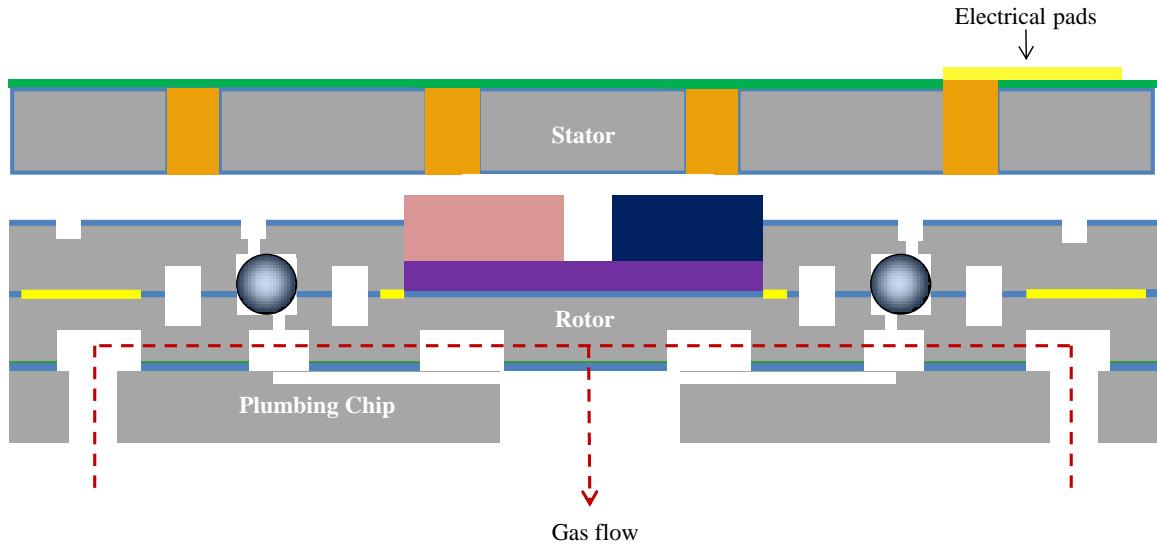
Figure 4.1. Upside-down testing orientation.

The horizontal asymmetry in the bearing raceway was designed such that the balls would roll on smooth silicon surface instead of sharp corners. From Figure 4.1, this is clearly the case when the rotor is at rest (or at very low speeds) due to the weight of the magnetic components and silicon rotor. During operation, the pressurized gas enters the turbine from the circular holes on the plumbing chip (shown as two side holes on Figure 4.1 and on Figure 2.6), passes through the veins and obtains a tangential angle, hits the turbine blades, and leaves the system from the center. When there is no sealing on the backside of the rotor at ambient pressure, the air flow results in a net pressure gradient across the rotor radius decreasing towards the center which leads to a net upward force. This, however, leads to the microballs to ride on sharp corners and hence excessive wear. To ensure operation on the smooth

side of the raceway, the pressure on the backside of the rotor has to be greater than the top side, leading to a net downward force. As the flow will also leak to the rotor backside towards the release areas in the ball raceway, the pressure on the rotor periphery will be equal to the backside pressure when the backside is sealed. The same pressure gradient across the radius, therefore, facilitates the pneumatic force in the desired downward direction. Consequently, the backside of the rotor has to be isolated and sealed from the top side, and from the ambient simultaneously.

The rotor-stator ball alignment pits that would define the air gap between the two could not be etched on the stator due to the previously discussed problems. Instead, small pieces of silicon wafers (spacers) were placed to create an air gap on the order of 100μm while the rotor-stator alignment was achieved through the initial packaging design that would yield ~100μm misalignment with negligible effect on the device performance. To incorporate the air gap spacers and backside sealing, the sealing had to be achieved without touching the rotor backside. Based on this restriction, the first generation packaging shown in Figure 4.2 was designed.
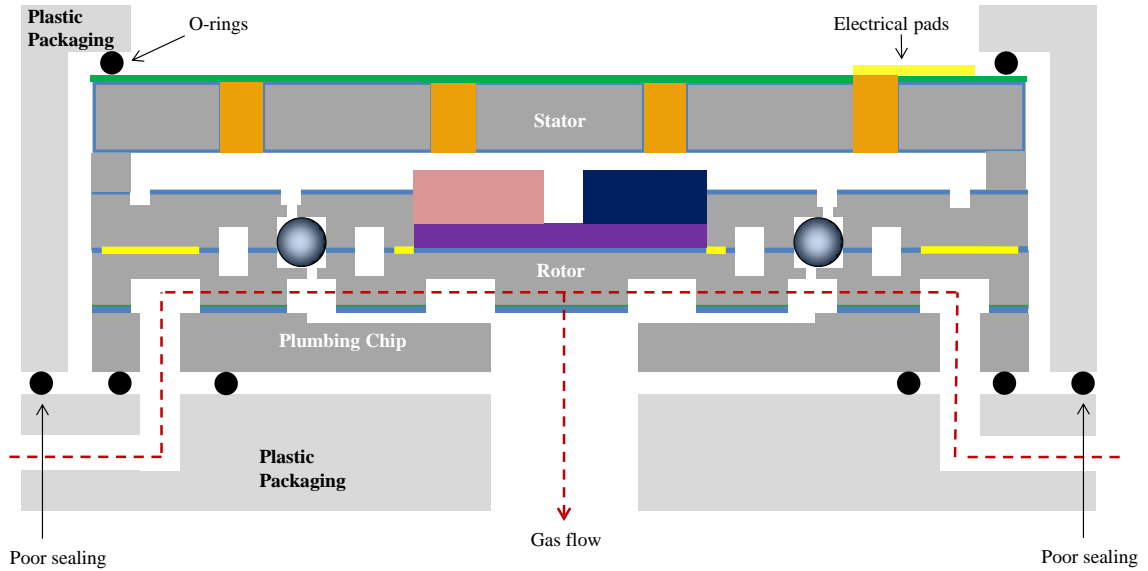
Figure 4.2. Schematic of the first generation packaging. The screws holding the two plastic pieces together are not shown.

The two plastic packaging pieces are held together by four screws that are not shown in Figure 4.2. As it will be mentioned later in this chapter, the first device was tested with this scheme. When the two pieces were completely screwed together, the O-rings in the package were supposed to pneumatically isolate the backside from the ambient and rotor top side. However it was later revealed that the O-ring between the two pieces of the plastic packaging did not seal the packaged volume mainly due to the package machining with lower than required precision. As a result, the rotor of the first device rotated on sharp silicon edges and high-speed testing could not be performed. Therefore, the second generation of packaging shown in Figure 4.3 was designed with a slight modification in the O-ring placement.
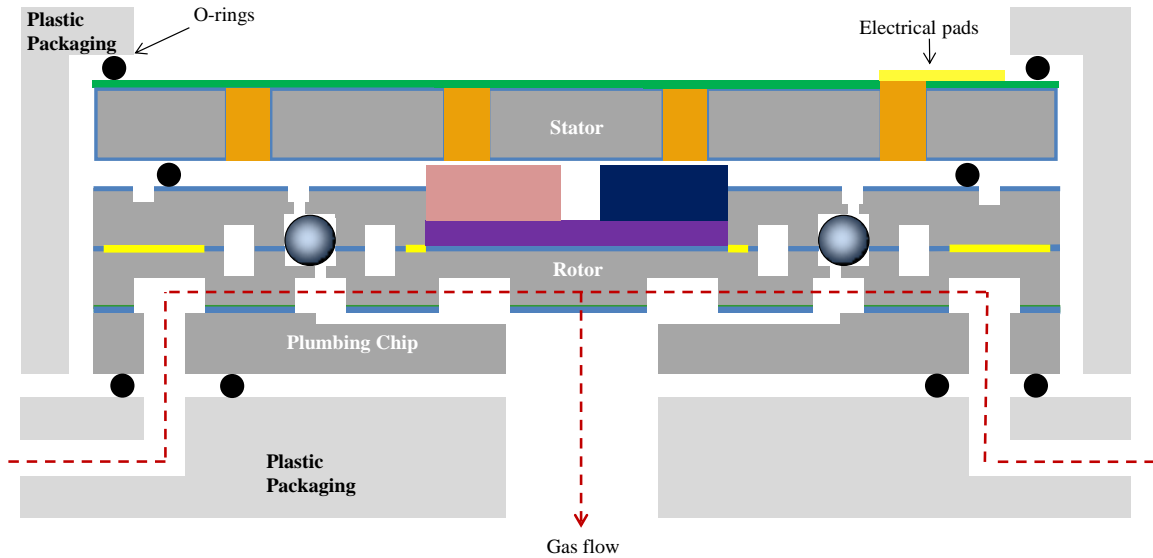
Figure 4.3. Second generation and final packaging scheme. The screws are not shown.

Four screws were again used to hold the two plastic packaging pieces together. As it can be seen from Figure 4.3, the O-ring in between the two plastic pieces was moved to the backside of the rotor in between the rotor and the stator. This packaging scheme resulted in perfect sealing of the rotor backside during later tests, and the necessary pressure build-up was achieved to obtain the force in downward direction. Although the placement of the O-ring between the rotor and the stator eliminated the dependency of sealing to precise package machining, it also led to the definition of the air gap by the same O-ring. Due to the compliant nature of this component, the air gap between the rotor and stator depends on how much the top plastic piece is pushed down by the screws. Assuming the O-ring is pressed down up to half of its thickness, this gap could be between ~200-700µm. Although the air gap is not perfectly controlled in this packaging scheme, the advantage of controllable air gap for the device still exists as the packaging can be improved to have more precise

112

machining with incorporated screw stoppers. The O-ring placed between the rotor and the stator also seals the top side of the stator as well, eliminating the need for a thin film passivation. The 3D design schematics with dimensions and pictures of the two plastic packaging pieces are shown in Figures 4.4 and 4.5, respectively. The inlets on the top plastic piece was first designed to control the rotor backside pressure in the first generation packaging scheme, but later not used and sealed when the packaging scheme was changed to the second generation design. A picture of a packaged micro-turbo-generator is also presented in Figure 4.6.

60mm

3.5mm

60mm

32mm

25mm

32mm

Fluidic port

6.5mm

(a)

19mm

90mm

60mm

Screw holes

11mm

15mm

Gas inlets and
fluidic ports

6.5mm
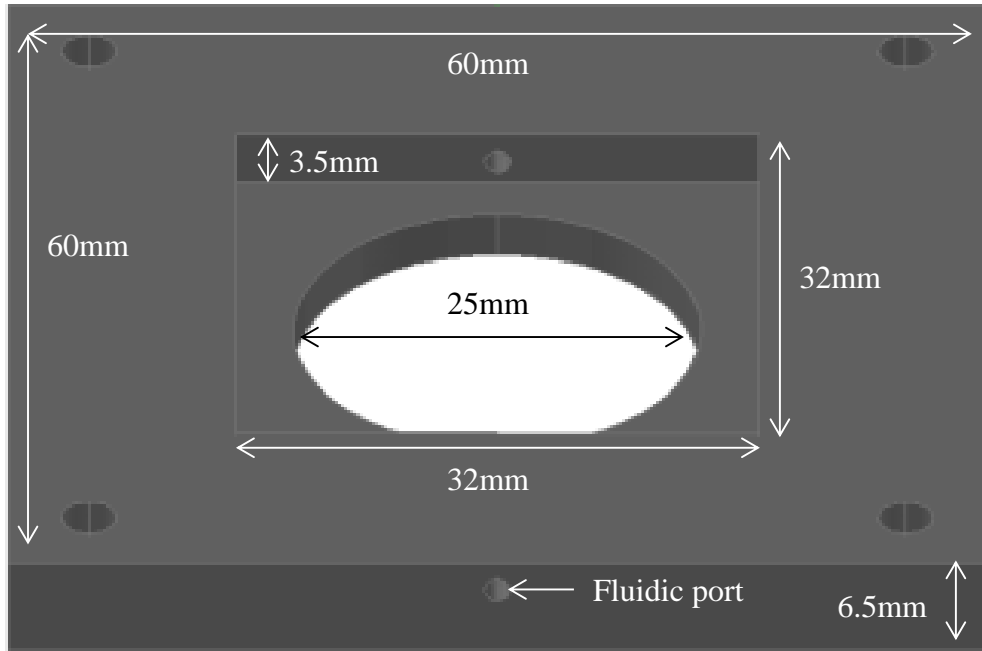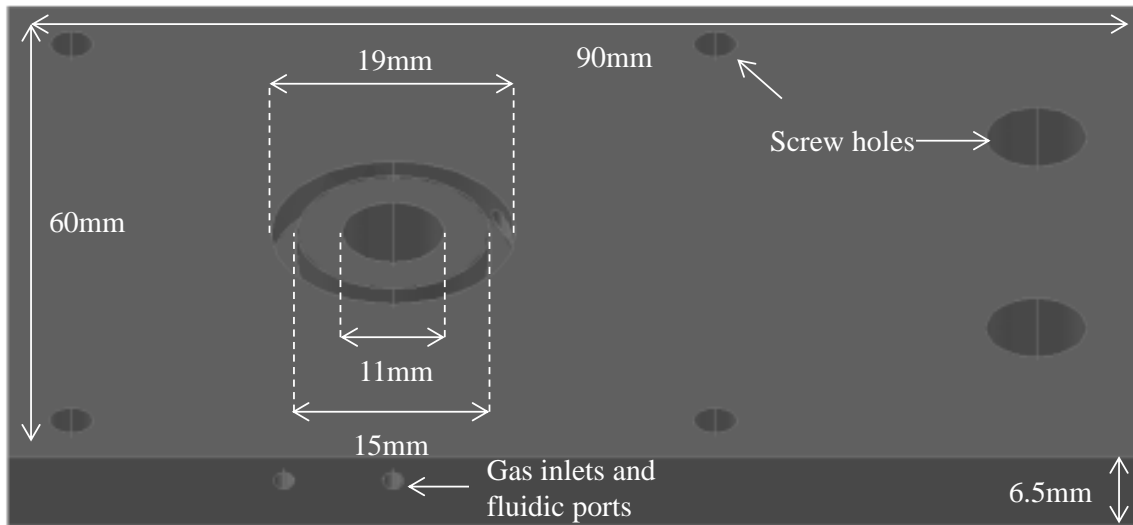
(b)

Figure 4.4. 3D schematics of (a) top and (b) bottom plastic packaging pieces with

dimensions.
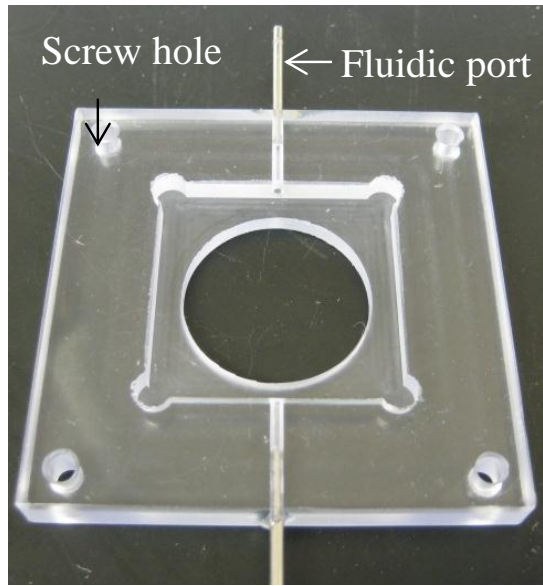
(a)
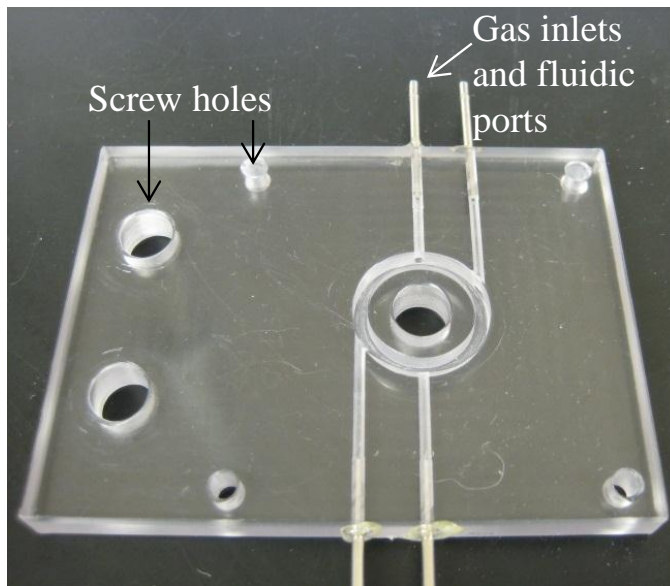
(b)

Figure 4.5. Pictures of the (a) top and (b) bottom pieces of the plastic packaging.
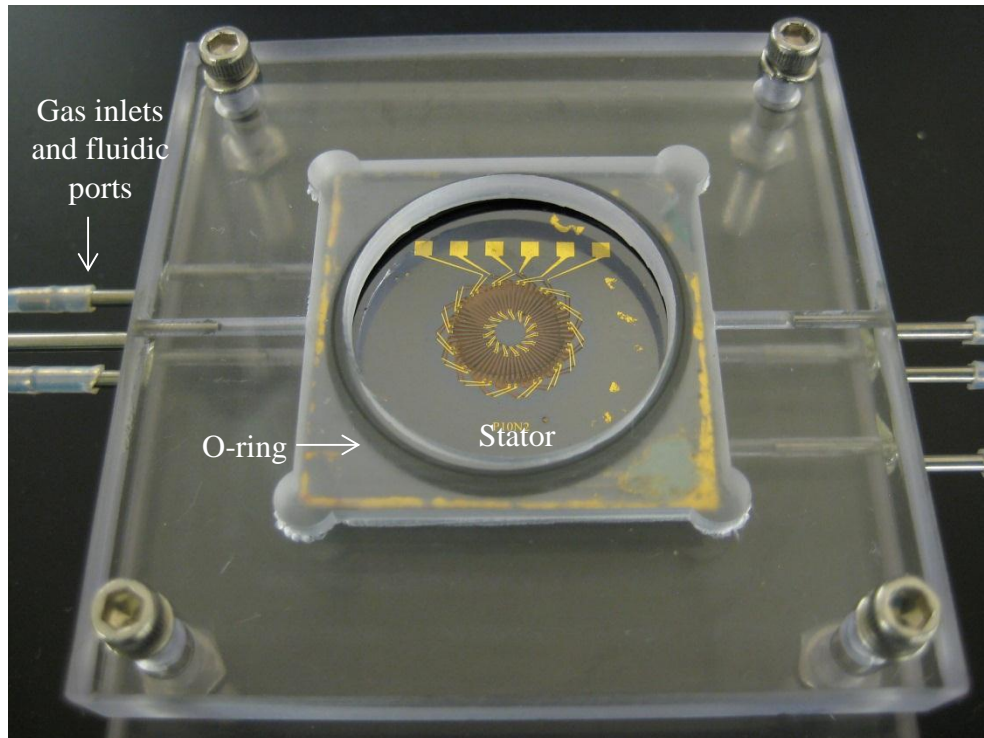
(a)
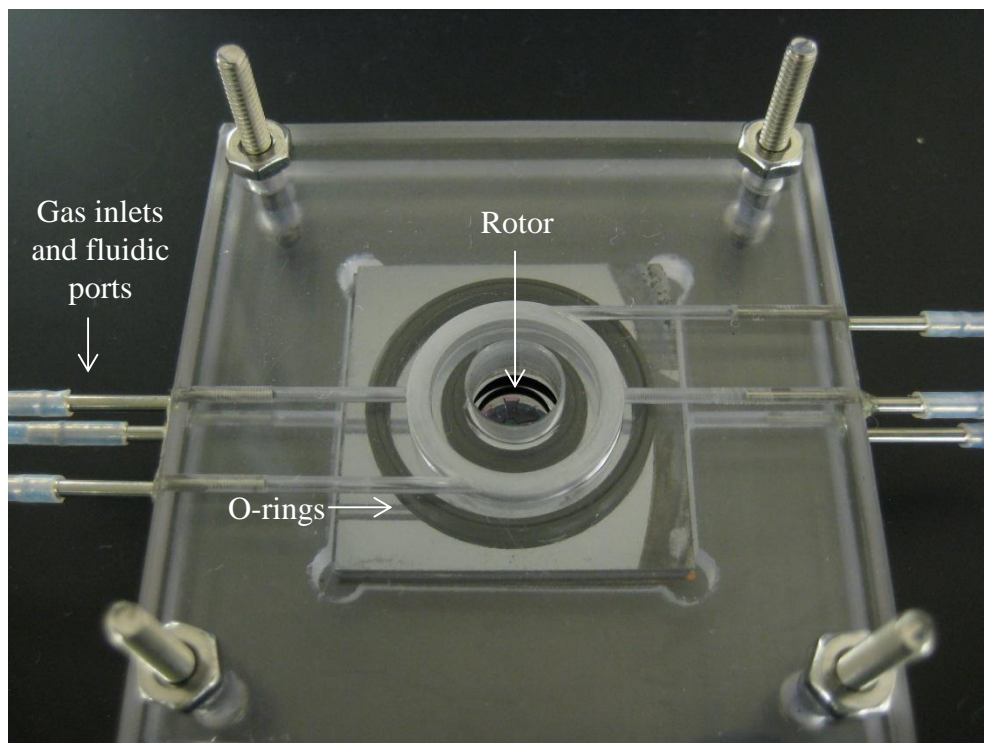
(b)

Figure 4.6. Picture of a packaged micro-turbo-generator (a) top view and (b) bottom view.

4.2. General Test Setup

Following the packaging design and manufacturing, a test setup was designed and built for the characterization of the micro-turbo-generator. In addition to the packaged device, this setup consists of a nitrogen tank as pressurized gas supply, a pressure regulator in series with valves for flow control, an Omega FM1700/1800 mass flow meter and an Omega PX138 pressure transducer for monitoring gas flow and pressure, a Philtec RC20-T4 optical probe for speed measurements, electrical probes for making connections to the phases, an electrical circuit with resistive loads for power delivery measurements, and a computer with LabVIEW program to monitor and record all these operating parameters. A schematic block diagram of this system is shown in Figure 4.7.
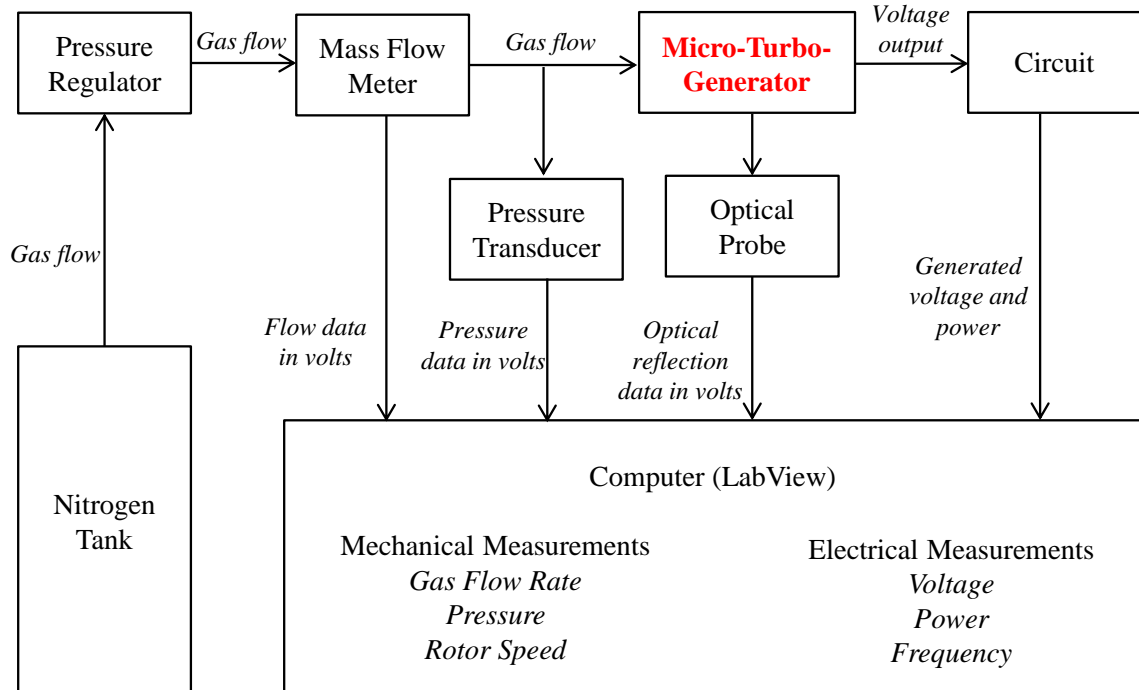
Figure 4.7. Block diagram of the testing setup.

The test setup operates as follows: Initially the optical probe was brought in close proximity of the rotor surface to detect the speed bumps etched in the center of the turbine side. Next, the gas lines were inserted in the package, connecting the output of the flow meter and the input of the pressure transducers to the device. The probes were then brought into contact with the phase pads. Before turning on the nitrogen valve, the regulator was adjusted to about 10psi max. This value was increased during the testing to reach higher speeds. Finally, the LabVIEW program was started and the valves were turned on to start spinning the rotor and testing the device. Although the device has three phases, only one phase in each tested device was successfully fabricated due to the problems in via connections related to fabrication issues. As a result, the initial three-phase electrical circuit was not used in testing the device and instead, a simple resistor was used as a matched load for power delivery characteristics. By excluding the electrical components and by replacing the stator with a same-sized silicon piece, the rotor component of the micro-turbo-generator was also tested with the same setup. The picture of this setup and LabVIEW program are shown in Figures 4.8 and 4.9, respectively.
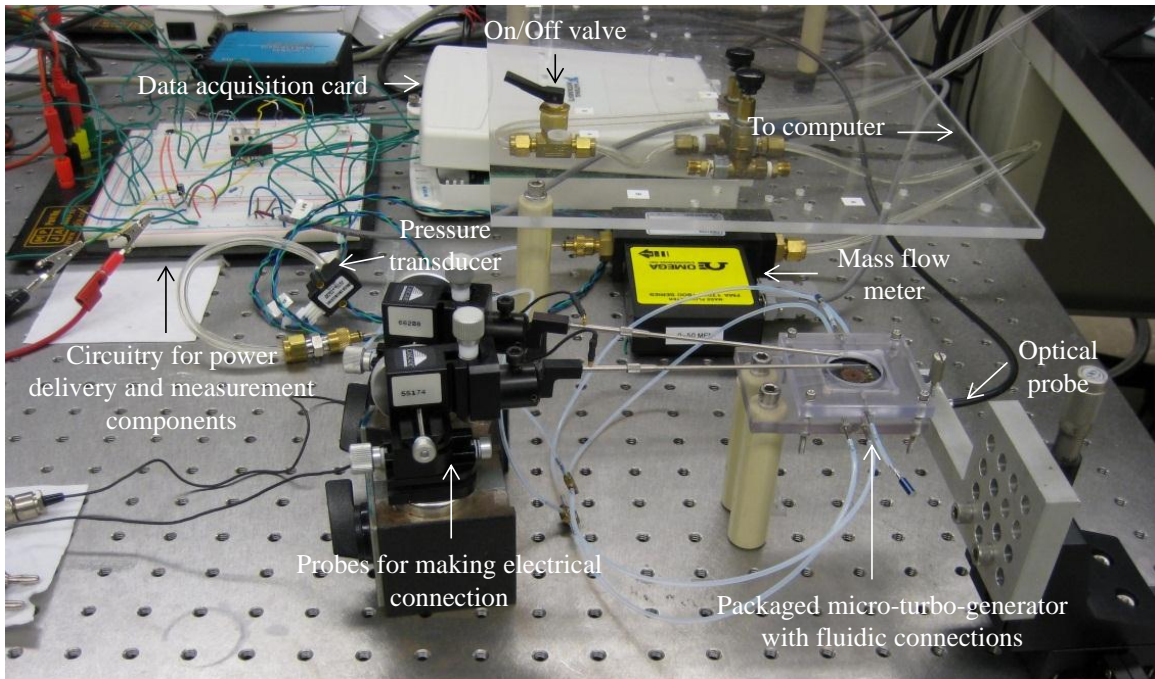
Figure 4.8. Picture of the test setup.
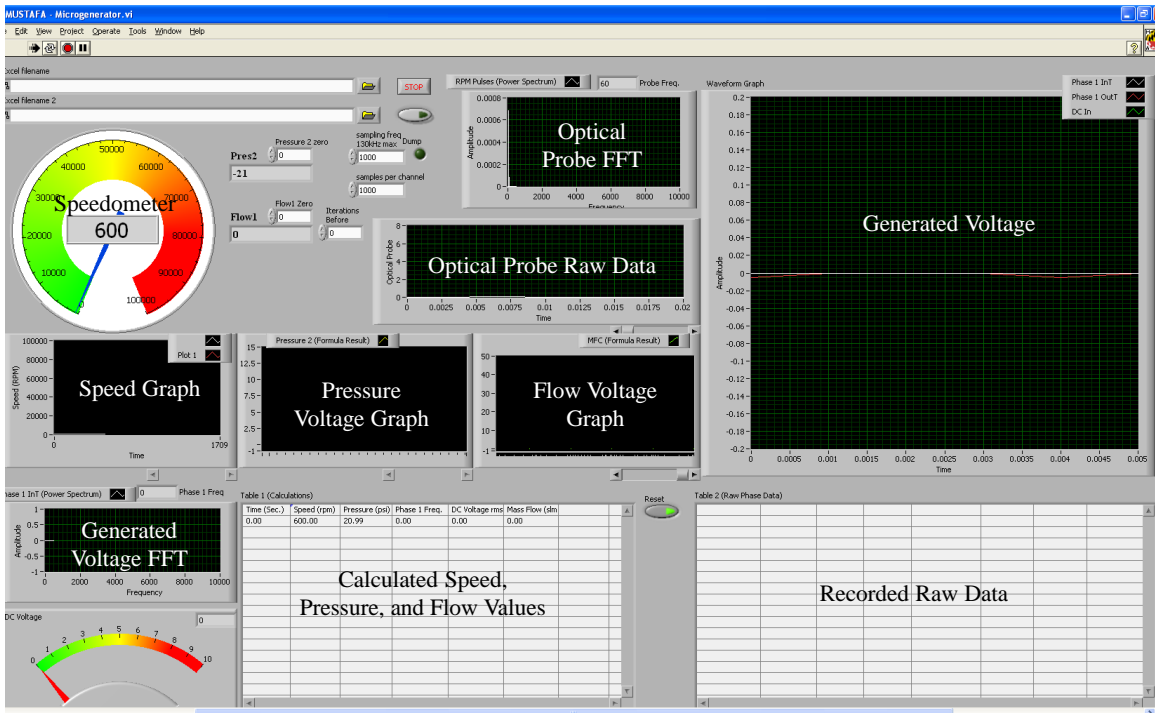
Figure 4.9. Picture of the LabVIEW program.

4.3. Magnetic Flux Density of Permanent Magnets

Prior to the complete device characterization as well as individual component testing, the magnetic flux density of permanent magnets were measured. The results of this characterization step are very important to make an accurate comparison between the theoretical estimations and experimental results. For this purpose, a separate test setup was built with a hall sensor fixed to a movable platform on top of the permanent magnets which were assembled on permendur disc. A picture of this setup is shown in Figure 4.10.
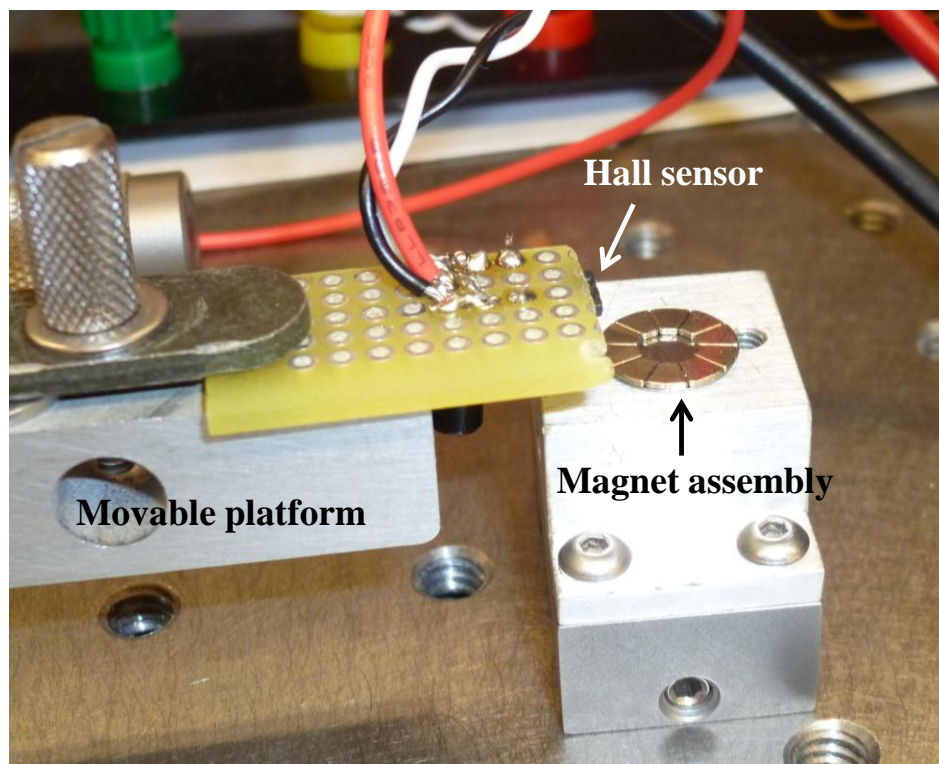
Figure 4.10. Picture of the test setup for permanent magnets.

The measurements were made at several locations on the surface of a single magnet and then repeated for a total of six magnets. Maximum flux density values

were calculated from the output voltage of the hall sensor, and averaged over these different magnets. The average maximum flux density was found to be 0.275T which is in very well agreement with COMSOL simulation results that estimate a magnetic flux density of 0.28T for this specific test. This shows that the magnets were fully magnetized up to their saturation value, and that the theoretical analysis and simulations for further performance estimations are valid.

4.4. Phase Electrical Parameters

Stator components of the two different micro-turbo-generators were characterized first to determine the phase electrical impedance parameters, i.e. the resistance and inductance. The capacitance is negligible since the spacing between the through-plated copper coils is very large. A simple calculation assuming that all three phase coil blocks are in parallel (highest possible capacitance) yields;

$$C = \frac{N\varepsilon A}{d} \approx 0.5nF$$

with $N = 100$, $A = 3mm \times 400\mu m$, and $d \approx 30\mu m$. At frequencies on the order of 10kHz, which is the maximum frequency that can be achieved with the device, this corresponds to a parallel impedance of;

$$Z \approx 35k\Omega$$

Considering the other impedance contributors, this is three orders of magnitude higher, and therefore negligible.

Phase resistances of the two stators were measured with a simple multimeter. Due to the thin backside connections, the phase resistances of the 10 pole 2 turns per pole and 10 pole 3 turns per pole designs were higher than the expected values and

were measured to be 46Ω and 220Ω, respectively. These values were highly determined by the geometry, number of via connections, and metal deposition conformity, and therefore can not be directly compared with each other.

The inductances of the stator phases were determined indirectly due to the lack of proper tools for inductance measurements by using a known resistance and an applied sinusoidal signal. Consider the circuit in Figure 4.11.
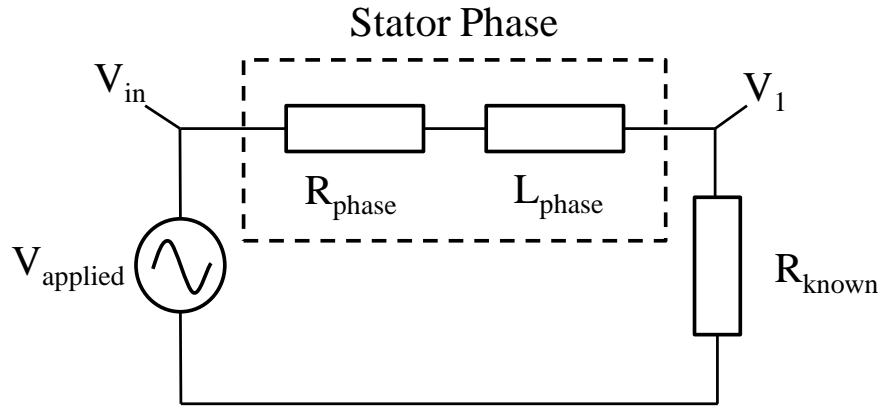
Figure 4.11. Test circuit for determining phase inductance.

In such a configuration, when $\dfrac{|V_1|}{|V_{in}|} = \dfrac{1}{2}$, then $\dfrac{|Z_1|}{|Z_{total}|} = \dfrac{1}{2}$. While $Z_1 = R_{known}$,

$Z_{total} = R_{phase} + 2\pi f L_{phase} + R_{known}$, and $|Z_{total}| = \sqrt{(R_1 + R_{knowon})^2 + 4\pi^2 f^2 L^2}$ where f is the applied electrical frequency. Since R_{phase} and R_{known} were already known, it is simple to back calculate the inductance when the measured V_1 was made half of the applied V_{in} by changing f. The two voltage signals, V_1 and V_{in}, in one of these tests are shown in Figure 4.12.
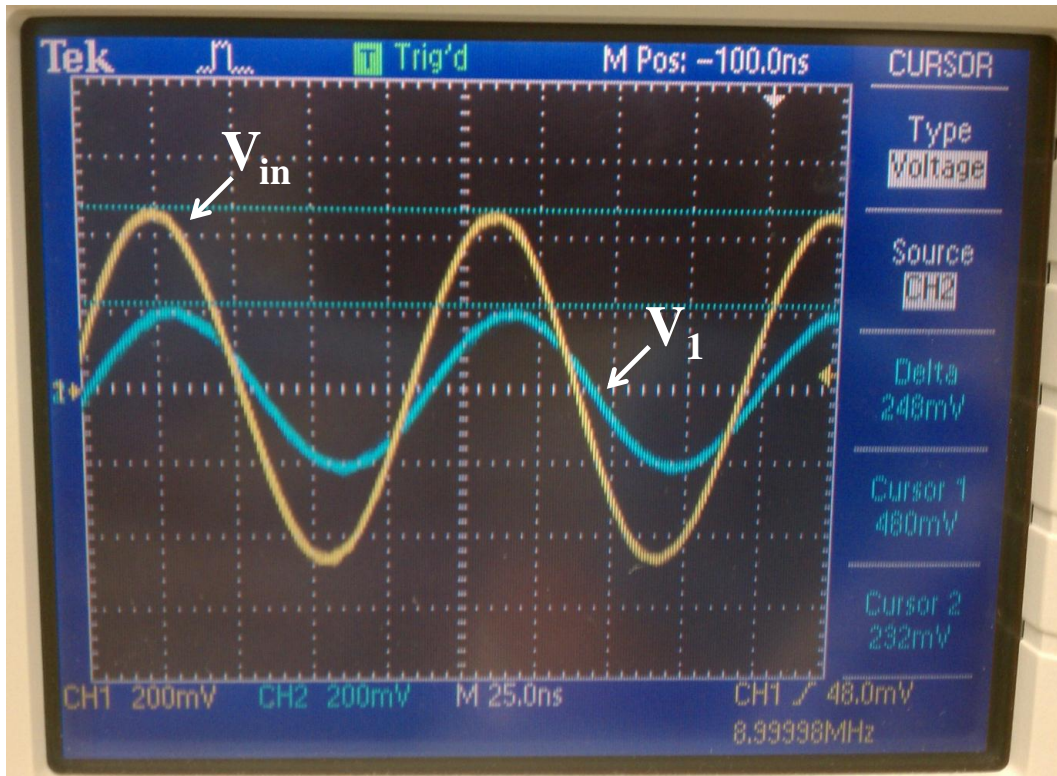
Figure 4.12. Oscilloscope outputs showing V_1 and V_{in} to determine phase inductance, note

that V_1 is approximately half of V_{in} and there is a phase difference between the two voltages.

Based on this test, the inductances of the 10 pole 2 turns per pole and 10 pole

3 turns per pole stator phases were measured to be 3μH and 3.5μH, which yields a

maximum impedance of 0.19Ω and 0.22Ω at the maximum frequency of 10kHz,

respectively. Note that these values are larger than the expected values presented in

Chapter 2 mainly due to the ignored mutual inductance effects and the parasitics

which were computationally intensive and therefore difficult to obtain from the

device simulations. However, these impedance values are still negligible compared to

the phase resistances. Finally, a potentiostat was used to apply a sinusoidal voltage

with varying frequencies while measuring the impedance simultaneously. Figure 4.13

below shows the constant 220Ω impedance of the 10 pole 3 turns per pole device up to frequencies of 10kHz, demonstrating the impedance is purely resistive within the device's operation range.
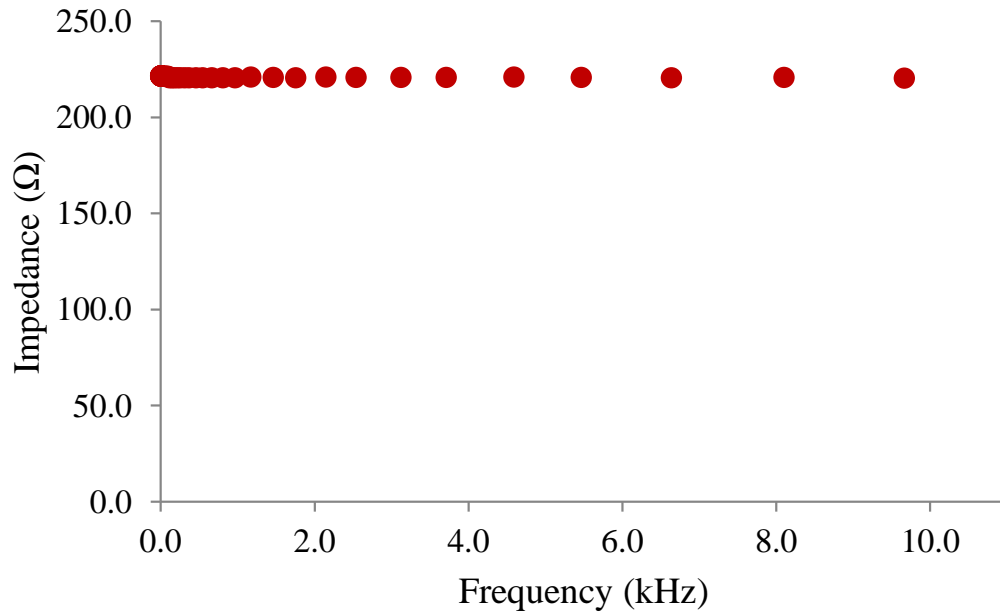
Figure 4.13. Impedance versus frequency curve of 10 pole 3 turns per pole stator measured by a potentiostat.

4.5. Rotor Mechanical Characteristics

Mechanical characterization of the rotor is essential to measure the friction torque and mechanical loss in the system. For this performance characterization, a procedure called spin-down testing, inherited from previously demonstrated microturbines in [8, 122], was followed. In this test, the turbine rotor with integrated permanent magnets was initially spun with pressurized nitrogen. Next, the flow was stopped and the rotor decelerated under the effect of friction. While the rotor slowed

down, angular position versus time data was recorded using the optical probe and a separate LabVIEW program specifically designed for this test. Finally, a Matlab code was used to remove the constant speed portion of the operation, process this data, and obtain the rotor deceleration curve. Figure 4.14 shows the deceleration of a 10 pole rotor from 16krpm as a result of the spin down test.

$$\theta = A(1 - e^{-Bt})$$
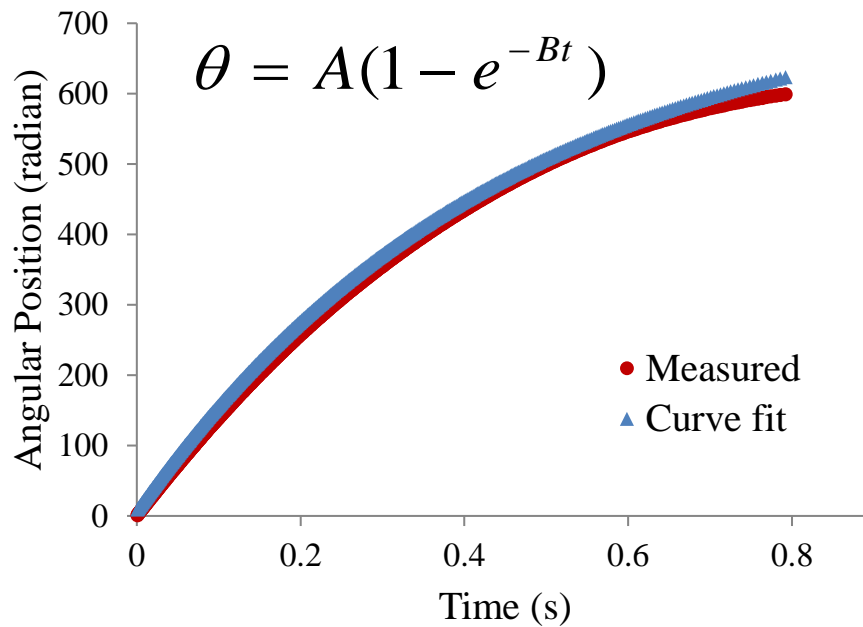
Figure 4.14. Deceleration of a 10 pole rotor under friction and the curve fit based on the previously developed friction model.

The previously developed friction model reported in [122] was used to calculate the deceleration of the rotor. In this model $\theta = A(1 - e^{-Bt})$ where θ is the angular position in radians, A and B are constants, and t is time. A curve with this formula was fit to the measured data with an r^2 value of 0.99, yielding A and B to be 740 and 2.25, respectively. The deceleration, which is the second derivative of

angular position with respect to time, now can be calculated using the time values on

the graph with $\frac{d^2\theta}{dt^2} = AB^2 e^{-Bt}$. To find the friction torque, the moment of inertia of

the rotor is also needed. To calculate this value, the rotor was assumed to be a

uniform disc, so that $I = \frac{mr^2}{2}$ where m is the rotor mass which was measured to be

~0.5g and r is the radius of 6mm. Consequently, the friction torque is $\tau = I \times \frac{d^2\theta}{dt^2}$

which gives a range of values depending on the time, and hence the rotor speed.

When all the numbers are put in the equations, the friction torque was found to be

5.5µNm - 33µNm between the speed values of 0rpm – 16krpm, respectively. In

comparison to the demonstrations of microball bearings in other devices in [8, 122],

the rotor has higher friction due to the 44% higher surface area, 20% more microballs

in the raceway, and four-fold increase in the total mass. Note that the 5.5µNm friction

torque is not the static torque at the 0rpm, but rather a dynamic torque at a speed very

close to 0rpm. The static friction torque value is believed to be higher than this value.

Once the friction torque is determined, the absorbed power dissipated by

friction can be calculated by $P = \tau \times \frac{d\theta}{dt}$. This formula yields a frictional power on

the order of 50mW at 16krpm. This test could not be repeated at higher speeds as the

rotors broke due to various reasons explained below during the electrical power

delivery tests. Note that this value cannot be compared to the formula presented in

Chapter 2 mainly due to the inability to measure the normal force on the rotor during

the operation. However, when equation (2-20) was considered with the above power

value, the normal force is calculated to be ~1N which was within the estimation range presented in Chapter 2.

4.6. Micro-Turbo-Generator Performance

Performing the electrical and mechanical tests on the stators and rotors individually, these components were combined together in the previously described plastic packaging to measure the performance of the micro-turbo-generator. Two stators with 10 pole 2 turns per pole and 10 pole 3 turns per pole, and two practically identical 10 pole rotors (one for each stator) were fabricated, as mentioned before. Although the stators were designed to have three phases, only one phase in each device was successfully fabricated due to fabrication-related challenges. Therefore, one phase AC power generation was demonstrated for each device. Figure 4.15 shows a packaged micro-turbo-generator before testing.
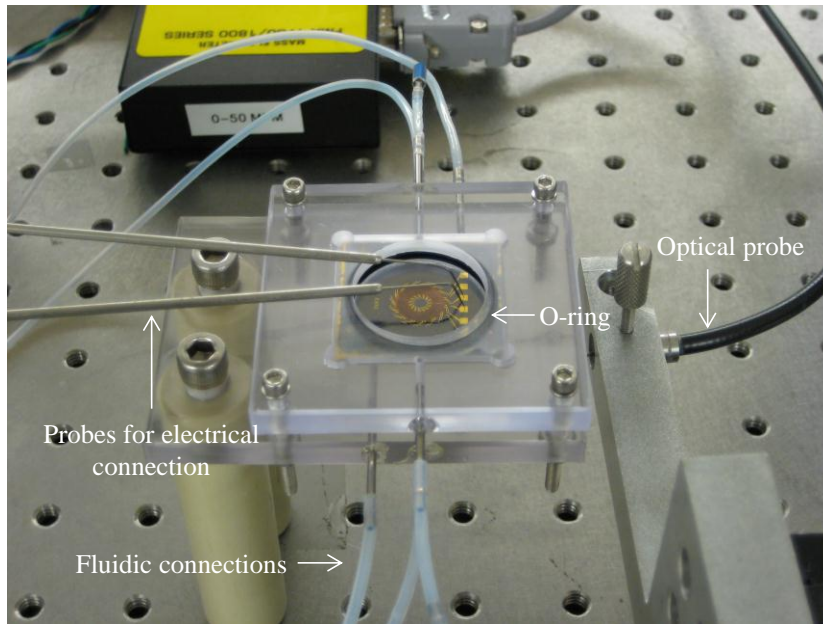
(a)
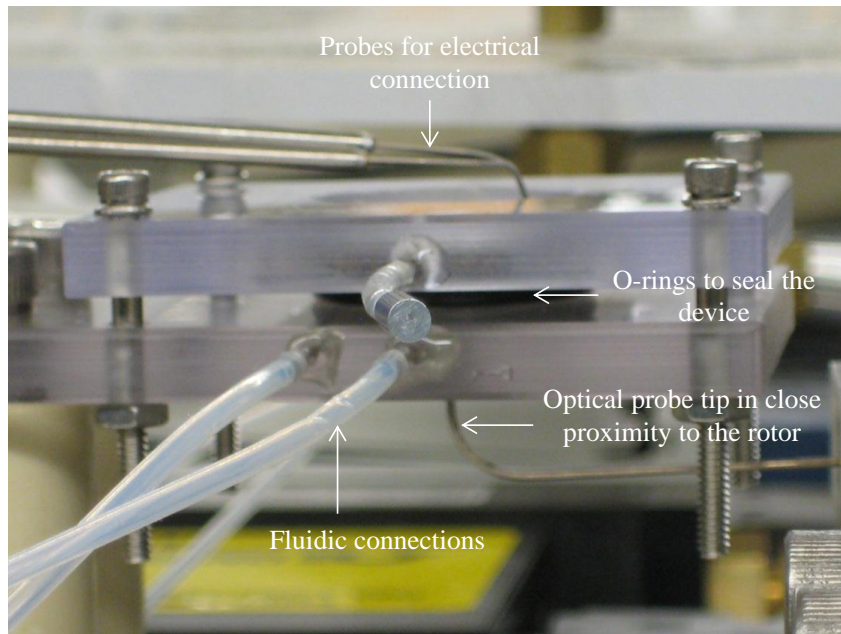
(b)

Figure 4.15. Picture of a packaged micro-turbo-generator (a) top view and (b) side view.

Previously described test setup and LabVIEW program were used to characterize the performance of the micro-turbo-generators. Initially, open circuit

voltages of the devices were measured at increasing rotor speeds. The rotor-to-stator air gap was not precisely set due to the use of an elastic O-ring between these two components, and was determined by how much the packaging screws were tightened. Therefore, equation (2-8) should be further expanded to calculate a range of expected values rather than a single value. The term that is affected by the varying gap in equation (2-8) is the average flux density (B_g), and hence magnetic flux density simulations had to be repeated for the maximum and minimum air gap conditions. Assuming that 1mm-thick O-ring can be squeezed up to half its thickness and given that permanent magnets protrude about 300μm from the rotor surface, the air gap between the surfaces of the magnets and the stator is 700μm when the O-ring is not pressed down, and 200μm when it is pressed down to half its thickness as explained previously. Repeating the COMSOL simulations for these gaps, magnetic flux density values of 0.109T – 0.28T were obtained for the air gaps of 700μm - 200μm, respectively. Based on these values, the expected voltage ranges were calculated for the two different devices. Figures 4.16 and 4.17 show the measured open circuit voltages with respect to rotational speed as well as linear curve fits for 10 pole 2 turns per pole and 10 pole 3 turns per pole devices, respectively. These figures also include the expected range of voltages, shown by the shaded regions, with maximum and minimum border lines calculated by using the flux density values mentioned above. The induced open circuit voltages of 10 pole 3 turns per pole device at three selected speeds are also shown in Figure 4.18 for the demonstration of increasing amplitude and frequency with increasing speed.
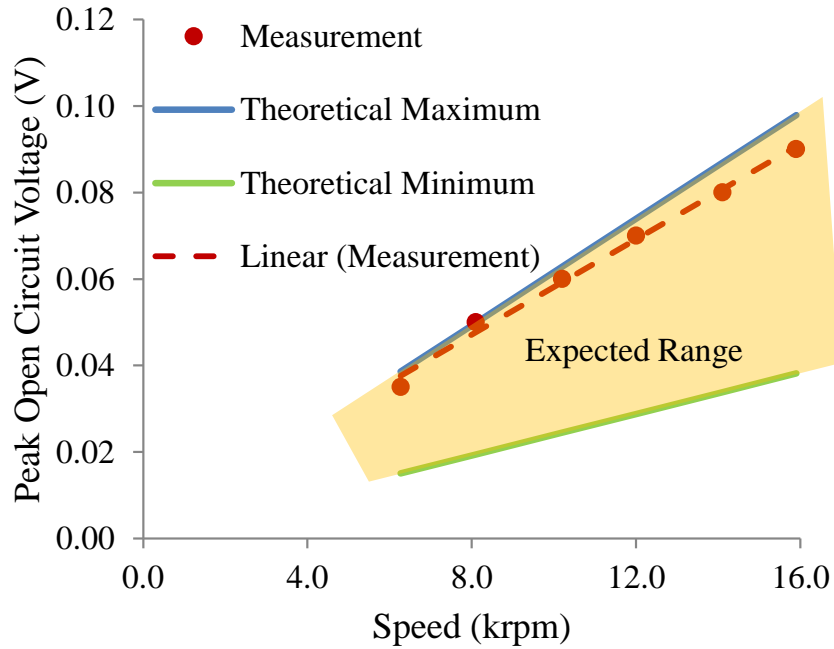
Figure 4.16. Measured open circuit voltages and range of expected values for 10 pole 2 turns per pole device.
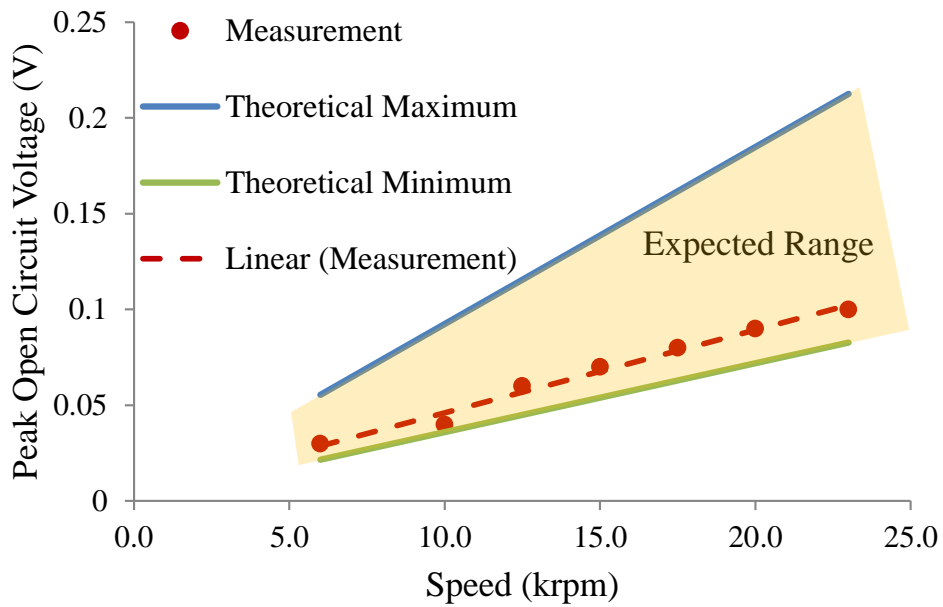
Figure 4.17. Measured open circuit voltages and range of expected values for 10 pole 3 turns per pole device.
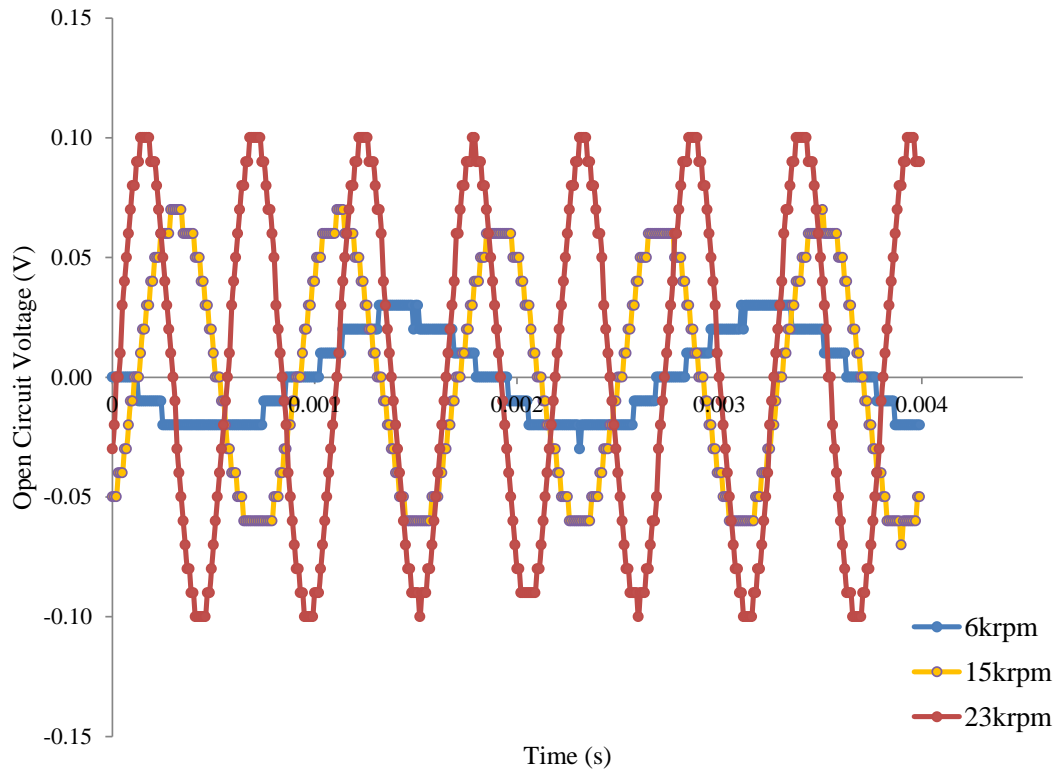
Figure 4.18. Induced sinusoidal open circuit voltages of 10 pole 3 turns per pole device at 6krpm, 15krpm, and 23krpm demonstrating the increasing voltage amplitude and frequency with increasing speed.

Sinusoidal voltages with a maximum peak value of 0.1V at 23krpm (from 10 pole 3 turns per pole device) was achieved. Ideally, induced voltages were expected to be trapezoidal as described in Chapter 2. However, due to the leakage fluxes at the magnet edges as well as imperfect magnetization towards the corners of the magnets, the shape of the induced voltage approaches from trapezoidal to sinusoidal. These two graphs in Figures 4.16 and 4.17 show that the experimental values fall within the theoretical estimations, demonstrating the accuracy of the analysis and simulations. Furthermore, the data follows an expected linear relationship with the rotational

speed. Note that the obtained results are very close to the theoretical maximum for the 10 pole 2 turns per pole device while the results from 10 pole 3 turns per pole device are closer to the theoretical minimum curve. This is mainly due to the fact that the tests were conducted more cautiously for the latter device to apply less pressure on the chips and avoid any fracture, and hence the screws were tightened lightly. For both devices, higher speeds could not be achieved due to the reasons explained in the next subsection. However, it is worth to mention that mechanical stability limit was not reached, and that higher speeds can be achieved with possible improvements in device microfabrication.

The two devices were then tested for power delivery to electrical loads. To extract the maximum power, the impedance of the electrical loads was chosen to be equal to that of the stator phases, i.e. 46Ω for 10 pole 2 turns and 220Ω for 10 pole 3 turns stators. This is a condition called the matched load condition where the power delivery is maximum, stated by Thevenin's theorem, and the electrical power delivery efficiency is 50%. Figure 4.19 shows the voltage induced on 46Ω load resistor sourced by 10 pole 2 turns per pole device at 10krpm, demonstrating power delivery. Due to the problems associated with rotor operation of this device that will be described in the next subsection, power measurements at higher speeds could not be performed. Figure 4.20, however, shows the output power of the 10 pole 3 turns per pole device on 220Ω load resistor for a range of rotational speeds. Power was calculated by the formula $P_{out} = \dfrac{V^2_{rms}}{R_{load}}$, where V_{rms} is the rms value of the induced voltage measured between the terminals of the load resistor while the micro-turbo-generator was being operated at a specific speed.

132
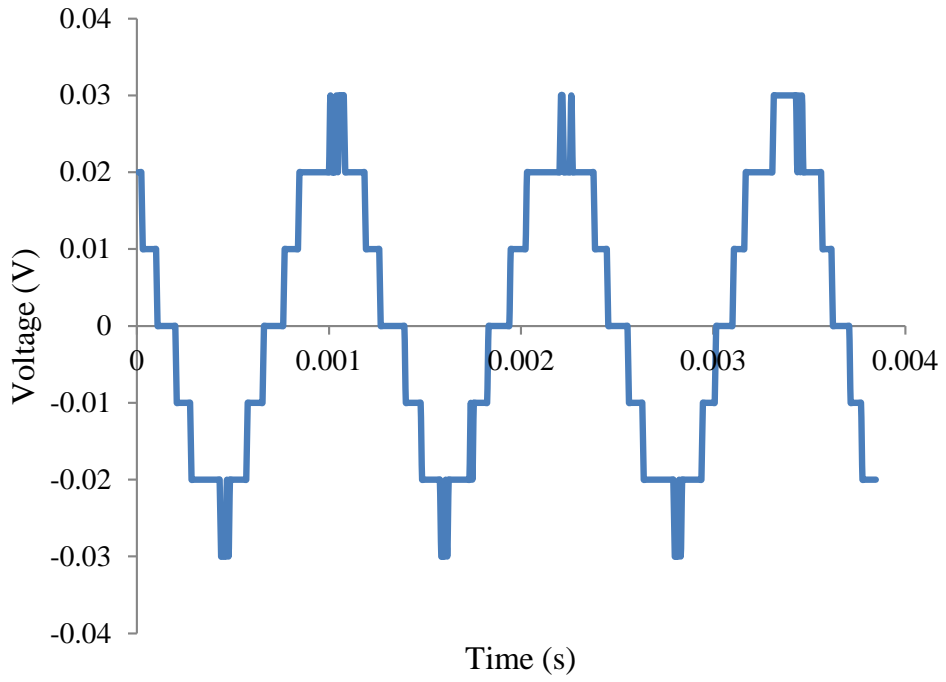
Figure 4.19. Induced voltage on 46Ω resistor at 10krpm sourced by 10 pole 2 turns device.
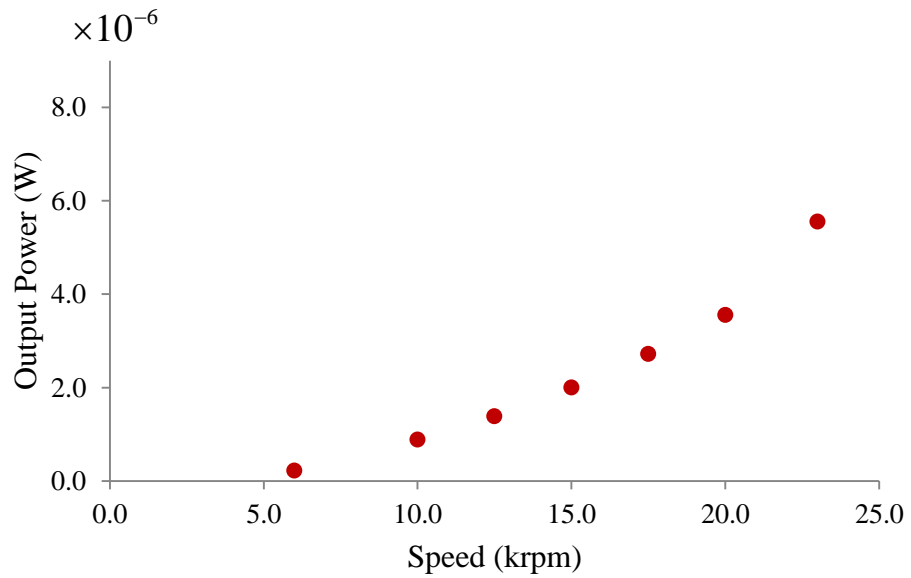
Figure 4.20. Power versus speed curve of 10 pole 3 turns per pole device with 220Ω load resistor.

Due to the 10mV resolution of the data acquisition card for the LabVIEW program, the data on Figure 4.19 does not look like a sinusoidal voltage and is rather digitized. This induced voltage corresponds to 10μW AC power on 46Ω load resistor at 10krpm. For both devices, the load voltage is exactly half of the open circuit voltage at a given speed as expected, which demonstrates that the phase impedance is well-characterized and that the matched load condition holds. Figure 4.20 shows an expected parabolic power versus speed curve with a maximum output power of 5.6μW delivered to a 220Ω resistor at 23krpm. Note that although the voltage and the speed of 10 pole 2 turns per pole device are lower than that of 10 pole 3 turns per pole device, the output power of the 10 pole 2 turns per pole device is higher mainly due to its lower phase resistance and lower rotor-to-stator air gap. The active volume of the micro-turbo-generator is ~0.17cm^3, and hence the power density values of the 10 pole 2 turns per pole and 10 pole 3 turns per pole devices were calculated to be 59μW/cm^3 and 33μW/cm^3, respectively. The voltage and power values of the two devices prohibited the use of diodes and transformers for AC/DC conversion, and therefore limited the generation to AC power rather than DC.

During the operation of the device, applied gas flow rate and pressure were also measured in liters per minute and psi, respectively, to calculate the applied mechanical power and overall efficiency. Figures 4.21-4.22 and 4.23-4.24 present the dependency of these parameters with respect to speed for the two practically identical ten pole rotors of 10 pole 2 turns per pole and 10 pole 3 turns per pole devices, respectively.
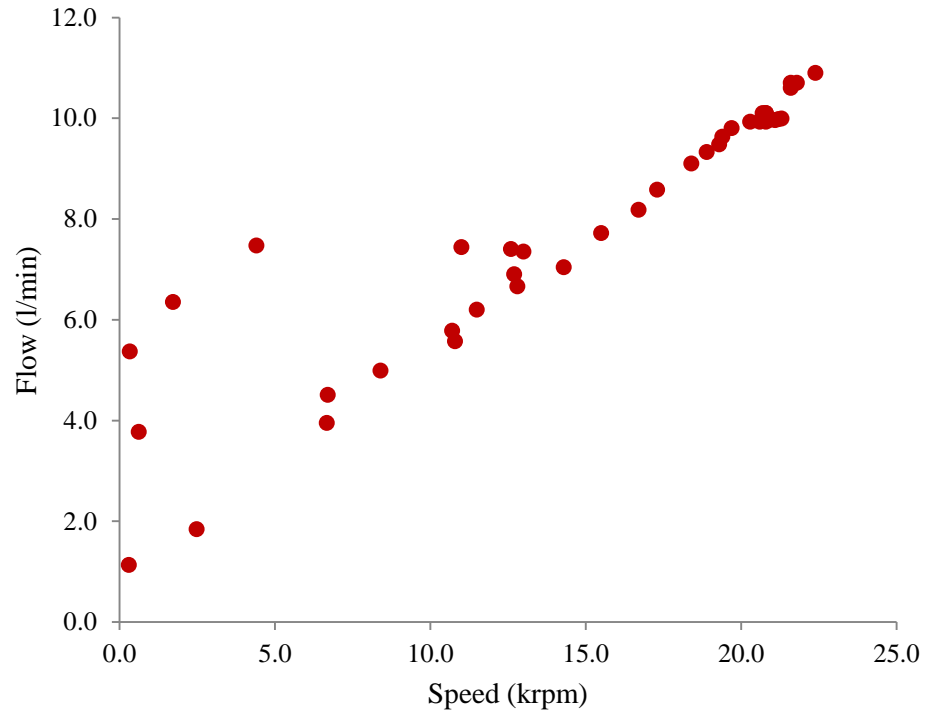
Figure 4.21. Gas flow versus speed curve for the rotor of 10 pole 2 turns per pole device.
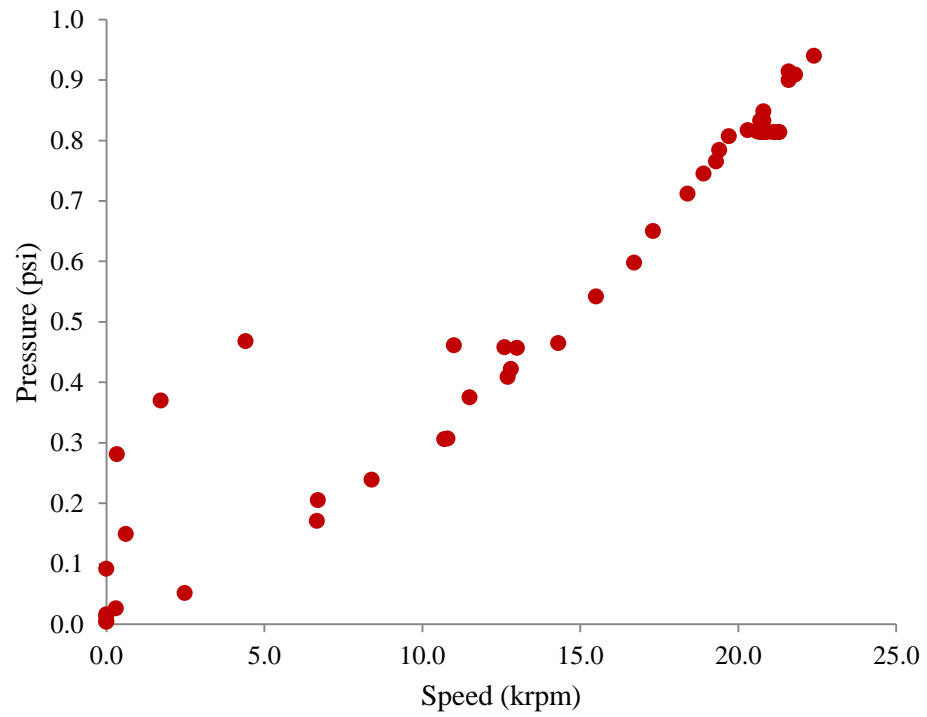
Figure 4.22. Pressure versus speed curve for the rotor of 10 pole 2 turns per pole device.
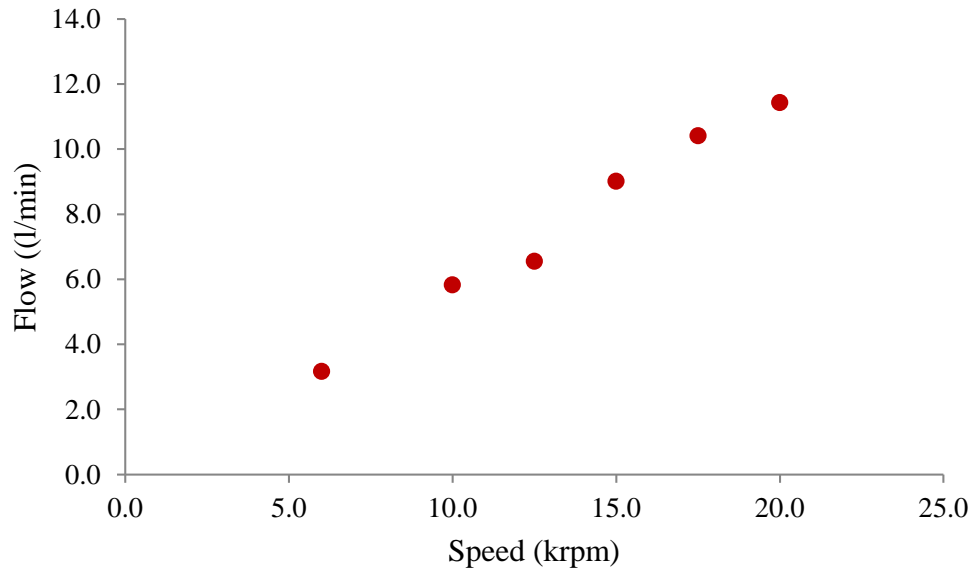
Figure 4.23. Gas flow versus speed curve for the rotor of 10 pole 3 turns per pole device.
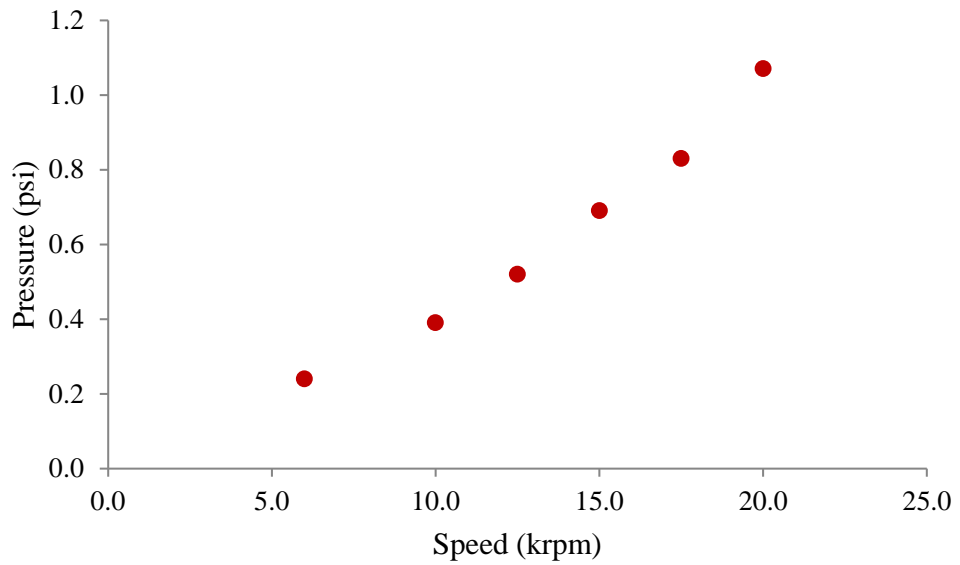
Figure 4.24. Pressure versus speed curve for the rotor of 10 pole 3 turns per pole device.

The data presented in Figures 4.21 and 4.22 were obtained from tests specifically aimed to probe the pressure and flow by using a separate LabVIEW program. Therefore, there are more data points compared to Figures 4.23 and 4.24 which were obtained by simultaneously measuring these parameters and delivered power at specific speeds. The data in Figures 4.21 and 4.22 are from a fresh rotor, and therefore it is somewhat scattered which is attributed to the artifacts of the fabrication imperfections that wear away during the first few cycles. The required flow and pressure for the two rotors at any given speed are very close in value that shows the consistency and repeatability in the mechanical performance of the two rotors.

The output power, input flow, and pressure values allow us to calculate the efficiency of the micro-turbo-generator. Mechanical input power can be calculated as $P_{in} = 0.115 \times flow \times pressure$, where P_{in} is in watts, *flow* is in liters per minute, and *pressure* is in psi. The efficiency can then be written as $\eta = \dfrac{P_{out}}{P_{in}}$. When the values are plugged in for the 10 pole 2 turns per pole device, the efficiency is found to be ~ 6×10^{-5} at 10krpm. A more clear picture is present for the 10 pole 3 turns per pole device due to the availability of more data points. Figures 4.25 and 4.26 show the input mechanical power and efficiency versus speed, respectively.
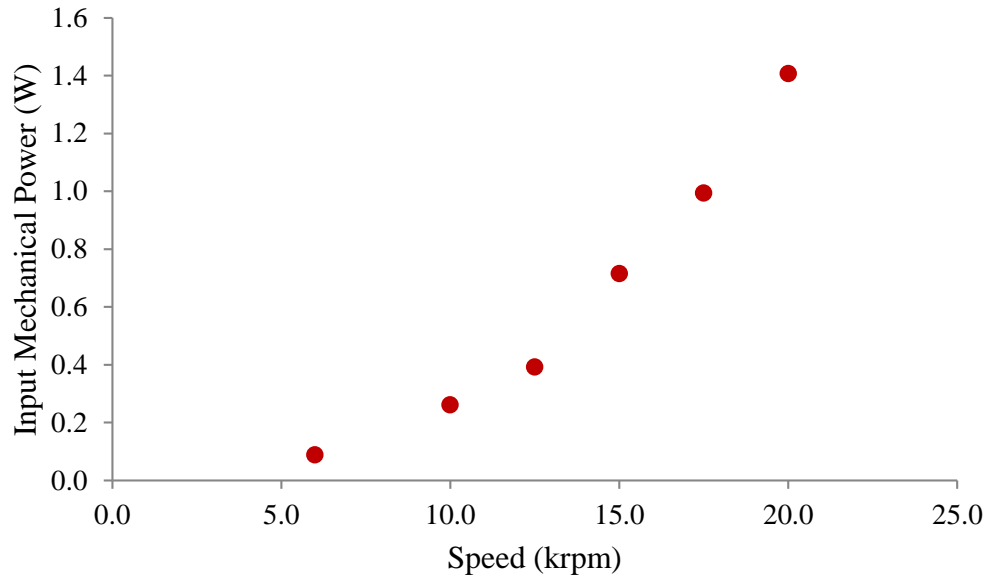
Figure 4.25. Input mechanical power versus speed for 10 pole 3 turns per pole device.
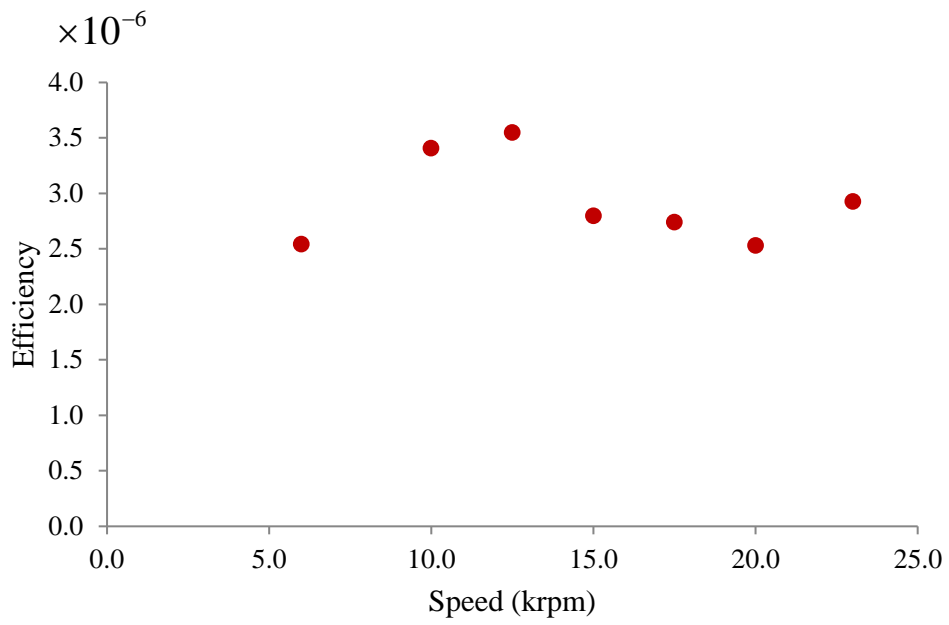
Figure 4.26. Efficiency versus speed for 10 pole 3 turns per pole device.

138

As it can be seen from Figure 4.26, the efficiency is on the order of 3×10^{-6}. Since the input flow and pressure values for the two devices are very similar, the reason behind the order of magnitude difference in efficiencies is again high rotor-to-stator air gap and high resistance of the 10 pole 3 turns per pole device. At this point, the efficiency can be divided into three different parts as $\eta = \eta_{mech} \times \eta_{el} \times \eta_{load}$ where η_{mech} is the conversion efficiency in pressurized gas power to turbine rotation, η_{el} is the conversion efficiency between the turbine rotation to electrical power, and η_{load} is assumed to be 50% due to the matched load condition. It should be noted that the only electrical loss mechanism is the eddy currents induced in the coil windings. A rough calculation using eq. (2-17) yields eddy current power loss values on the order of 100μW. Since the generated electrical power is very small compared to the frictional power loss of 50mW at 16krpm, η_{mech} can be roughly calculated as $\eta_{mech} = \dfrac{50mW}{P_{in}}$. The 50mW value was measured at 16krpm, and can be used to calculate an approximate value for this efficiency. When the input mechanical power value of 0.8W at 16krpm is plugged in the above equation, η_{mech} is found to be on the order of 6%. As a result, η_{el} becomes 2×10^{-3} for the 10 pole 2 turns per pole device, and 1×10^{-4} for the 10 pole 3 turns per pole device, respectively. This shows that most of the input mechanical power is dissipated against friction.

4.7. Discussion

The results discussed in the above sections demonstrate the first successful development and operation of an integrated microball bearing supported

139

electromagnetic micro-turbo-generator. Well agreement with the theoretical calculations and experimental results prove the accuracy of design analysis and simulations. The output voltage and per-phase AC power were shown to be on the order of 0.1V and 10μW, respectively with a power density of up to 59μW/cm^3. Conversion from AC to DC requires a combination of diodes and optionally transformers. The use of these components in an AC/DC conversion circuit, however, would result in zero output voltage and power due to the voltage drops on the diodes and power dissipation in the transformers. Therefore, the output voltage and power values of the micro-turbo-generator limited the operation to AC power generation. The measured power values are lower compared to the previously demonstrated devices in [69-93] due to *low rotational speeds* and *fabrication challenges* involved in device manufacturing, which are the two factors that prevented achieving higher performance. Issues with the fabrication process also limited the AC power generation to single phase rather than three phase.

Low rotational speeds for the two rotors were caused by the problems with the initial plastic packaging described previously, and the low bonding strength between the two wafers of the rotor. The first successful rotor was tested with the 10 pole 2 turns per pole stator with the initial packaging scheme in Figure 4.2. The poor sealing led to pressure imbalance and caused the rotor to be pushed up and rotate on the sharp silicon edges of the ball raceway. This resulted in excessive wear and material build up on the raceway, and severely affected the performance of the device. This device is still operational, however the speed cannot be maintained constant beyond 10krpm.

The rotor of the 10 pole 3 turns per pole device suffered from the breaking of the eutectic bond holding the two rotor wafers together. In fact, two wafers came un-bonded after the first DRIE release etch, i.e. before the end of fabrication. Since the bonding could not be repeated in a bonding tool at that point, these wafers were re-bonded at 450ºC with 50g weight on top in a furnace and the fabrication was completed. During the operation, there is a net torque applied to the turbine blades arising from the gas flow, which is also exerted to the bonding interface. As the gas flow is increased to reach higher speeds, the magnitude of the applied torque also increases. The weak bond between the two wafers could withstand this torque up to 23krpm, and broke at 25krpm. Therefore, higher speeds could not be achieved.

Successful operation of this device before un-bonding proved the effectiveness of the package sealing. Similar microturbines that are developed as part of a separate ongoing research at MSAL utilize exactly the same kind of bonding without any problems. Therefore, the bond breakdown is believed to be caused by random tooling problems that occurred during the eutectic metal deposition and bonding processes such as faulty equipment operation, contamination, different material composition, or material oxidation. Since AuSn eutectic metal was evaporated on most of the rotors at the same time, the bond in other rotors also failed before successful testing. This can be alleviated in future generation devices by depositing the eutectic metal on one rotor at a time. The only disadvantage, however, is the high cost of AuSn. It can be concluded from the failure mechanisms that the speed stability limit was not reached, and that the rotor can be stably operated beyond 23krpm.

After the bond break down, the ball raceway was scanned using an optical profilometer. The profile scan and an SEM image of the raceway are shown in Figures 4.27 and 4.28, respectively.
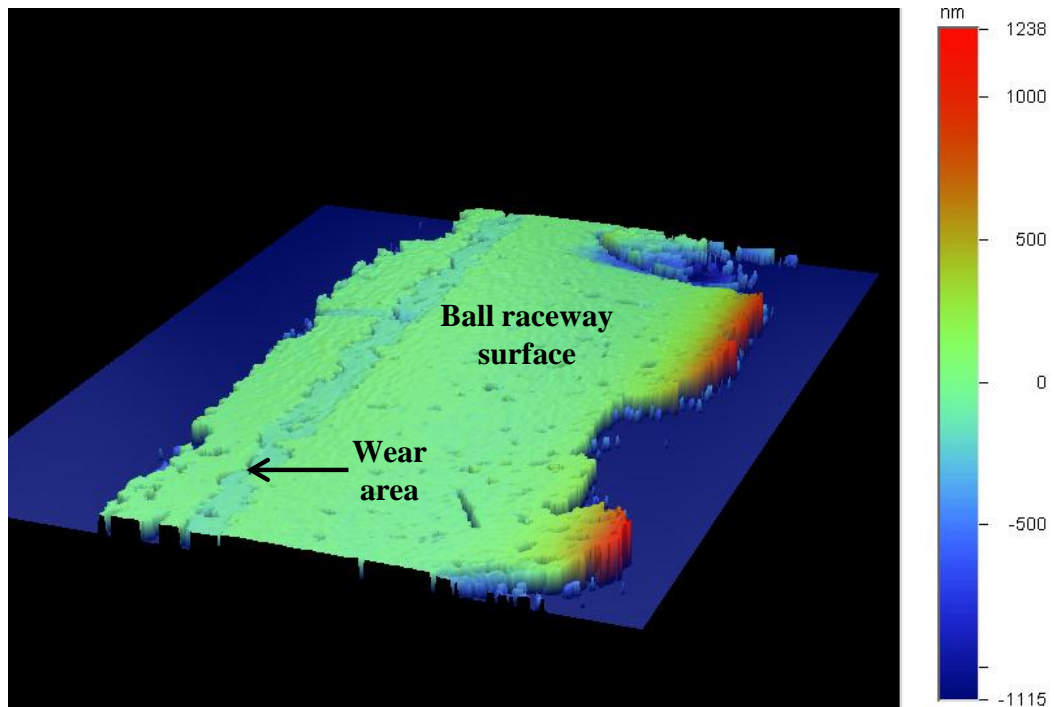
Figure 4.27. Profile scan of the ball raceway showing wear.
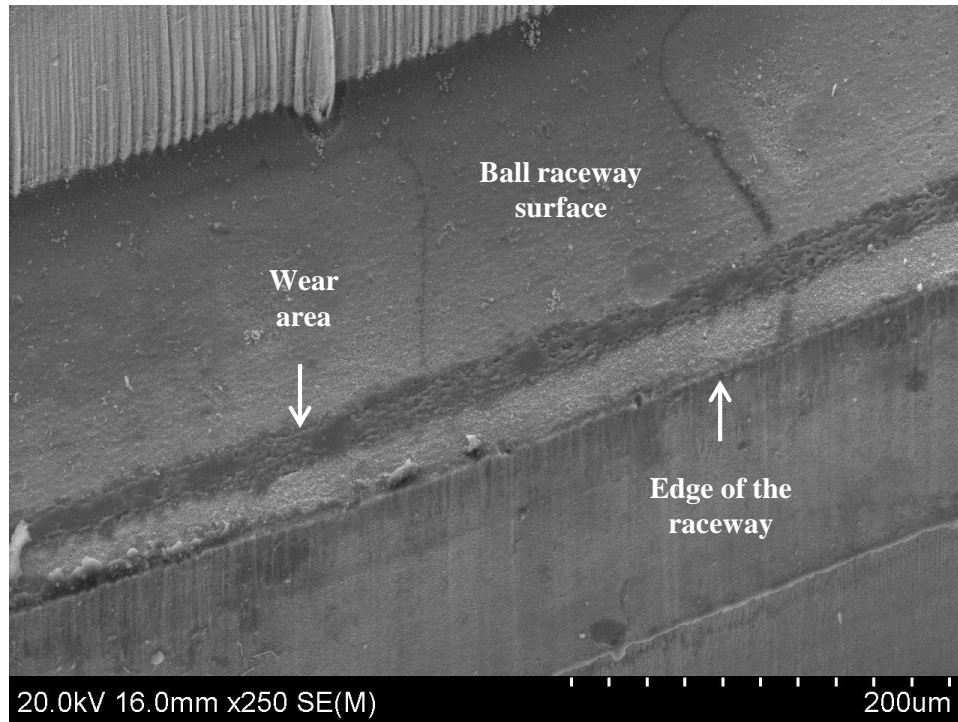
Figure 4.28. An SEM image of the ball raceway.

Figures 4.27 and 4.28 show a wear area of 130nm in depth and 13µm in width in the rectangular ball raceways after an operation of roughly half an hour at speeds between 5-23krpm. The wear values observed in the current bearings can be reduced by altering the geometry of the raceways from rectangular to circular through isotropic etching of the microball trenches. This will increase the ball-to-trench contact area and decrease the pressure on the contact interface that leads to less wear on both surfaces. In addition, increasing the diameter of the microballs may also decrease the wear due to increased contact surface, and is currently being investigated at MSAL. These improvements in the raceway to decrease the wear will enhance the tribological characteristics and increase the lifetime of the micro-turbo-generator.

Fabrication challenges were specifically a substantial drawback for the micromanufacturing of stators. The problems and restrictions discussed in Chapter 3 mandated the fabrication of backside connections by sputtered thin metal lines. As a result, the total phase resistance became two orders of magnitude higher than originally designed, which was reflected on the output power by a same magnitude reduction. In parallel, issues with the dielectric layer below backside connection lines resulted in disconnected backside connections. Therefore, all three phases could not be perfectly fabricated in one device. The thermal issues also prohibited the fabrication of stator alignment ball pits for a precise air gap definition between the rotor and the stator. This led to the variable and large air gaps that were defined by \ the packaging screws torque, and hence how much the O-ring between the two components were pressed. Large air gaps resulted in less magnetic flux linkage to the stator that decreased output power. These problems associated with the device fabrication can be solved by using a better dielectric layer on the stator backside, and wet etching of stator ball pits on the top side. This, however, requires extensive material characterization and fabrication process development.

Main contributors to the power losses are friction, eddy currents in the winding, and winding power loss which is equal to the generated electrical power at matched load condition, as described above. The rough calculations explained previously show that only 6% of the input mechanical power is converted to rotational energy, and that most of this energy is dissipated against friction in the ball raceway. This was expected as the surface-to-surface interactions in the form of friction become more dominant with device miniaturization due to the high surface-

to-volume ratio of MEMS devices. As a direct result, the final efficiency of the micro-turbo-generator was calculated to be on the order of $\sim 10^{-5}$. Since no permendur was utilized as a back iron on the backside of the stator, the device did not suffer from hysteresis and eddy current loss in this component.

5. Conclusion and Future Work

5.1. Summary

The successful development of the first integrated electromagnetic micro-turbo-generator supported on encapsulated microball bearings was demonstrated for power generation applications in small scale. Future generations of this device can potentially be coupled to a same-scale combustion engine to convert high-density hydrocarbon energy into electricity, which would allow for the realization of a miniature power source with power and energy densities surpassing that of battery technology. The micro-turbo-generator is comprised of a three-phase stator with three-dimensional copper coils and a microball bearing-supported rotor with integrated magnetic materials and a pneumatic actuation mechanism. Using these components, the device is capable of converting pressurized gas flow into electrical power. The device presents a novel combination of three key technologies and components to maximize output power, namely encapsulated microball bearings, high-flux thick magnetic materials, and wafer-thick stator coils. Integration of microball bearings allows for simple, robust, and stable device operation at high speeds on the order of tens of krpm and requires a simple fabrication process. The use of thick magnetic materials to increase the output power was also possible by the given stability and robustness of the microball bearings. Wafer-thick coil structures optimize the rotor-to-stator magnetic flux linkage, and decrease the internal impedance of the device which are crucial aspects in improving the output power.

The theory of device operation was explained using Faraday's law of electromagnetic induction. Based on this physical law, open circuit voltage of the

micro-turbo-generator was derived and the magnetic flux density within the stator was analyzed through finite element simulations. In addition, important device performance parameters such as coil resistance, inductance, armature reaction, power losses, efficiency, and normal force were investigated. The design initially utilized a permendur back iron in the stator to increase the magnetic flux density within the device. However, high normal force between the rotor and the stator that would lead to excessive wear in the microball bearings prohibited the use of stator back iron in this first device development, and therefore excluded from the design. Nevertheless, stator design was made and optimized based on the future integration of this component for a higher generated power. Considering the theoretical analysis and fabrication limitations, optimum designs that would result in maximum power and minimum power loss were found to be 8 pole 4 turns per pole, 10 pole 3 turns per pole, and 12 pole 3 turns per pole. In addition to these designs, a fabrication-wise safe and risky designs of 10 pole 2 turns per pole and 12 pole 1 turn were included the design set, respectively.

Device microfabrication was one of the most challenging aspects of this work due to the complicated device geometry and the large number of different components and device layers. Initially, the fabrication process was designed to use a total of 20 optical masks. During the course of device development, simplifications in the device structure were made in order to demonstrate the first working device. Finally, a total of 15 optical masks and 110 process steps were utilized to fabricate the micro-turbo-generator. To make the fabrication possible, a novel technique for the bottom up electroplating process was developed, eliminating the need for abrasive

polishing steps on one side of a silicon wafer after through-hole metal plating. This technique was applied on stators to realize wafer-thick copper coils integrated in silicon substrates and to reduce the impedance of the stator phases. While more than 80% of the stator coils were integrated in silicon, the remainder connections were fabricated on the stator backside over a dielectric layer deposited on the bottom of the silicon substrates. A number of dielectric layers were used and KMPR1050 was determined to suit best for the micro-turbo-generator. Further electroplating to decrease the backside connection resistance could not be performed due to the electrical shorting of the connections during this process. Therefore, backside connections contribute to more than 99% of the phase resistance. Once these backside connections are electroplated in dielectric layers, phase impedances lower than that presented in [69-93] will be achievable. Rotor fabrication was based on the microturbines previously demonstrated at MSAL with a number of modifications. One of the problems in rotor fabrication was observed to be the failure in the eutectic bonding holding the two rotor wafers together. This was attributed to possible tooling problems, material contamination, oxidation, and incorrect material composition. Finally, two stators with 10 pole 2 turns per pole and 10 pole 3 turns per pole designs, each with one operational phase, along with two 10 pole rotors were fabricated.

The successfully fabricated micro-turbo-generators were tested for mechanical and electrical performance. Initially, a plastic packaging and a test setup were designed and built. Tests to extract the phase electrical parameters showed that the phase impedances were purely resistive with values of 46Ω and 220Ω for the 10 pole 2 turns per pole and 10 pole 3 turns per pole stators, respectively. Spin-down tests

demonstrated a net friction torque between 5.5μNm-33μNm over a speed range of 0krpm-16krpm. This corresponds to a frictional power loss of 50mW at 16krpm. Maximum per-phase peak sinusoidal open circuit voltages of 0.06V and 0.1V, and maximum delivered powers of 10μW and 5.6μW over a speed range of 0-23krpm were measured that correspond to power densities of 59μW/cm^3 and 33μW/cm^3 for the two stator designs, respectively. These experimental results were shown to be in well agreement with the theoretical estimations that are based on mathematical analysis and finite element simulations. While the efficiency of 10 pole 2 turns per pole device was calculated to be 6×10^{-5}, an efficiency of 3×10^{-6} was found for the 10 pole 3 turns per pole device. The rotor failures at high speeds were observed to be due to the failure in the eutectic bond between the two rotor wafers and not the speed stability limit. The power values are lower compared to the previously demonstrated devices in [69-93] mainly due to low achieved speeds, high resistance of backside coil connections, and large stator-to-rotor air gap that are direct results of packaging issues, rotor bonding failures, and previously discussed fabrication challenges. However, this micro-turbo-generator provides a design platform for further improvement in the device design and fabrication that will lead to higher output power. Well agreement of the experimental results and theoretical estimations suggest that milliwatt to watt-level power is possible at high speeds and low phase impedances on the order of 100krpm and <1Ω, respectively, which are within the achievable design range of this device.

5.2. Summary of Accomplishments and Contributions

The first integrated electromagnetic micro-turbo-generator supported on encapsulated microball bearings was demonstrated in this dissertation. The major accomplishments and contributions of this work are summarized as follows:

Development of an electromagnetic micro-turbo-generator supported on microball bearings:

- Demonstrated the first electromagnetic micro-turbo-generator with simple and robust encapsulated microball bearings, wafer-thick stator coils and magnetic materials.

- Modeled and optimized the device design through theoretical analysis and finite element simulations.

- Developed a long and complex fabrication process with 15 optical masks and 110 process steps.

- Integrated permanent magnets and a soft magnetic material into a ball bearing-supported silicon microturbine.

- Performed a study to for measuring the vertical strength in eutectic bonds utilizing AuSn (74/26) as the adhesive metal layer.

- Designed and built a comprehensive test platform to measure the electrical and mechanical performance of the micro-turbo-generator.

- Demonstrated a maximum AC peak voltage and power of 0.1V and 10µW over a rotational speed range of 0-23krpm.

Wafer-thick three-dimensional stator coils:

- Designed and fabricated a three-dimensional wafer-thick stator coil structure integrated in a silicon substrate for low phase impedance.

- Optimized the thickness for maximum flux linkage from the rotor to the stator.

A novel fabrication technique for through-hole electroplating of metals with planar surfaces:

- Developed a novel technique for through-hole metal electroplating that involves a unique seed wafer detachment process and eliminates the need for abrasive polishing steps on one side of the wafer.

- Demonstrated a planar surface topography with protrusions on the order of 3µm on a silicon wafer with through-hole electroplated copper structures.

5.3. Future Work and Outlook

The following sections discuss possible device improvements for a higher performance in future device generations and potential uses of this technology in other applications based on the capabilities of the micro-turbo-generator.

5.3.1. Design and Fabrication Improvements

The microfabrication of the micro-turbo-generator was one of the main challenges in this work due to the large number of masks and process steps used to integrate all the components and device layers, as described previously. To

demonstrate the first working device, which was the focus of this dissertation, a number of simplifications were made in the design and fabrication at the expense of lower performance. The future generations of the micro-turbo-generator can be developed by building upon this work, and addressing the design and fabrication bottlenecks to improve the mechanical and electrical performance.

Due to the very low (~0.2µm) thickness of the backside connection layer, more than 99% of the phase resistance comes from this part of the stator winding. The future designs can include a chemically robust polymer mold on the back side of the stator that will allow for the electroplating of backside connections in this mold to a thickness of larger than 20µm. This will lead to two orders of magnitude decrease in the phase resistance and the same magnitude increase in maximum per-phase power. In addition, the use of such a mold will also result in reliable fabrication of all three stator phases, and hence, three phase power generation. Another factor that would improve the output power is defining a low and controlled air gap between the rotor and the stator for a higher magnetic flux density. The fabrication process can be altered to include wet etching of stator alignment ball pits instead of dry etching to eliminate the thermally-induced stress, and create a well-defined low air gap to maximize the magnetic flux within the stator. Furthermore, the magnetic flux can be improved by using a soft magnetic back iron on the back side of the stator. This will be only possible by improvements in the bearing geometry and by using a thrust pressure on the bottom side of the rotor to decrease the normal load on the microball bearings. Finally, the eutectic metal deposition and bonding of the rotors one at a time

along with using more reliable fabrication equipment will enhance the yield in rotor fabrication, and therefore will enable higher rotational speeds and power.

Once these improvements are made, a circuit with a three phase diode bridge rectifier and transformers can be used to perform AC to DC conversion and generate DC power. This circuit can be coupled with impedance matching networks to deliver power to electrical systems with a spectrum of different impedance characteristics.

5.3.2. Integration with a Micro Combustion Engine

Further integration of this micro-turbo-generator with a MEMS scale combustion engine will enable the conversion of high-density hydrocarbon energy into electricity. Once such a system with a >2% efficiency is realized, the energy density of current battery technology can be surpassed and batteries can be replaced in a variety of applications including micro air vehicles and portable military devices. A fully operational micro combustion engine is yet to be demonstrated, and significant research efforts are focused on the development of this component. In parallel, conventionally manufactured cm-size engines are available. The integration of the micro-turbo-generator presented in this work to either of these devices requires a systems design approach to address challenges such as heat management, durability to normal and tangential loads, and possible raceway wear.

5.3.3. Gas Flow Harvesting

The turbine structures, pneumatic actuation mechanism, and simple and robust bearing design of the micro-turbo-generator allows for the use of this device for

harvesting power from any type of gas flow that can spin the rotor component. One such application can be generating electrical power from human breathing to recharge the batteries of portable electronic systems. The MEMS scale of the micro-turbo-generator enables the integration of this device to electronic systems like cell phones and music players. Through optimizations in the coil design and turbine geometry that will allow for higher speeds at low flow rates, the future generations of the micro-turbo-generator can recharge the batteries of such systems when the user breaths through an apparatus fixed to the electronic device. Accordingly, the carbon dioxide flow would be harvested to generate electrical power to extend the operation time of these electronic systems. However, a filtering mechanism should also be designed and incorporated to prevent the particles that can affect the micro-turbo-generator operation.

5.3.4. Micromotor Applications

The micro-turbo-generator can also be used as a micromotor by applying three-phase current to the three-phase coils. Operation of this device in motoring mode will enable the development of high performance electrically-driven micro-turbo-pumps for microscale fluid delivery and rotary micropositioners.

6. References

[1]   M. Yoshio, R.J. Brodd, A. Kozowa, "Lithium-Ion Batteries", Springer, January 8, 2009, ISBN-10: 0387344446.

[2] http://en.wikipedia.org/wiki/File:Energy_density.svg

[3]   http://www.hypertextbook.com/facts/2003/EvelynGofman :Energy density of aviation fuel

[4]   http://www.mh-aerotools.de/airfoils/cox_frameset.htm

[5]   A. H. Epstein and S. D. Senturia, "Macro power from micro machinery," *Science*, vol. 276, p. 1211, May 1997.

[6]   A. H. Epstein, "Millimeter-scale, MEMS gas turbine engines," *ASME Journal of Engineering for Gas Turbines and Power*, vol. 126, pp. 205–226, Apr. 2004.

[7]   D. P. Arnold, "Review of microscale magnetic power generation," *IEEE Transactions on Magnetics,* vol. 43, no. 11, pp. 3940-3951, November 2007.

[8]   C. M. Waits, "Microburbopump utilizing microball bearings," *PhD thesis*, University of Maryland, College Park, ECE, 2008.

[9]   K. A. Cook-Chennault, N. Thambi, and A. M. Sastry, "Powering MEMS portable devices – a review of non-regenerative and regenerative power supply systems with special emphasis on piezoelectric energy harvesting systems," *Smart Materials and Structures,* vol. 17, pp. 1-33, 2008.

[10] J. B. Lee, Z. Z. Chen, M. G. Allen, A. Rohatgi, and R. Arya, "A miniaturized high-voltage solar-cell array as an electrostatic mems power-supply," *Journal of Microelectromechanical Systems,* vol. 4, pp. 102-108, 1995.

[11] A. Kribus, "Thermal integral micro-generation systems for solar and conventional use," *Transactions on ASME Journal of Solar Energy,* vol. 124, pp. 189-197, 2002.

[12] S. Bermejo, P. Ortega, J. J. Jimenez, and L. Castaner, "Response of c-Si PV arrays under monochromatic light for MEMS power supply," *Journal of Micromechanics and Microengineering,* vol. 15, pp. 1446-1453, 2005.

[13] S. Roundy, "On the effectiveness of vibration-based energy harvesting," *Journal of Intelligent Material Systems and Structure,* vol. 16, pp. 809-823, 2005.

[14] S. Roundy, P. K. Wright, and J. Rabaey, "A study of low level vibrations as a power source for wireless sensor nodes," *Computer Communications,* vol. 26, pp. 1131-1144, 2003.

[15] S. Roundy, P. K. Wright, "A piezoelectric vibration based generator for wireless electronics," *Smart Materials and Structures,* vol. 13, pp. 1131-1142, 2004.

[16] H. A. Sodano, D. J. Inman, and G. Park, "Comparison of piezoelectric energy harvesting devices for recharging batteries," *Journal of Intelligent Material Systems and Structures,* vol. 16, pp. 799-807, 2005.

[17] S. P. Beeby, R. N. Torah, M. J. Tudor, P. Glynne-Jones, T. O'Donnell, C. R. Saha, and S. Roy, "A micro electromagnetic generator for vibration energy harvesting," *Journal of Micromechanics and Microengineering,* vol. 17, pp. 1257-1265, 2007.

[18] R. Funahashi, M. Mikami, T. Mihara, S. Urata, and N. Ando, "A portable thermoelectric-power-generating module composed of oxide devices," *Journal of Applied Physics,* vol. 99, 066117, 2006.

[19] S. R. Brown, S. M. Kauzlarich, F. Gascoin, and G. J. Snyder, "$Yb_{14}MnSb_{11}$: new high efficiency thermoelectric material for power generation," *Chemistry of Materials,* vol. 18, pp. 1873-1877, 2006.

[20] D. Berardan, E. Alleno, C. Godart, M. Puyet, B. Lenoir, R. Lackner, E. Bauer, L. Girard, and D. Ravot, "Improved thermoelectric properties in double-filled $Ce_y/2Yb_{y/2}Fe_{4-x}(Co/Ni)_xSb_{-12}$ skutterudites," *Journal of Applied Physics,* vol. 98, 033710, 2005.

[21] H. Beyer, J. Nurnus, H. Bottner, A. Lambrecht, T. Roch, and G. Bauer, "PbTe based supperlatice structures with high thermoelectric efficiency," *Applied Physics Letters,* vol. 80, pp. 1216-1218, 2002.

[22] J. C. Chen, Z. J. Yan, and L. Q. Wu, "The influence of Thomson effect on the maximum power output and maximum efficiency of a thermoelectric generator," *Journal of Applied Physics,* vol. 79, pp. 8823-8828, 1996.

[23] S. W. Kim, Y. Kimura, and Y. Mishima, "Enhancement of high temperature thermoelectric properties of intermetallic compounds based on a skutterudite $IrSb_3$ and a half-Heusler TiNiSb," *Science and Technology of Advanced Materials,* vol. 5, pp. 485-489, 2004.

[24] R. Venkatasubrahmanian, E. Siivola, T. Colpitts, and B. O'Quinn, "Thin-film thermoelectric devices with high room-temperature figures of merit," *Nature,* vol. 413, pp. 597-602, 2001.

[25] X. C. Xuan, "Optimum design of a thermoelectric device," *Semiconductor Science and Technology,* vol. 17, pp. 114-119, 2002.

[26] K. Kurosaki, A. Kosuga, H. Muta, M. Uno, and S. Yamanaka, "Ag_9TlTe_5: a high-performance thermoelectric bulk material with extremely low thermal conductivity," *Applied Physics Letters,* vol. 87, pp. 3, 2005.

[27] T. Christen, and M. W. Carlen, "Theory of Ragone plots," *Journal of Power Sources,* vol. 91, pp. 210-216, 2000.

[28] W. G. Pell, and B. E. Conway, "Quantitative modeling of factors determining Ragone plots for batteries and electrochemical capacitors," *Journal of Power Sources,* vol. 63, pp. 255-266, 1996.

[29] H. A. Kiehn, "Battery Technology Handbook," 2nd edition (New York: Dekker) 2003.

[30] P. Albertus, J. Christensen, and J. Newman, "Modeling side reactions and nonisothermal effects in nickel metal-hydride batteries," *Journal of Electrochemical Society,* vol. 155 A, pp. 48-60, 2008.

[31] D. H. Doughty, "Materials issues in lithium ion rechargeable battery technology, "*Journal of Power Sources,* vol. 32, pp. 75-81, 1996.

[32] H. Karami, M. Shamsipur, S. Ghasemi, and M. F. Mousavi, "Lead-acid bipolar battery assembled with primary chemically formed positive pasted electrode," *Journal of Power Sources,* vol. 164, pp. 896-904, 2007.

[33] D. L. Reddy a T. B., "Handbook of batteries," 3rd edition, (New York: McGraw-Hill) 2002.

[34] K. Gerasopoulos, X. Chen, J. N. Culver, C. Wang, and R. Ghodssi, "Self-assembled Ni/TiO$_2$ nanocomposite anodes synthesized via electroless plating and atomic layer deposition on biological scaffolds," *Chemical Communications,* vol. 46, pp. 7349-7351, August 2010.

[35] X. Chen, K. Gerasopoulos, J. Chuo, A. Brown, C. Wang, R. Ghodssi, and J. Culver, "Virus-enabled silicon anode for lithium-ion batteries," *ACS Nano,* vol. 4, no. 9, pp. 5366-5372, August 2010.

[36] K. Gerasopoulos, M. McCarthy, P. Banerjee, X. Fan, J. N. Culver, and R. Ghodssi, "Biofabrication methods for the patterned assembly and synthesis of viral nanotemplates," *Nanotechnology,* vol. 21, pp. 1-11, January 2010.

[37] K. Gerasopoulos, M. McCarthy, E. Royston, J. N. Culver, and R. Ghodssi, "Nanostructured nickel electrodes using the tobacco mosaic virus for microbattery applications," *Journal of Micromechanics and Microengineering,* vol. 18, no. 10, pp. 1-8, September 2008.

[38] J. D. Morse, "Micro-fuel cell power sources." *International Journal of Energy Research,* vol. 31, pp. 576-602, 2007.

[39] G. Q. Lu and C. Y. Wang, "Development of micro direct methanol fuel cells for high power applications," *Journal of Power Sources,* vol. 144, pp. 141-145, 2005.

[40] N. T. Nguyen and S. H. Chan, "Micromachined polymer electrolyte membrane and direct methanol fuel cells – a review," *Journal of Micromechanics and Microengineering,* vol. 16, pp. 1-12, 2006.

[41] K. B. Min, S. Tanaka, and M. Esashi, "Fabrication of novel MEMS-based polymer electrolyte fuel cell architectures with catalytic electrodes supported on porous SiO_2," *Journal of Micromechanics and Microengineering,* vol. 16, pp. 505-511, 2006.

[42] R. Hahn, S. Wagner, A. Schmitz, and H. Reichl, "Development of a planar micro fuel cell with thin film and micro patterning technologies," *Journal of Power Sources,* vol. 131, pp. 73-78, 2004.

[43] H. Y. Cha, H. G. Choi, J. D. Nam, Y. Lee, S. M. Cho, E. S. Lee, J. K. Lee, and C. H. Chung, "Fabrication of all-polymer micro-DMFCs using UV-sensitive photoresist," *Electrochimica Acta,* vol. 50, pp. 795-799, 2004.

[44] S. Aravamudhan, A. R. A. Rahman, and S. Bhansali, "Porous silicon based orientation independent, self-priming micro direct ethanol fuel cell," *Sensors and Actuators A,* vol. 123/124, pp. 497-504, 2005.

[45] C. Y. Lee, G. W. Wu, and C. L. Hsieh, "In situ diagnosis of micrometallic proton exchange membrane fuel cells using microsensors," *Journal of Power Sources,* vol. 172, pp. 363-367, 2007.

[46] J. S. Lee, M. Y. Lee, C. Y. Lee, J. J. Lai, F. H. Kuan, and C. W. Chuang, "The performance of miniature metallic PEM fuel cells," *Journal of Power Sources,* vol. 171, pp. 148-154, 2007.

[47] B. E. Buergler, M. Ochsner, S. Vuillemin, and L. J. Gauckler, "From macro- to micro-single chamber solid oxide fuel cells," *Journal of Power Sources,* vol. 171, pp. 310-320, 2007.

[48] S. K. Chou, W. M. Yang, K. J. Chua, J. Li, K. L. Zhang, "Development f micro power generators – a review," *Journal of Applied Energy,* vol. 88, pp. 1-16, 2011.

[49] N. I. Kim, S. Kato, T. Kataoka, T. Yokomori, S. Maruyama, T. Fujimori, "Flame stabilization and emission of small Swiss-roll combustors as heaters," *Combustion Flame,* vol. 141, pp. 229-240, 2005.

[50] T. Okamasa, G. G. Lee, Y. Suziki, N. Kasagi, S. Matsuda, "Development of a micro catalytic combustor using high-precision ceramic tape casting," *Journal of Micromechanics and Microengineering,* vol. 16, pp. 198-205, 2006.

[51] W. G. Bessler, C. Schulz, "Quantitative multi-line NO-LIF temperature imaging," *Applied Physics B,* vol. 78, pp. 519-533, 2004.

[52] T. H. Lee, G. B. Wolfgang, K. Helmut, S. Christof, B. J. Jay, "Quantitative temperature measurements in high-pressure flames with multiline No-LIF thermometry," *Applied Optics,* vol. 44, pp. 6718-6728, 2005.

[53] V. V. Zamaschikov, "Experimental investigation of gas combustion regimes in narrow tubes," *Combustion Flames,* vol. 108, pp. 357-359, 1997.

[54] J. Peirs, D. Reynaerts, and F. Verplaetsen, "A microturbine for electric power generation," *Sensors and Actuators A,* vol. 113, pp. 86-93, 2004.

[55] I. A. Waitz, G. Gauba, and Y. S. Tzeng, "Combustors for micro-gas turbine engines," *Transactions on ASME Journal of Fluids Engineering,* vol. 120, pp. 109-117, 1998.

[56] T. L.L Marbach, and A. K. Agrawal, "Heat-recirculating combustor using porous inert media for mesoscale applications," *Journal of Propulsion and Power,* vol. 22, pp. 145-150, 2006.

[57] S. Tanaka, T. Yamada, S. Sugimoto, J. F. Li, and M. Esashi, "Silicon nitride ceramic-based two-dimensional microcombustor," *Journal of Micromechanics and Microengineering,* vol. 13, pp. 502-508, 2003.

[58] W. M. Yang, S. K. Chou, C. Shu, H. Xue, Z. W. Li, D. T. Li, and J. F. Pan, "Microscale combustion research for application to micro thermophotovoltaic systems," *Energy Conversion and Management,* vol. 44, pp. 2625-2634, 2003.

[59] Z. W. Li, S. K. Chou, C. Shu, and W. M. Yang, "Effects of step height on wall temperature of a microcombustor," *Journal of Micromechanics and Microengineering,* vol. 15, pp. 207-212, 2005.

[60] W. M. Yang, S. K. Chou, C. Shu, Z. W. Li, and H. Xue, "A prototype microthermophotovoltaic power generator," *Applied Physics Letters,* vol. 84, pp. 3864-3866, 2004.

[61] W. M. Yang, S. K. Chou, C. Shu, Z. W. Li, and H. Xue, "Development of microthermophotovoltaic system," *Applied Physics Letters,* vol. 81, pp. 5255-5257, 2002.

[62] W. M. Yang, S. K. Chou, C. Shu, H. Xue, and Z. W. Li, "Design, fabrication, and testing of a prototype microthermophotovoltaic system," *Journal of Microelectromechanical Systems,* vol. 13, pp. 851-856, 2004.

[63] W. S. N. Trimmer, "Microrobots and micromechanical systems," *Sens. Actuators*, vol. 19, pp. 267–287, 1989.

[64] I. J. Busch-Vishniac, "The case for magnetically-driven micro-actuators," *Sens. Actuators*, vol. A33, pp. 207–220, 1992.

[65] J. W. Judy, "Microelectromechanical systems (MEMS): Fabrication, design and applications," *Smart Mater. Struct.*, vol. 10, pp. 1115–1134, 2001.

[66] O. Cugat, J. Delamare, and G. Reyne, "Magnetic micro-actuators and systems (MAGMAS)," *IEEE Trans. Magn.*, vol. 39, no. 6, pp. 3607–3612, Nov. 2003.

[67] T. G. Wiegele, "Micro-turbo-generator design and fabrication: A preliminary study," *in Proc. 31st Intersociety Energy Conversion Engineering Conf. (IECEM'96)*, Aug. 1996, pp. 2308–2313.

[68] A. Holmes, G. Hong, K. Pullen, and K. Buffard, "Axial-flow microturbine with electromagnetic generator: design, cfd simulation, and prototype demonstration," *17th IEEE International Conference on Micro Electro Mechanical Systems (MEMS 2004)*, pp. 568–571, 2004.

[69] A. S. Holmes, G. Hong, and K. R. Pullen, "Axial-flux permanent magnet machines for micropower generation," *J. Microelectromech. Syst.*, vol. 14, no. 1, pp. 54–62, Feb. 2005.

[70] C. T. Pan and T. T. Wu, "Development of a rotary electromagnetic microgenerator," *J. Micromech. Microeng.*, vol. 17, no. 1, pp. 120–128, Jan. 2007.

[71] C. T. Pan and T. T. Wu, "Simulation and fabrication of magnetic rotary microgenerator with multipolar NdFeB magnet," *Microelectronics Reliability*, vol. 47, pp. 2129–2134, Dec. 2007.

[72] C. T. Pan and Y. J. Chen, "Application of low temperature co-fire ceramics on in-plane micro-generator," *Sensors and Actuators A: Physical*, vol. 144, pp. 144– 153, May 2008.

[73] H. Raisigel, Micro-G´en´erateur Magn´etique Planaire et Micro-Converteur Int´egr´e. *PhD thesis*, Laboratoire d'Electrotechnique de Grenoble, France, 2006.

[74] H. Raisigel, O. Cugat, and J. Delamare, "Permanent magnet planar microgenerators," *Sensor and Actuators A: Physical*, vol. 130, pp. 438–444, Aug. 2006.

[75] S. Das, Magnetic Machines and Power Electronics for Power MEMS Applications. *PhD thesis*, Massachusetts Institute of Technology, EECS, 2005.

[76] S. Das, D. P. Arnold, I. Zana, J.-W. Park, M. G. Allen, and J. H. Lang, "Microfabricated high-speed axial-flux multiwatt permanent-magnet generators – Part I: Modeling," *Journal of Microelectromechanical Systems*, vol. 15, pp. 1330–1350, Oct. 2006.

[77] D. P. Arnold, S. Das, J.-W. Park, I. Zana, J. H. Lang, and M. G. Allen, "Microfabricated high-speed axial-flux multiwatt permanent-magnet generators – Part II: Design, fabrication, and testing," *Journal of Microelectromechanical Systems*, vol. 15, pp. 1351–1363, Oct. 2006.

[78] D. P. Arnold, P. Galle, F. Herrault, S. Das, J. H. Lang, and M. G. Allen, "A selfcontained, flow-powered microgenerator system," *5th International Workshop on Micro and Nanotechnology for Power Generation and Energy Conversion Applications. PowerMEMS 2005*, pp. 113–115, Dec. 2005.

[79] S. Das, D. P. Arnold, I. Zana, J. W. Park, J. H. Lang, and M. G. Allen, "Multiwatt electric power from a microfabricated permanent-magnet generator," *18th IEEE International Conference on Micro Electro Mechanical Systems. MEMS 2005*, pp. 287–290, Jan. 2005.

[80] D. P. Arnold, Magnetic Machines for Microengine Power Generation. PhD thesis, Georgia Institute of Technology, ECE, 2004.

[81] I. Zana, F. Herrault, D. P. Arnold, and M. G. Allen, "Magnetic patterning of permanent-magnet rotors for microscale motor/generators," *5th International Workshop on Micro and Nanotechnology for Power Generation and Energy Con- version Applications. PowerMEMS 2005,* pp. 116–119, Dec. 2005.

[82] D. P. Arnold, Y.-H. Joung, I. Zana, J.-W. Park, D. S., J. H. Lang, V. D., and M. G. Allen, "High-speed characterization and mechanical modeling of microscale, axial-flux, permanent-magnet generators," *The 13th International Con- ference on Solid-State Sensors, Actuators and Microsystems. TRANSDUCERS 2005*, pp. 701–704, June 2005.

[83] D. P. Arnold, F. Herrault, I. Zana, P. Galle, J.-W. Park, S. Das, J. H. Lang, and M. G. Allen, "Design optimization of an 8 W, microscale, axial-flux, permanentmagnet generator," Journal *of Micromechanics and Microengineering*, vol. 16, pp. S290–S296, Sep. 2006.

[84] F. Herrault, D. P. Arnold, I. Zana, P. Galle, and M. G. Allen, "High temperature operation of multi-watt, axial-flux, permanent-magnet generators," *Sensors and Actuators A: Physical*, vol. 148, no. 1, pp. 299-305, Nov. 2008.

[85] F. Herrault, D. P. Arnold, I. Zana, P. Galle, and M. G. Allen, "Multi-watt, microscale, axial-flux, permanent-magnet generators operating at high temperatures," *IEEE International Magnetic Conferences (Intermag 2006),* San Diego, CA, May 2006. p. 597.

[86] B. C. Yen, A Fully-Integrated Multi-Watt Permanent-Magnet Turbine Generator. *PhD thesis*, Massachusetts Institute of Technology, EECS, 2008.

[87] B. C. Yen, F. Herrault, K. J. Hillman, M. G. Allen, F. F. Ehrich, S. Jacobson, C.-H. Ji, J. H. Lang, H. Li, Z. S. Spakovszky, and D. R. Veazie, "Characterization of a fully-integrated permanent-magnet turbine generator," *in Proc. 8th int. Workshop Micro Nanotechnology For Power Generation and Energy Conversion Apps. (PowerMEMS 2008),* pp. 121-124, Nov. 2008.

[88] F. Herrault, C.-H. Ji, and M. G. Allen, "Ultraminiaturized, high-speed, permanent magnet generators for milliwatt-level power generation," Journal of Microelectromechanical Systems, vol. 17, no. 6, pp. 1376-1387, Dec. 2008.

[89] F. Herrault, T. Crittenden, S. Yorish, E. Birdsell, A. Glezer, and M. G. Allen, "A self-resonant, MEMS-fabricated, air-breathing engine," *Tech. Dig. Solid-State Sensor, Actuator, and Microsystems Workshop (Hilton Head 2008)*, pp. 348-351, June 2008.

[90] F. Herrault, C.-H. Ji, S.-H. Kim, X. Wu, and M. G. Allen, "A microfluidic-electric package for Power MEMS generators," *Tech. Dig. 21st IEEE int. Conf. Micro Electro Mechanical Systems (MEMS 2008),* pp.112-115, Tucson, USA, Jan. 2008.

[91] F. Herrault, C.-H. Ji, R. H. Shafer, S.-H. Kim, and M. G. Allen "Ultraminiaturized milliwatt-scale permanent magnet generators," *in Proc. Transducers 2007: The 14th International Conference on Solid-State Sensors, Actuators and Microsystems*, pp.899-902, Lyon, France, June 2007.

[92] F. Herrault, C. H. Ji, S. H. Kim, X. Wu, and M. G. Allen, "A Microfluidic-Electric Package for Power MEMS Generators," *Proceedings of the 21st IEEE International Conference on Micro Electro Mechanical Systems (MEMS 2009)*, pp. 112-115, Tucson, AZ, USA, January 13-17, 2008.

[93] F. Herrault, B. C. Yen, C. H. Ji, Z. S. Spakovszky, J. H. Lang, and M. G. Allen, "Fabrication and Performance of Silicon-Embedded Permanent-Magnet Microgenerators," *Journal of Microelectromechanical Systems,* vol. 19, no. 1, pp. 4-13, February 2010.

[94] A. P. Camacho, W. G. Gardner, I. Wang, H. S. Shen, J. W. Jaworski, C. K. Gilmore, S. O. Pelekies, J. A. Dunnmon, and J. M. Protz, "Experimental Results of An Ejector Driven Micro Turbine Generator," *Proceedings of the 10th International Workshop on Micro and Nanotechnology for Power Generation and Energy Conversion Applications (Power MEMS '10)*, pp. 95-98, Leuven, Belgium, November 30 – December 3, 2010.

[95] O. Dessornes, and C. Zwyssig, "Micro-Generator for Ultra Gas Turbine," *Proceedings of the 10th International Workshop on Micro and Nanotechnology for Power Generation and Energy Conversion Applications (Power MEMS '10)*, pp. 195-198, Leuven, Belgium, November 30 – December 3, 2010.

[96] Ta-Wei Lin, "Modeling and Experimental Measurement of Dynamic Friction in MEMS-based Micro-ball Bearing," *Master's Thesis*, University of Maryland, December 2001.

[97] T-W. Lin, A. Modafe, B. Shapiro and R. Ghodssi, "Characterization of Dynamic Friction in MEMS-Based Micro-Ball Bearings," *IEEE Transactions on Instrumentation and Measurement*, vol. 53, no. 3, pp. 839-846, June 2004.

[98] X. Tan, A. Modafe, and R. Ghodssi, "Measurement and Modeling of Dynamic Rolling Friction in Linear Microball Bearings," *Journal of Dynamic Systems, Measurement, and Control*, vol. 128, pp. 891-898, December 2006.

[99] X. Tan, A. Modafe, and R. Ghodssi, "An Empirical Model for Dynamic Friction in Microfabricated Linear Microball Bearings," *The 24th American Control Conference (ACC 2005)*, pp. 2463-2468, Portland, OR, June 8-10, 2005.

[100] A. Modafe, "Benzocyclobutene-Based Electric Micromachines Supported on Microball Bearings: Design, Fabrication, and Characterization," *Ph.D. Thesis*, University of Maryland, College Park, MD, September 2007.

[101] A. Modafe, N. Ghalichechian, A. Frey, J. H. Lang, and R. Ghodssi, "Microball-bearing-supported electrostatic micromachines with polymer dielectric films for electromechanical power conversion," *Journal of Micromechanics and Microengineering (JMM)*, vol. 16, pp. S182-S190, September 2006.

[102] N. Ghalichechian, A. Modafe, J. H. Lang, and R. Ghodssi, "Dynamic characterization of a linear electrostatic micromotor supported on microball bearings," *Sensors and Actuators A: Physical*, vol. 136, no. 2, pp. 416-503, May 2007.

[103] A. Modafe, N. Ghalichechian, and R. Ghodssi, "BCB-Based Linear Micromotor Supported on Microball Bearings: Design Concepts, Characterization, and Fabrication Development, *American Vacuum Society 51st International Symposium* Anaheim, CA, November 14-19, 2004.

[104] A. Modafe, N. Ghalichechian, J. H. Lang, and R. Ghodssi, "A Microball-Bearing-Supported Linear Electrostatic Micromotor with Benzocyclobutene Polymer Insulating Layers," *The 13th International Conference on Solid-State Sensors, Actuators, and Microsystems (Transducers '05)*, pp. 693-696, Seoul, Korea, June 5-9, 2005.

[105] A. Modafe, N. Ghalichechian, A. Frey, J. H. Lang, and R. Ghodssi, "Microball-Bearing-Supported Electrostatic Micromachines with Polymer Dielectric Films for Electromechanical Power Conversion," *Fifth International Workshop on Micro Nano Technology for Power Generation and Energy Conversion Applications*, pp. 173-176, Tokyo, Japan, November 28-30, 2005.

[106] N. Ghalichechian, A. Modafe, A. Frey, J. H. Lang, and R. Ghodssi, "Dynamic Characterization of a Linear Variable-Capacitance Micromotor," *2006 Solid-State Sensor, Actuator, and Microsystems Workshop*, pp. 19-22, Hilton Head Island, June 4-8, 2006.

[107] M. I. Beyaz, "Closed-Loop Control of a Micropositioner Using Integrated Photodiode Sensors," *Master's Thesis*, University of Maryland, College Park, MD, August 2008.

[108] M. I. Beyaz, M. McCarthy, N. Ghalichechian, and R. Ghodssi, "Closed-Loop Control of a Long-Range Micropositioner Using Integrated Photodiode

Sensors," *Sensors and Actuators: A. Physical*, vol. 151, pp. 187-194, April 2009.

[109] M.I. Beyaz, M. McCarthy, N. Ghalichechian, and R. Ghodssi, "Photodiode Position Sensors for Integrated Feedback Control of a Long-Range Micropositioner", *Proceedings of the 2008 IEEE SENSORS Conference,* pp. 803-806, Lecce, Italy, October 26-29, 2008.

[110] M. I. Beyaz, N. Ghalichechian, and R. Ghodssi, "Toward an Autonomous Electrostatic Micromotor: Integrated Feedback Control", *Proceedings of the 21st IEEE International Conference on Micro Electro Mechanical Systems (MEMS 2008),* pp. 483-486, Tucson, AZ, USA, January 13-17, 2008.

[111] M. I. Beyaz, N. Ghalichechian, A. Modafe, and R. Ghodssi, "Towards Feedback Control with Integrated Position Sensing in Micromachines," *American Vacuum Society 54th International Symposium*, Seattle, WA, October 14 - 19, 2007.

[112] M. I. Beyaz, N. Ghalichechian, and R. Ghodssi, "Toward Smart Micromachines with Integrated Feedback Control," *International Semiconductor Device Research Symposium (ISRS 2007)*, College Park, MD, December 11 - 14, 2007.

[113] N. Ghalichechian, "Design, Fabrication, and Characterization of a Rotary Variable-Capacitance Micromotor Supported on Microball Bearings," *Ph.D. Thesis*, University of Maryland, College Park, MD, July, 2007.

[114] N. Ghalichechian, A. Modafe, M. Beyaz, and R. Ghodssi, "Design, Fabrication, and Characterization of a Rotary Micromotor Supported on Microball Bearings," *Journal of Microelectromechanical Systems (JMEMS)*, vol. 17, No. 3, pp. 632-642, June 2008.

[115] N. Ghalichechian, A. Modafe, M. I. Beyaz, C. M. Waits, and R. Ghodssi, "Design and Fabrication of a Rotary, Electrostatic Micromotor Supported on Microball Bearings," *Sixth International Workshop on Micro and Nanotechnology for Power Generation and Energy Conversion Applications (Power MEMS '06),* pp. 227-230, Berkeley, CA, USA, Nov 29-Dec 1, 2006.

[116] N. Ghalichechian, A. Modafe, M. I. Beyaz, and R. Ghodssi, "A Rotary Micromotor Supported on Microball Bearings," *The 14th International Conference on Solid-State Sensors, Actuators, and Microsystems (Transducers '07),* Lyon, France, June 10-14, 2007.

[117] N. Ghalichechian, M.McCarthy, M. I. Beyaz, R. Ghodssi, "Measurement and Modeling of Friction in Linear and Rotary Micromotors Supported on Microball Bearings," *Proceedings of the 21st IEEE International Conference on Micro Electro Mechanical Systems (MEMS 2008),* pp. 507-510, Tucson, AZ, USA, January 13-17, 2008.

[118] C.M. Waits, M. McCarthy, and R. Ghodssi, "A Microfabricated Spiral-Groove Turbopump Supported on Microball Bearings," *Journal of Microelectromechanical Systems (JMEMS),* vol. 19, no. 1, pp. 99-109, February 2010.

[119] C. M. Waits, B. Geil, and R. Ghodssi, "Encapsulated Ball Bearings for Rotary Micro Machines," *Journal of Micromechanics and Microengineering (JMM),* vol. 17, pp. S224-S229, August 2007.

[120] C. Mike Waits, M. McCarthy, and R. Ghodssi, "A MEMS Turbopump for Fuel Delivery in Small-scale Power Systems," *The 15th International Conference on*

Solid-State Sensors, Actuators, and Microsystems (Transducers '09), Denver, CO, June 21-25, 2009.

[121] C.M. Waits, N. Jankowski, B. Geil, and R. Ghodssi, "MEMS Rotary Actuator using an Integrated Ball Bearing and Air Turbine", *The 14th International Conference on Solid-State Sensors, and Microsystems (Transducers '07),* Lyon, France, June 10-14, 2007.

[122] M. McCarthy, C. M. Waits, and R. Ghodssi, "Dynamic Friction and Wear in a Planar-Contact Encapsulated Microball Bearing Using an Integrated Microturbine," *Journal of Microelectromechanical Systems (JMEMS)*, vol. 18, No. 2, pp. 263-273, April 2009.

[123] M. McCarthy, C.M. Waits, and R. Ghodssi, "Dynamic Friction and Microturbine Performance Using a Planar-Contact Encapsulated Microball Bearing", *Proceedings of the 2008 Solid-State Sensor, Actuator, and Microsystems Workshop*, Hilton Head Island, SC, June 1-5, 2008.

[124] B. Hanrahan, M. McCarthy, J. Balsam, C.M. Waits, H. Bruck, and R. Ghodssi, "Hard Film Coatings for High-Speed Rotary MEMS Supported on Microball Bearings," *Proceedings of the 9th International Workshop on Micro and Nanotechnology for Power Generation and Energy Conversion Applications (PowerMEMS 2009)*, pp. 589-592, Washington, DC, December 1-4, 2009.

[125] B. Hanrahan, M. Beyaz, M.McCarthy, C.M. Waits, and R. Ghodssi, "A New Performance Regime For Microfabricated Ball Bearings," *Proceedings of the 10th International Workshop on Micro and Nanotechnology for Power*

Generation and Energy Conversion Applications (PowerMEMS 2010), Leuven, Belgium, November 30 - December 3, 2010, pp. 191-194.

[126] M. McCarthy, C. M. Waits, M. I. Beyaz, and R. Ghodssi, "A rotary microactuator supported on encapsulated microball bearings using an electro-pneumatic thrust balance," *Journal of Micromechanics and Microengineering (JMM)*, vol. 19, issue 9, pp. 1-7, August 2009.

[127] M. McCarthy, C. M. Waits, M. I. Beyaz, and R. Ghodssi, "A Rotary Microactuator Supported on Encapsulated Microball Bearings Using an Electro-Pneumatic Thrust Balance," *Proceedings of the 22nd IEEE International Conference on Micro Electro Mechanical Systems (MEMS 2009),* pp. 1095-1098, Sorrento, Italy, January 15-29, 2009.

[128] M. McCarthy, M. I. Beyaz, C. M. Waits, and R. Ghodssi, "An Electro-Pneumatic Thrust Balance for Small-Scale Energy Conversion Using Encapsulated Rotary Microball Bearings," *Proceedings of the 8th International Workshop on Micro and Nanotechnology for Power Generation and Energy Conversion Applications (Power MEMS '08),* pp. 129-132, Sendai, Japan, November 9-12, 2008.

[129] A.E. Fitzgerald, C. Kingsley, S.D. Umans, " Electric Machinery," 3rd edition, ISBN:0-07-707708-3.

[130] X.F. Wang, Y. Song, M. Irving, "Power systems analysis," 1st edition, ISBN: 978-0387728520

[131] D. K. Cheng, "Fundamentals of Engineering Electromagnetics," ISBN: 0-201-56611-7.

[132] http://www.matweb.com/search/datasheet.aspx?matguid=a1a4325be7e14f35a49 4637090d6d3de&ckck=1

[133] http://services.eng.uts.edu.au/~venkat/pe_html/ch05s1/ch05s1p1.htm   (online power electronics text)

[134] G. Schweitzer, "Active magnetic bearings – chances and limitations," *6th International Conference on Rotor Dynamics*, 2002.

[135] http://www.edfagan.com/2006/products/soft-magnetic-alloys/magnetic-properties/

[136] P. Dixit, J. Miao, R. Preisser, "Fabrication of high aspect ratio 35μm pitch through wafer copper interconnects by electroplating for 3d wafer stacking," *Electrochemical and Solid State Letters*, 9 (10), G305-308, 2006.

[137] P. Dixit, J. Miao, "Aspect ratio dependent copper electrodeposition technique for very high aspect ratio through hole plating," *Journal of The Electrochemical Society*, 153 (6), G552-559, 2006.

[138] M.I. Beyaz, M. McCarthy, and R. Ghodssi, "Fabrication of High-Aspect Ratio Metal Structures with Planar Surfaces for Power MEMS Devices," *Proceedings of the 9th International Workshop on Micro and Nanotechnology for Power Generation and Energy Conversion Applications (PowerMEMS 2009)*, pp. 586-588, Washington, DC, December 1-4, 2009.

[139] S. M. Hu, "Critical Stress in Silicon Brittle Fracture, and Effect of Ion Implantation and Other Surface Treatments," *Journal of Applied Physics,* vol. 53, pp. 3576-3580, May 1982.

[140] M. Beyaz, B. Hanrahan, and R. Ghodssi, "A Microfabricated Rotor Supported On Microball Bearings With Integrated Permanent Magnets", *Proceedings of the 10th International Workshop on Micro and Nanotechnology for Power Generation and Energy Conversion Applications (PowerMEMS 2010)*, Leuven, Belgium, November 30 - December 3, 2010, pp. 167-171.

Appendix: Fabrication Recipes

Photolithography with Shipley 1813 (1.5μm)

- Adhesion promoter: HMDS (spin: 3000rpm for 30 seconds)

- Spin speed: 3000rpm, time: 30 seconds, open lid

- Softbake: 100ºC for 1 minute on hot plate

- Exposure dose: 180mJ/cm^2

- Developer: 352 for 1 minute

- Removal: Acetone - Methanol - Isopropyl Alcohol - Deionized Water

Photolithography with AZ9260 (~10μm) (Modified from Original for This Process)

- Adhesion promoter: HMDS (spin: 3000rpm for 30 seconds)

- Spin speed: 3 step process, closed lid

  - Step 1: Spin 1: 500rpm, Time 1: 10 seconds, Ramp 1: 1

  - Step 2: Spin 2: 2000rpm, Time 2: 60 seconds, Ramp 2: 1

  - Step 3: Spin 3: 3000rpm, Time 3: 2 seconds, Ramp 3: 1, Ramp down: 1

- Softbake: 2 step process on hot plate

  - Step 1: 65ºC for 5 minutes

  - Step 2: 100ºC ramping from 65ºC for 15 minutes

  - Cool down: 2 minutes on cold surface

- Exposure dose: 800mJ/cm^2

- Developer: 400K:Deionized water (1:4) for 5 minutes

- Removal: Acetone - Methanol - Isopropyl Alcohol - Deionized Water

- Alternative removal: Flood Exposure – Development – Deionized Water

Photolithography with KMPR1050 (~20μm) (Modified from Original for This Process)

- Adhesion promoter: HMDS (spin: 3000rpm for 30 seconds)

- Spin speed: 3 step process, open lid

    - Step 1: Spin 1: 500rpm, Time 1: 10 seconds, Ramp 1: 5

    - Step 2: Spin 2: 4000rpm, Time 2: 40 seconds, Ramp 2: 10

    - Step 3: Spin 3: 5000rpm, Time 3: 2 seconds, Ramp 3: 1, Ramp down: 1

- Softbake: 100ºC ramping from 65ºC for 30 minutes on hot plate

    - Cool down: on hot plate

- Exposure dose: 1500mJ/cm^2

- Post exposure bake: 100ºC ramping from 65ºC, 4 minutes at 100ºC

    - Cool down: on hot plate

- Developer: SU8 Developer for 3 minutes

Photolithography with Spray Coating (~10μm)

- Spray coating

- Softbake: 110ºC for 2 minutes

- Exposure dose: 800mJ/cm^2

- Developer: 300 MIF for 3 minutes

- Removal: Acetone - Methanol - Isopropyl Alcohol - Deionized Water

Deep Reactive Ion Etching

- Etch cycle:

  - Gases: SF6: 130sccm, O2: 13sccm

  - Power: Coil: 600W, Platen: 17W

  - Time: 10 seconds

- Passivation cycle:

  - Gases: C4F8: 85sccm

  - Power: Coil: 600W, Platen: 0W

  - Time: 6.5 seconds

Metal Sputtering (Au and Cu)

- DC Power: Two step DC sputtering

  - Step 1: DC Power 1: 50W, Time 1: 2 minutes for Au, 10 minutes for Cu

  - Step 2: DC Power 2: 200W, Time 2: 8 minutes for Au, 25 minutes for Cu

- Pressure: 5mTorr

Cu Electroplating

- DC Current Density: 50mA/cm^2

- Solution temperature: Room temperature

- Stirring speed: 200 rpm

- Anode – Cathode distance: ~ 3cm

Au Wet Etching

- Etchant: Transene Gold Etchant TFA

- Etch temperature: Room temperature

- Agitation: Moderate

- Etch rate: ~200nm/min

Cu Wet Etching

- Etchant: Transene CE-200

- Etch temperature: Room temperature

- Agitation: Moderate

- Etch rate: ~5µm/min

PECVD Oxide Deposition (~3µm)

- Temperature: 200ºC

- Gases: N2O: 710sccm, 5%SiH4 / 95%N2:170sccm

- Pressure: 1000mTorr

- Power: 20W

- Time: 60nm/min

Reactive Ion Etching of Oxide

- Gases: C4F8: 10sccm, He: 10sccm

- ICP Power: 1400W

- Electrode Power: 50W

- Pressure: 1mTorr

- Temperature: Room temperature

- Etch rate: 220nm/min

E-Beam Deposition of AuSn (74/26)

- Pressure: 1μTorr

- Voltage: 7kV

- Current: 150mA

- Temperature: Room temperature

- Deposition rate: ~1.5nm/sec

Wafer Bonding

- Gas: H2N2

- Normal Force: 3000N

- Bonding Temperature: 330ºC